FEDERAL UNIVERSITY OF ITAJUBA - UNIFEI
GRADUATE PROGRAM IN ELECTRICAL ENGINEERING

Enhanced Power Flow Methods in Complex Plane for VSC-MTDC Hybrid AC/DC Transmission Grids

Guilherme Souto Chagas

Itajuba, November 22, 2022

FEDERAL UNIVERSITY OF ITAJUBA - UNIFEI
GRADUATE PROGRAM IN ELECTRICAL ENGINEERING

Guilherme Souto Chagas

Enhanced Power Flow Methods in Complex Plane for VSC-MTDC Hybrid AC/DC Transmission Grids.

Thesis submitted to the Graduate Program in Electrical Engineering as part of the requirements for obtaining the Title of Doctor of Science in Electrical Engineering.

Area of Concentration: Electric Power Systems

Supervisor: Prof. Dr. Robson Pires

November 22, 2022

Itajuba

FEDERAL UNIVERSITY OF ITAJUBA - UNIFEI
GRADUATE PROGRAM IN ELECTRICAL ENGINEERING

Enhanced Power Flow Methods in Complex Plane for VSC-MTDC Hybrid AC/DC Transmission Grids.

Guilherme Souto Chagas

Thesis approved by examination committee on the 24^{th} of August 2022, granting the author the title of **Doctor of Science in Electrical Engineering**.

Examination Committee:
Prof. Dr. Maurício Aredes
Prof. Dr. Carlos Alberto de Castro Junior
Prof. Dr. João Alberto Passos Filho
Prof. Dr. Zulmar Soares Machado Junior
Prof. Dr. Benedito Donizeti Bonatto
Prof. Dr. Robson Pires, supervisor

Itajuba
2022

Agradecimentos

Ao final desta caminhada, me lembro de muitas pessoas que, de alguma maneira, participaram para que este trabalho fosse possível. Venho expressar em breves palavras meu profundo agradescimento.

Em primeiro lugar, ao Prof. Dr. Robson Pires, por assumir minha orientação desde meu programa de mestrado e apresentar uma proposta de pesquisa instigante que imediatamente chamou minha atenção. Foram seis anos de muita pesquisa e investigação, onde juntos compartilhamos êxitos e dividimos frustrações, sempre com muito apoio.

Aos Profs. Drs. Maurício Aredes, João Alberto Passos, Carlos Castro, Zulmar Machado, e Benedito Bonatto, que trouxeram sugestões e comentários valorosos que engradeceram este trabalho.

À FAPEMIG (Fundação de Amparo à Pesquisa do Estado de Minas Gerais), pela bolsa de estudos e auxílio financeiro que possibilitou minha dedicação integral ao programa e à realização deste trabalho.

Aos meus pais, Maria e Osmar, por serem meu porto seguro, sempre me dando força e suporte na minha trajetória.

À Ângela Maria, pelas incontáveis horas de dedicação e trabalho que tanto me ajudaram a encontrar inspiração, confiança e discernimento para seguir com meus objetivos.

À Olívia Stephen (*in memoriam*), pelo carinho e acolhimento irrestritos nos anos em que estivemos um pelo outro, por me ensinar sobre as mais variadas coisas, pelos momentos de euforia, e pelos melancólicos também. Olívia, você me mostrou a liberdade de ser verdadeiro. Obrigado, minha amiga.

E, claro... ao Caio, por todo seu carinho, amor e incentivo, por sempre acreditar em mim, principalmente nos meus momentos de maior dúvida, por ser e me fazer leve. Mesmo longe, sempre aqui.

"Bottomless wonders spring from simple rules,
which are repeated without end."
– Benoit Mandelbrot

Abstract

The power flow problem is composed of phasor variables and quantities and thus can be naturally formulated in the complex domain; however, their applications are commonly developed in the real domain. The solution via the Newton-Raphson method, for example, would be restricted in the real domain once the Taylor series expansion in terms of complex variables alone does not exist. Thanks to the Wirtinger calculus, a Newton-Raphson method based on Taylor series expansions of nonlinear functions of complex variables and their complex conjugates becomes possible. As new technologies are implemented in power systems, such as the incorporation of FACTS devices, the development of power flow applications becomes increasingly intricate, and maintaining their formulations in the real domain is preceded by an arduous algebra task. To overcome this difficulty, a series of power flow solution methods are proposed in this work, specified to solve multi-terminal AC/DC hybrid systems, being formulated in the complex plane without any loss of precision. Both sequential and unified approaches for solving hybrid AC/DC power flow are derived in the complex plane. In order to improve the performance of the algorithms, an exact second-order power flow algorithm in the complex domain is also proposed. Such power flow models in the complex plane are naturally developed in Cartesian coordinates; therefore, most constraint equations can be written as quadratic functions. Consequently, the Taylor series expansion stops at its second order and the exact non-linearity of complex quadratic power flow equations is maintained. Minor changes in the code structure are required to transform the Newton-Raphson method into the exact power flow approach in the complex plane. The new algorithm exhibits either a superior behavior in fully AC or hybrid AC/DC networks. In order to show the validity of its formulations, the proposed algorithms are implemented in Matlab for well-established case studies of the IEEE-14, -30, -57 and -118 bus, a modified version of the IEEE Two Area RTS-96, and the Brazilian Southern-equivalent of 1916-buses, termed as SIN-1916. The features and advantages of the proposed algorithms are illustrated through the test systems interconnected across a DC network prone to several scenarios, e.g., topology, voltage control, and interchanging of active power.

Key-words: Complex-valued Newton-Raphson method; Second-order load flow; Sequential AC/DC power flow; Unified AC/DC power flow; VSC-HVDC; MTDC transmission grids; Wirtinger Calculus.

Resumo

O problema de fluxo de carga é composto por variáveis e grandezas fasoriais e pode ser naturalmente formulado no domínio complexo; porém, suas aplicações são comumente desenvolvidas no domínio real. A solução via o método de Newton-Raphson, por exemplo, estaria restrita ao domínio real uma vez que a expansão em séries d Taylor em termos somente das variáveis complexas não existe. Mas, graças ao cálculo de Wirtinger, um método de Newton-Raphson baseado em expansões em série de Taylor de funções não lineares de variáveis complexas e seus conjugados complexos se faz possível. A medida em que novas tecnologias são implementadas nos sistemas de potência, como a incorporação de dispositivos FACTS, o desenvolvimento de aplicações de fluxo de carga se torna cada vez mais complexa, e manter suas formulações no domínio real necessita de uma árdua tarefa de álgebra. Para superar esta dificuldade, uma série de métodos de solução de fluxo de potência é proposta neste trabalho, especificados para solucionar sistemas híbridos AC/DC multi-terminal, sendo formuladas no plano complexo sem qualquer perda de precisão. Tanto a abordagem sequencial quanto a unificada para a solução do fluxo de potência híbrido AC/DC são derivadas no plano complexo. Com o objetivo de melhorar o desempenho dos algoritmos, também é proposto um algoritmo exato de fluxo de potência de segunda ordem no domínio complexo. Tais modelos de fluxo de potência no plano complexo são naturalmente desenvolvidos em coordenadas cartesianas; logo, a maioria das equações de restrições pode ser escrita como funções quadráticas. Consequentemente, a expansão em séries de Taylor se encerra na sua segunda ordem e a não linearidade exata das equações complexas quadráticas de fluxo de potência é mantida. Pequenas alterações na estrutura do código são necessárias para transformar o método de Newton-Raphson na abordagem exata do fluxo de potência no plano complexo. O novo algoritmo exibe um comportamento superior em redes totalmente AC ou híbridas AC/DC. A fim de mostrar a validade de suas formulações, os algoritmos propostos são implementados em Matlab para estudos de casos bem estabelecidos dos sistemas teste IEEE-14, -30, -57 e -118 barras, uma versão modificada do sistema de duas áreas IEEE RTS-96, e o sistema interligado nacional SIN-1916 barras. As características e vantagens dos algoritmos propostos são ilustradas através dos sistemas teste interligados através de uma rede DC propensa a vários cenários sob diferentes topologias, controles de tensão e injeções de potência ativa, por exemplo.

Palavras-chaves: Fluxo de carga AC/DC sequencial; Fluxo de carga AC/DC unificado; Fluxo de carga de segunda ordem; Método Newton-Raphson no domínio complexo; Redes de transmissão MTDC; VSC-HVDC; Wirtinger Calculus.

List of Figures

List of Tables

List of abbreviations and acronyms

AC	Alternating Current
ADS	AC/DC Sequential power flow method
ADU	AC/DC Unified power flow method
CSC	Current-Source Converter
CV	Complex-Valued
DC	Direct Current
EIA	Enhanced Iwamoto's Approach
ELM	Enhanced Levenberg-Marquardt Power Flow
EPF	Exact Power Flow
FACTS	Flexible AC Transmissions System
FDLF	Fast Decoupled Load Flow
HVDC	High-Voltage Direct Current
IGBT	Insulated Gate Bipolar Transistor
LCC	Line-Commutated Converter
LM	Levenberg-Marquardt
MMC	Modular Multilevel Converter
NPC	Neutral-Point Clamping
MTDC	Multi-terminal HVDC
NR	Newton-Raphson
OLTC	On-Load-Tap-changer
PCC	Point of Common Coupling
PFA	Power Flow Analysis
PSSE	Power System State Estimation

PWM	Pulse Width Modulation
RV	Real-Valued
SCR	Short Circuit Ratio
SIN	Sistema Interligado Nacional
SM	SubModule
STATCOM	Static synchronous compensator
VSC	Voltage-Source Converter

List of symbols

a, a^*	Complex and complex conjugate tap position
$\Im\{\cdot\}$	Imaginary part of a complex quantity or variable
$\mathbf{J}$	Complex-valued Jacobian matrix
K	DC voltage droop gain
$\underline{M}$	Mismatches vector
p	DC system polarity factor
P_{loss}	Converter power losses
P_{losses}	Overall converter station power losses
$\Re\{\cdot\}$	Real part of a complex quantity or variable
S_{loss}	Converter station component power losses
x, x^*	Complex and complex conjugate state variable
$\underline{x_c}$	State variables vector in the conjugate coordinates system
Y	Complex admittance
$\underline{Y_c}$	Vector of functions in the conjugate coordinates system
$\mathbf{Y}$	Bus admittance matrix
Z	Complex impedance
$\Delta(\cdot)$	denotes a quantity or variable deviation
ν	Iteration counter
$\|\| \cdot \|\|$	Euclidean norm
$\|\| \cdot \|\|_\infty$	Infinity norm
$\underline{(\cdot)}$	Quantity or variable vector

Superscripts

$(\cdot)^{H}$	Complex conjugate transpose, i.e., Hermitian operator
$(\cdot)^{ref}$	Value of reference
$(\cdot)^{spec}$	Specified value
$(\cdot)^{T}$	Complex transpose
$(\cdot)^{*}$	Complex conjugate

Subscripts

$(\cdot)_{ac}$	AC grid quantity or variable
$(\cdot)_{c}$	VSC quantity or variable
$(\cdot)_{dc}$	DC grid quantity or variable
$(\cdot)_{eq}$	Equivalent value
$(\cdot)_{f}$	VSC AC filter quantity or variable
$(\cdot)_{t}$	VSC transformer quantity or variable
$(\cdot)_{s}$	PCC quantity or variable

Contents

1 Introduction

1.1 Context and Motivation

The power flow equations are primordially complex-valued (CV) formulations. Due to their state variables, the most natural, compact, and direct way to formulate it is in the Complex Domain [1]. However, numerical solutions for solving power system applications, such as the power flow analysis and power system state estimation, were typically adapted and carried out in the real domain, and this is not arbitrary. The solution methods of these problems often require a first- or second-order approximation of the set of nonlinear power flow equations. Nonetheless, such methods cannot be applied to nonlinear functions of complex variables because they are non-analytic in their arguments. Therefore, for these functions, Taylor series expansions do not exist. Hence, this problem has been solved for many decades by redefining the nonlinear functions as separate functions of the real and imaginary parts of their complex arguments so that standard methods can be applied.

Although not widely known, the *Wirtinger Calculus* [2] is a solution for this issue, where the equations can be expanded in terms of the complex variables and their conjugates. This property lies in the fact that if a complex function is analytic in the space spanned by $\Re\{x\}$ and $\Im\{x\}$ in $\mathbb{R}$, it is also analytic in the space spanned by x and its conjugate x^* in $\mathbb{C}$. This expansion allows the construction of differential calculus for such functions that is entirely analogous to the ordinary differential calculus for functions of real variables [3]. Yet, for several decades the computers had limited processing, especially for complex arithmetic. Thus, solving it in the real domain was still more advantageous, replacing its complex phasors with their corresponding real-valued (RV) variables in rectangular or polar coordinates. However, this is no longer a constraint: modern processors employ single instruction multiple data (SIMD), resulting in a CV formulation that is faster than the classical RV one [4]. Therefore, the former limitations on solving power flow equations in the complex plane are now surpassed, and the need for space spanning in $\mathbb{R}$ is dismissed. In addition, the distinct advantage of a more straightforward software implementation is retrieved.

This new scene has rescued the interest in researching how the complex implementation of the power flow equations can improve algorithms for power system applications and analysis, making those more adaptable for recent constraints such as the insertion of distributed and renewable energy generation and FACTS to the grid. [5] presents the general methods and analyses for power flow analysis and power system state estimation using Wirtinger's calculus. [6] specializes the complex variable Newton Raphson in distribution networks. [7] proposes a CV formulation for unbalanced radial networks. [8]

presents the Newton Raphson Power Flow with FACTS devices. A novel non-iterative power flow method based on holomorphic embedding in complex plane was proposed in [9, 10], and has opened a whole new research path. In [11] it was presented a robust Levemberg-Marquardt for solving ill-conditioned systems.

1.2 Contributions of the Thesis

This thesis provides contributions to the stead-state study of hybrid AC/DC power systems with multi-terminal HVDC grids. In particular, the analysis focuses on the formulation of such systems and components in the complex-plane. The impact of adopting a complex-valued formulation, which for many decades was left aside due to no-longer existing computational constraints, is studied along with enhancement numerical techniques which was made possible by such formulation. The adequation of well-established real-valued power flow methodologies for its natural formulation in the complex plane is developed and enhanced. Results are supported by steady-state simulations performed on test cases under different scenarios in Matlab.

This thesis is organized as follows. Chapter 2 is introductory, providing an overview of HVDC technology, with a focus on recent developments in VSC HVDC technology. Furthermore, the advantages of HVDC transmission over AC transmission are given. Chapter 3 describes the complex-valued model solution aiming at the power flow analysis (CV-PFA) problem. In Chapter 4 it is developed the exact power flow formulation in the complex plane and it discusses the set of simulations aimed to support the proposal. The major contributions of this work are in Chapter 5 and can be summarized as:

- The generalized VSC-MTDC model in complex-plane;
- The sequential AC/DC power flow algorithm with the proposed VSC model;
- A simplified sequential AC/DC power flow algorithm;
- A unified AC/DC power flow algorithm with a fully decouplable Jacobian matrix;
- An exact second-order unified AC/DC power algorithm by applying the methodology discussed in Chapter 4.

Also, simulations are carried out aiming to validate and evaluate the numerical performance of the proposed contributions. Finally, in Chapter 6 are gathered some overall conclusions of the work.

2 HVDC Technology

Although High Voltage Direct Current (HVDC) transmission might be considered to be a mature technology, it is quite amazing how many new aspects and projects are under consideration. The complexity of electrical power systems is increasing owing to its interconnections with existing systems and application of new technology to provide realiable and clean power at the lowest cost. Furthermore, there is growing interest to incorporate renewable energy sources into the grids. Applications of HVDC transmission technology are necessary as a means to overcome such problems.

The development of HVDC transmission system dates back to the 1930s when mercury arc rectifiers were invented [12]. The HVDC type of electrical power transmission began its first commercial operation in Gotland, Sweden in 1954 through a submarine cable interconnection. Since the 1960s, HVDC transmission is being improoved with new conceptions of switches and is now a mature technology and has played a vital part in both long distance transmission and in the interconnection of systems. In the early 1970s, the advent of the thyristor valve gave a boost to the applications of HVDC and considerably enhanced reliability and lowered the costs of implementation. The availability of high power forced commutated switches in the 1990s further enhanced the applications for HVDC, which now operates in partnership with FACTS-based AC transmission to provide complex and versatile modes of power transmission. New applications are always being developed. It is important, therefore, that the technology continues to be developed too and that new researchers and engineers continue to understand this technology.

2.1 HVDC Technology Concepts

HVDC transmission systems combine high reliability with a long useful life. Their core component is the power converter, which serves as the interface to the AC transmission system. The conversion from AC to DC, and vice versa, is achieved by controllable electronic switches (valves). HVDC technology covers different concepts and applications, e.g. advantages and limitations over AC transmission, configurations, and conversors. Some of those are discussed in this section.

2.1.1 Advantages of HVDC Systems

The continuing and revived interest in DC systems can be attributed to different factors:

Investment costs One of the advantages DC has over three-phase AC systems is the need for only two conductors instead of three, or only one in case of a monopolar link with ground return. Figure 1 shows schematically the tower configurations for 1200 MW (two circuits AC, bipolar DC) and 1500–2000 MW transmission at EHVAC single circuit or monopolar DC [12]. Figure 2 shows a simplified cost comparison for DC and AC transmission lines. In the case of HVDC the initial capital investment is much higher because of the converter costs. As the transmission distance increases, the benefits of DC offset the capital investment and at certain distance the total cost of an HVDC system is same as an AC line [13].

Long-distance transmission In AC systems, a number of technical challenges arise when the transmission distance increases. In overhead line systems, voltage control becomes an issue: with long lines, compensation is needed, which can give rise to new problems, such as subsynchronous resonances [14]. In a high voltage cable connection, the transmission distance is a limiting factor due to the charging current, which increases with increasing voltage. At high voltages, this charging current can even prevent the cable from carrying active power.

Cable connections The absence of this steady-state charging current makes that DC power, contrary to AC power, easily allows to use cables at high voltages. This makes HVDC connections particulary feasible for submarine power transmission.

Transmission line losses In an AC line, the current density in the conductor is unequally distributed as an AC current has the tendency to primarily flow near the conductor surface. This "skin effect" results in a higher line resistance for AC currents compared to DC currents, which do not suffer from this unequal current distribution. Furthermore, DC lines only carry active power, contrary to AC lines where also reactive power adds up to the total line loading. These two factors make that line losses are lower for DC transmission for similar power and voltage ratings.

Enhanced controllability In a DC link, the power through the line is fully controllable. This controllability yields a number of advantages, especially when the link is to be operated in the framework of a market-oriented environment. Similarly, in a DC grid, the power injections at different converters can be set independently. The controllability also opens the possibility to use the link to provide auxiliary services, e.g. sharing of primary reserves and power system damping.

Asynchronous interconnections DC technology allows to interconnect asynchronous systems that operate at a different or at the same frequency, regarding that if phase difference between two AC systems is large, they cannot be directly connected.

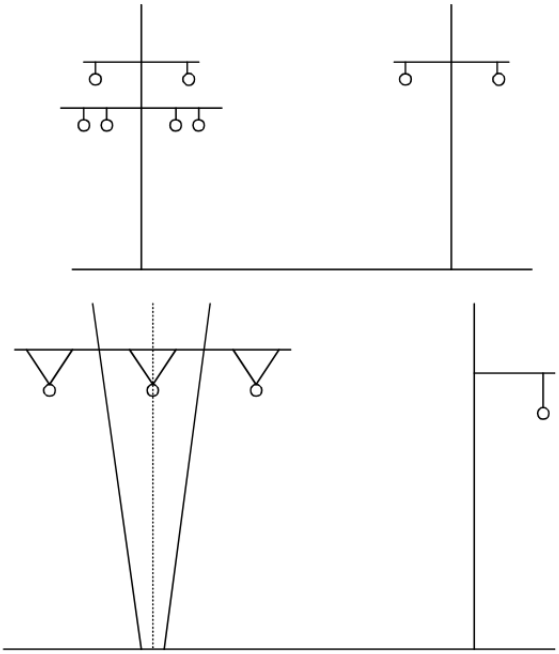

Figure 1 – Tower configurations for HVAC and HVDC transmission [14].

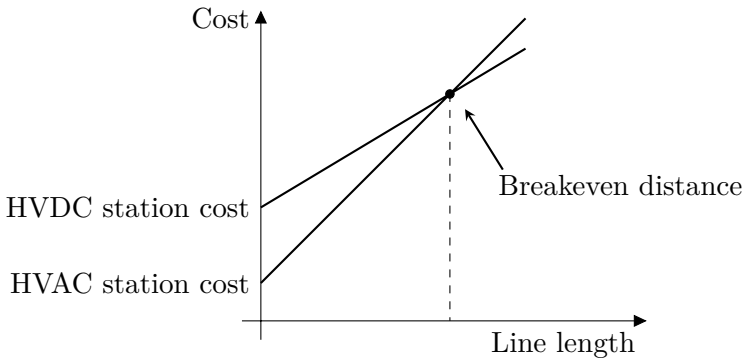

Figure 2 – HVDC and HVAC transmission cost comparison.

It is clear from the above that DC technology especially yields advantages when long-distance and submarine power transmission is considered. Consequently, when the transmission distance is small, the high investment cost for the converter stations might not be offset by the lower investment cost for the transmission line. A similar reasoning holds for the overall system losses: the converter losses result in higher overall loss figures for short connections. Furthermore, the complexity of the converter stations results in a large number of components, which in turn demands a robust control strategy for ensuring the reliability and availability of the overall transmission scheme.

2.1.2 Example applications

Example applications of HVDC transmission systems in [14] are shown in Figure 3, in which the labeling is as follows:

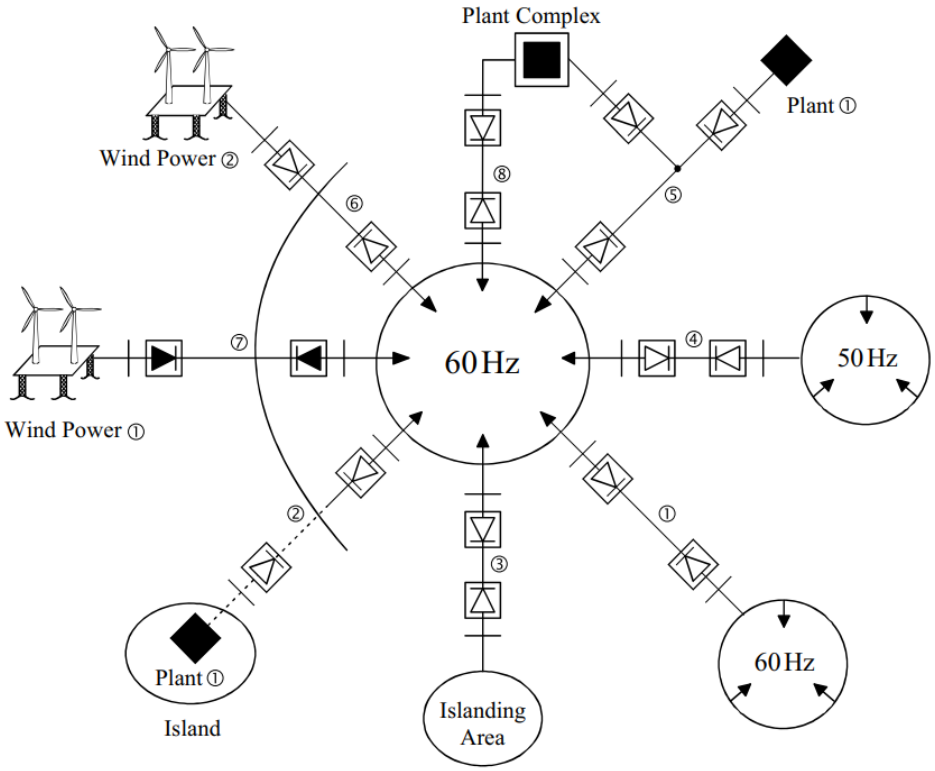

Figure 3 – Various applications of an HVDC system [14].

1. Power transmission of bulk energy through long distance overhead line.

2. Power transmission of bulk energy through sea cable.

3. Fast and precise control of the flow of energy over an HVDC link to create a positive damping of electromechanical oscillations and enhance the stability of the network by modulation of the transmission power by using a Back-to-Back configuration.

4. Since an HVDC link has no constraints with respect to frequency or to phase angle between the two AC systems, it can be used to link systems with different frequencies using an asynchronous Back-to-Back configuration.

5. When power is to be transmitted from a remote generation location across different countries or different areas within one country, it may be strategically and politically necessary to offer a connection to potential partners in the areas traversed by using a multi-terminal DC link.

6. An HVDC transmission system can also be used to link renewable energy sources, such as wind power, when it is located far away from the consumer.

7. VSC (Voltage Source Converter) based HVDC technology is gaining more and more attention. This new technology has become possible as a result of important advances in the development of Insulated Gate Bipolar Transistors (IGBT). In this

system, Pulse-Width Modulation (PWM) can be used for the VSC as opposed to the thyristor based conventional HVDC. This technology is well suited for wind power connection to the grid.

8. Since reactive power does not get transmitted over a DC link, two AC systems can be connected through an HVDC link without increasing the short circuit power; this technique can be useful in generator connections.

2.1.3 HVDC System Configurations

The two most basic HVDC link configurations are the point-to-point and back-to-back. Most HVDC systems fall under point-to-point category, which refers to long distance power transmissions. It consists of either cable or overhead lines or a combination of these two. In the back-to-back type of system, the rectifier and the inverter are located in the same station. In general,it is used for providing an asynchronous interconnection for two AC systems.

HVDC point-to-point systems are classified as either monopolar or bipolar schemes. Fig. 4 shows the different configurations for a point-to-point link. A monopolar link (Fig. 4a) is the base configuration. It uses only one conductor and has a ground return path or a metallic return, yielding considerable cost reductions: the metallic return requires less insulation as it is at low voltage. A ground return results in the highest cost reduction, but is not always allowed because of perceivable problems related to metallic corrosion of objects in the vicinity of the grounding electrodes.

A comparable scheme is the symmetric monopole (Fig. 4b). The symmetric monopole uses two conductors with opposite voltage polarity and is only earthed by means of a high impedance. Hence, no earth currents flow. The scheme has primarily been used for VSC HVDC schemes.

As an alternative to monopolar transmission schemes, a bipolar scheme (Fig. 4c) can be used. Similar to the symmetric monopole, the bipole as well has a pair of conductors with opposite voltage polarity. However, the bipolar scheme has two converters connected in series at each converter end and the junction of the two converters is grounded, either at one point or possibly at both ends. Under normal operation, the current in the two lines is equal in magnitude and there is no ground current. However, the scheme can still operate at half the power with the outage of one pole, increasing the overall redundancy in the system. With similar power ratings to the monopolar scheme from Fig. 4a, the conductors only carry half of the current.

The extension of a point-to-point HVDC system to a system with three or more converters stations is denominated multi-terminal HVDC system. It requires a signifi-

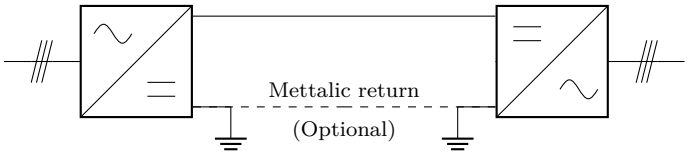

(a) Monopole

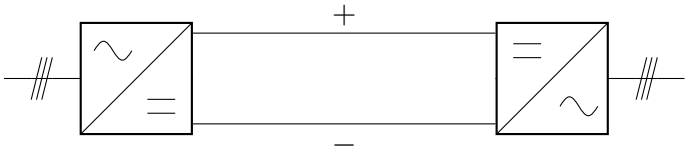

(b) Symmetrical monopole

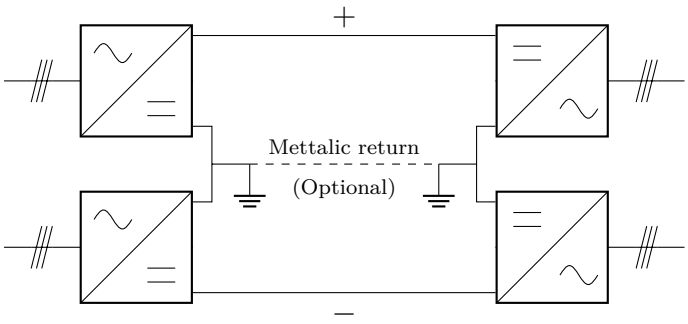

(c) Bipole

Figure 4 – HVDC system configurations.

cant complexity to facilitate communication and control between each converting station. However, it is considered to be a relatively new technology and has shown potential for a wide range of applications. A more thorough discussion concerning the multi-terminal configuration is presented in Section 2.4.

2.2 Current Source Converter (CSC) HVDC

Using thyristor valves, the HVDC schemes discussed in this section are commonly referred to as Current Source Converter (CSC) HVDC or alternatively Line Commutated Converter (LCC) HVDC. The valves can be switched on, but need the current to pass through zero in order to switch off and therefore depend on the external AC grid for commutation. The basic module for a CSC HVDC link is a three-phase full-wave 6-pulse converter, also known as the Graetz bridge (Fig. 5). The scheme can be used to transmit power in both directions. This is accomplished by changing the firing angle of the thyristor, which in turn results in a voltage polarity change of the link.

As a result of the operating principles – the thyristor valves only start conduction when triggered – and the commutation between two phases, which introduces an additional current lagging, the converters inherently absorb reactive power. The least expensive way to compensate for the reactive power is to provide reactive compensation by means of switchable capacitor banks which are partly already present in the form of

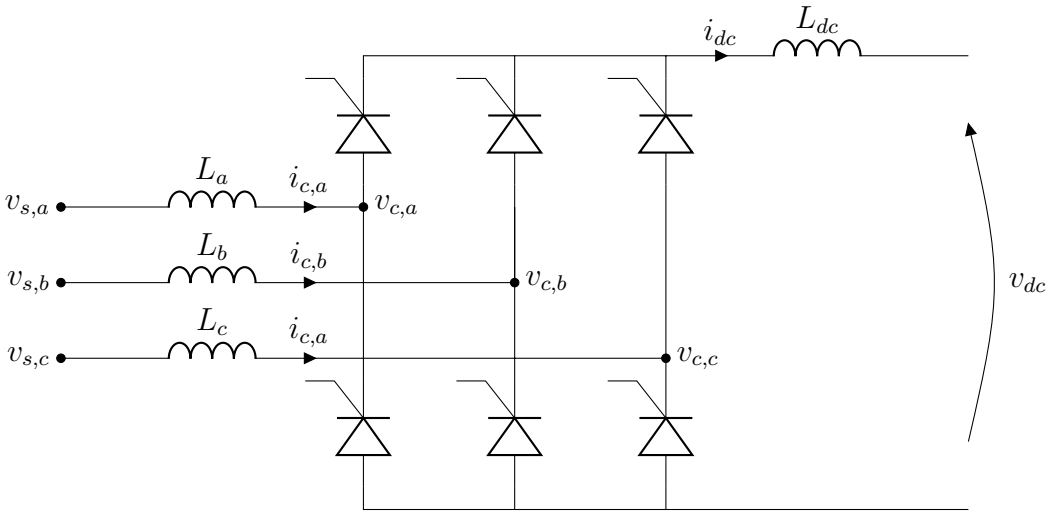

Figure 5 – LCC HVDC Graetz bridge.

selective filters. Alternatives include the use of a static var compensator (SVC), a nearby generator or a synchronous condenser.

The current source converter introduces a significant amount of harmonics, both at the AC and DC side. These harmonics have to be filtered in order to prevent them from entering the system and from causing a distortion of the voltage waveform. At the AC side, usually a combination of tuned filters is used. The harmonic currents flow within the converter transformer, that has to be specially designed to cope with the resulting voltage stresses and losses. At the DC side, a distinction is made between characteristic harmonics determined by the pulse number of the converter, and non-characteristic harmonics caused by AC side unbalances [12]. The DC side harmonics are reduced by the smoothing reactor L_{dc} (Fig. 5) and filters.

One of the main disadvantages of the CSC HVDC scheme, however, is the need for a relatively strong AC system, commonly expressed in terms of the short-circuit ratio (SCR) at the point of common coupling (PCC). The SCR provides an indication of the inherent strength of the AC system. Amongst the problems that can occur in low SCR systems are dynamic overvoltages, voltage instability, harmonic resonances, voltage flicker and more commutation failures [14]. To overcome the problems at low SCR, an alternative scheme, called Capacitor Commutated Converter (CCC), was developed. The scheme includes a series capacitor between the valve and the converter transformer [15]. One of the main disadvantages, however, is that the series capacitances increase the insulation costs of the valves. The scheme has therefore only been applied in back-to-back links, where the voltage ratings are much lower. The concept has been applied in the Garabi back-to-back connection between Argentina and Brazil [16] and in a back-to-back configuration in the Rio Madeira HVDC System [17].

2.3 Voltage Source Converter (VSC) HVDC

The development of the Insulated Gate Bipolar Transistor (IGBT) for high power applications in the 1990s opened up new possibilities for HVDC. The IGBT, a development from Metal-Oxide-Semiconductor Field Effect Transistor (MOSFET) technology, has a low conduction loss and a high switching speed [15]. Contrary to thyristors, IGBTs can be switched both on and off, making them well suited to be used in voltage source converters. Since commutation can be achieved quickly and independently of the AC system voltage, an entirely different type of operation compared to the LCC converter is possible. This yields a number of advantages for VSC HVDC over CSC HVDC technology:

Reactive power control Contrary to CSC HVDC, which constantly consumes reactive power, VSC HVDC can independently control the active and reactive power within the limitations of the converter. Each converter station can be used to provide voltage support to the local AC network while transmitting any level of active power, at no additional cost [13].

Connection to weak systems VSC HVDC can be used to connect to weak or even passive systems. This feature makes VSC ideally suited for connecting offshore wind farms. In case of an LCC HVDC link, the offshore converter requires an external voltage to commutate against, which calls for all but trivial technical solutions.

Good response to AC faults The VSC converter actively controls the AC voltage/current, so the VSC-HVDC contribution to the AC fault current is limited to rated current or controlled to lower levels. The converter can remain in operation to provide voltage support to the AC networks during and after the AC disturbance.

Ancillary services The VSC can be controlled to provide a variety of ancillary services, such as reactive power support, black start capabilities [18], flicker mitigation and unbalanced voltage compensation [19].

A typical VSC HVDC converter station is shown in Fig. 6 and consists of the following components:

Converter The voltage source converter itself is an active component that converts the DC side voltage to an AC voltage of an arbitrary size and shape by switching the IGBTs.

DC capacitor The DC capacitor is the energy storage element in VSC. It provides the VSC with the stiff DC voltage between switching instants, which is an essential presumption with all VSC topologies.

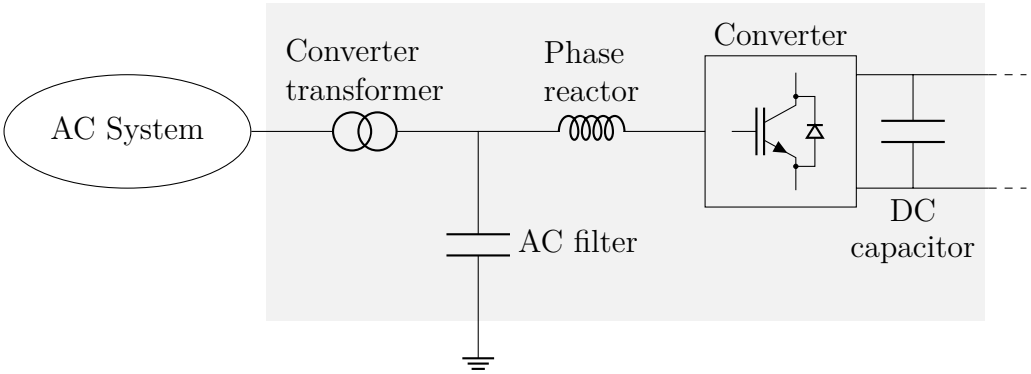

Figure 6 – VSC HVDC converter station scheme.

Phase reactor The phase reactor is essential to the operation of the VSC. The control schemes switches the IGBTs as to control the complex current through the phase reactor, thereby controlling the active and reactive power.

AC filter Since high frequency switching of the VSC only introduces high-order harmonics in the voltage waveform, these harmonics can easily be removed by a low-pass filter filter. Compared to CSC, the filter is not required to provide reactive power compensation. As a consequence, much smaller filter installations are needed.

Converter transformer The VSC transformer is usually equipped with tap changers that are used to optimize the filter bus voltage magnitude with respect to the AC grid side voltage. Other than in CSC, the VSC transformer is not exposed to low order voltage harmonics. This allows for a simpler design, similar to regular power transformers.

2.3.1 VSC Topologies

2.3.1.1 Two-level converter topology

The first generation of VSC HVDC schemes, which became commercially available as "HVDC Light" by ABB [20], was based on a two-level converter topology (Fig. 7). In order to cope with the high voltages, each converter valve, simplified in Fig. 7 to only one switching component, in reality consists of a multitude of series-connected IGBTs and their anti-parallel diodes. This series connection yields a number of challenges from a voltage balancing point of view: when fired, all stacked IGBTs should ideally start conducting at the same instant. If not, the IGBTs that start to conduct later are stressed to a high extent.

The well-known Pulse-Width Modulation (PWM) technique is used to make a sinusoidal waveform at fundamental frequency. The PWM technique basically connects the output voltage either to the positive or negative DC voltage. By varying the width of the

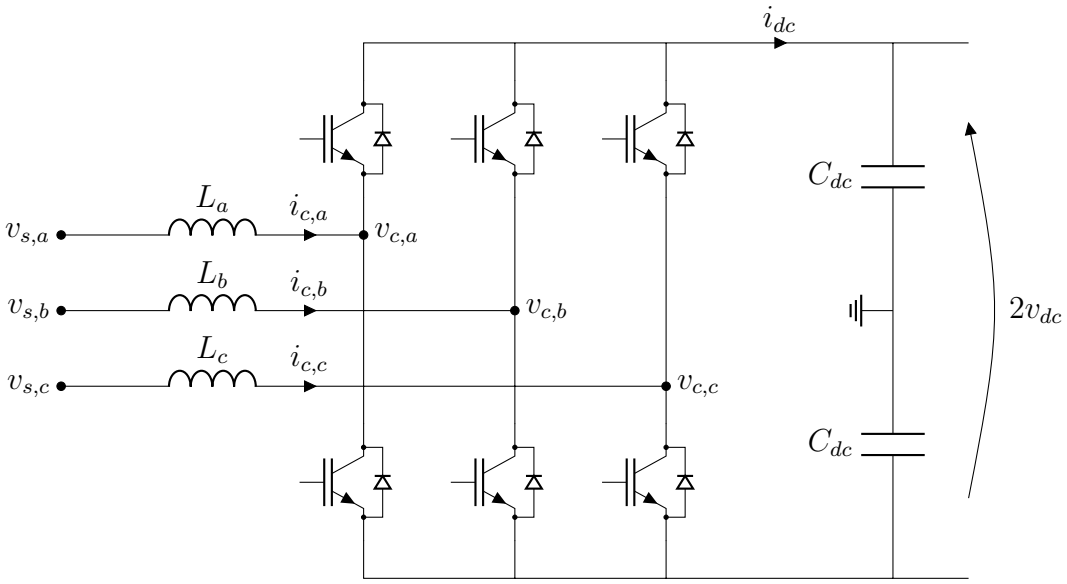

Figure 7 – Two-level voltage source converter.

pulses during which the converter voltage is connected, a high frequency voltage signal is synthesized, containing the fundamental frequency voltage signal as shown in Fig. 11a. Although IGBTs have relatively low conduction losses, the PWM switching at a frequency of about 1.5 kHz results in relatively high switching losses. Whereas fundamental-frequency switched CSC HVDC schemes are characterized by loss figures in the order of magnitude of 0.8%, the first generation of VSC HVDC schemes yielded losses that were a multiple of those of CSC schemes, adding up to 3% per converter station [15]. The subsequent innovations in the converter topologies have mainly been aiming at reducing the losses [21, 22].

2.3.1.2 Three-level converter topology

The second generation of commercially available schemes used a three-level converter with active neutral-point clamping (NPC), depicted in Fig. 8. Two diodes are inserted in each phase, clamping the voltage to half the DC voltage. Thereby, these diodes provide a third voltage level to switch between, without altering the number of switches. Fig. 11b shows the corresponding switching pattern. The use of a third voltage level yields a lower voltage per switching and hence a lower switching frequency per component. As a result, the converter losses were reduced from 3% per converter station down to 1.7% [21].

2.3.1.3 Modular multilevel converter topology

The introduction of so-called modular multilevel converters [23, 24], gave rise to various new VSC topologies for HVDC transmission [25, 26]. Fig. 9 shows the modular

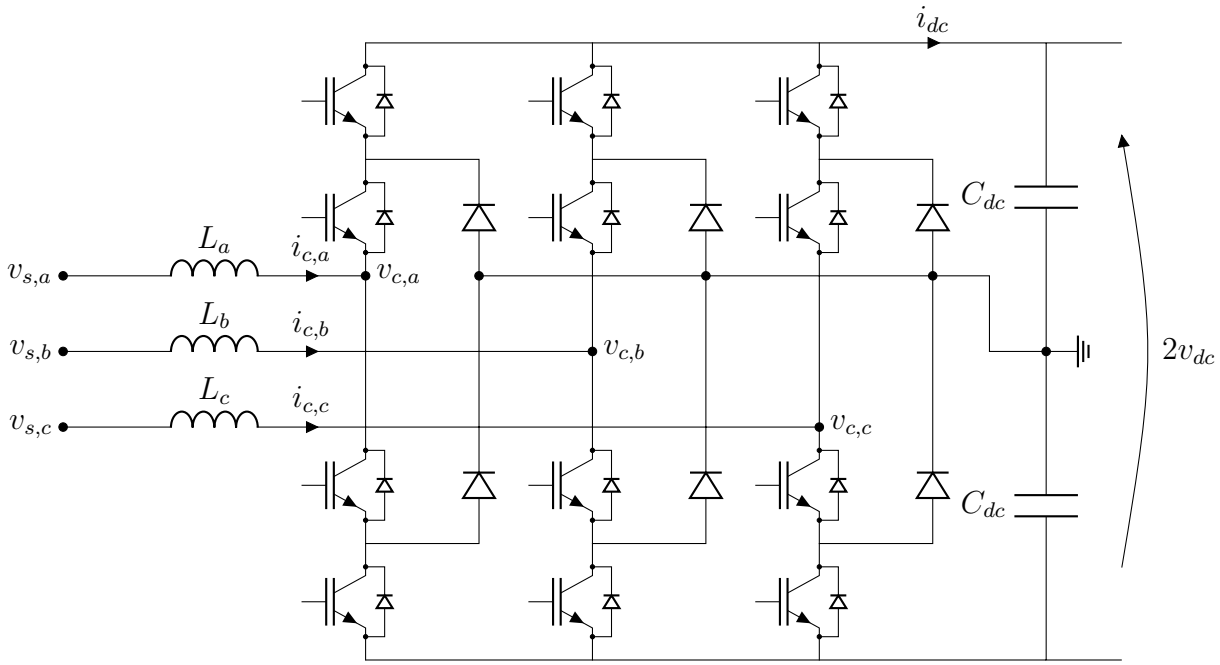

Figure 8 – Three-level neutral-point clamped voltage source converter.

structure of the MMC scheme. The basic concept of these cascaded multilevel topologies is to stack a number of submodules (SM) from Fig. 10. The MMC VSC HVDC converters use the half-bridge module from Fig. 10a, which consists of two converter valves and a capacitor. Different from the earlier topologies, the MMC topology no longer has a common DC capacitance, but includes a distributed capacitance along the valve stacks instead. Each half-bridge submodule has two switches which can be switched in the following ways:

Inserted: S_1 is switched on and S_2 is switched off.

Bypassed: S_1 is switched off and S_2 is switched on.

Blocked: both S_1 and S_2 are switched off.

The resulting waveform can be built in a stepwise manner (Fig. 11c). With a high number of submodules, the use of PWM can thus possibly be abandoned. The resulting voltage contains a much lower amount of high-order harmonics, compared to the two-level and three-level topology. For a high number of submodules, the filtering requirements are greatly reduced because of the generation of high-quality AC voltage, i.e., AC filters might not be required.

In MMC HVDC converters, the voltage level of each module typically is in the order of magnitude of some kilovolts (single IGBT voltage) and the number of modules per converter arm is about a few 100, resulting in a switching frequency of only 150 Hz

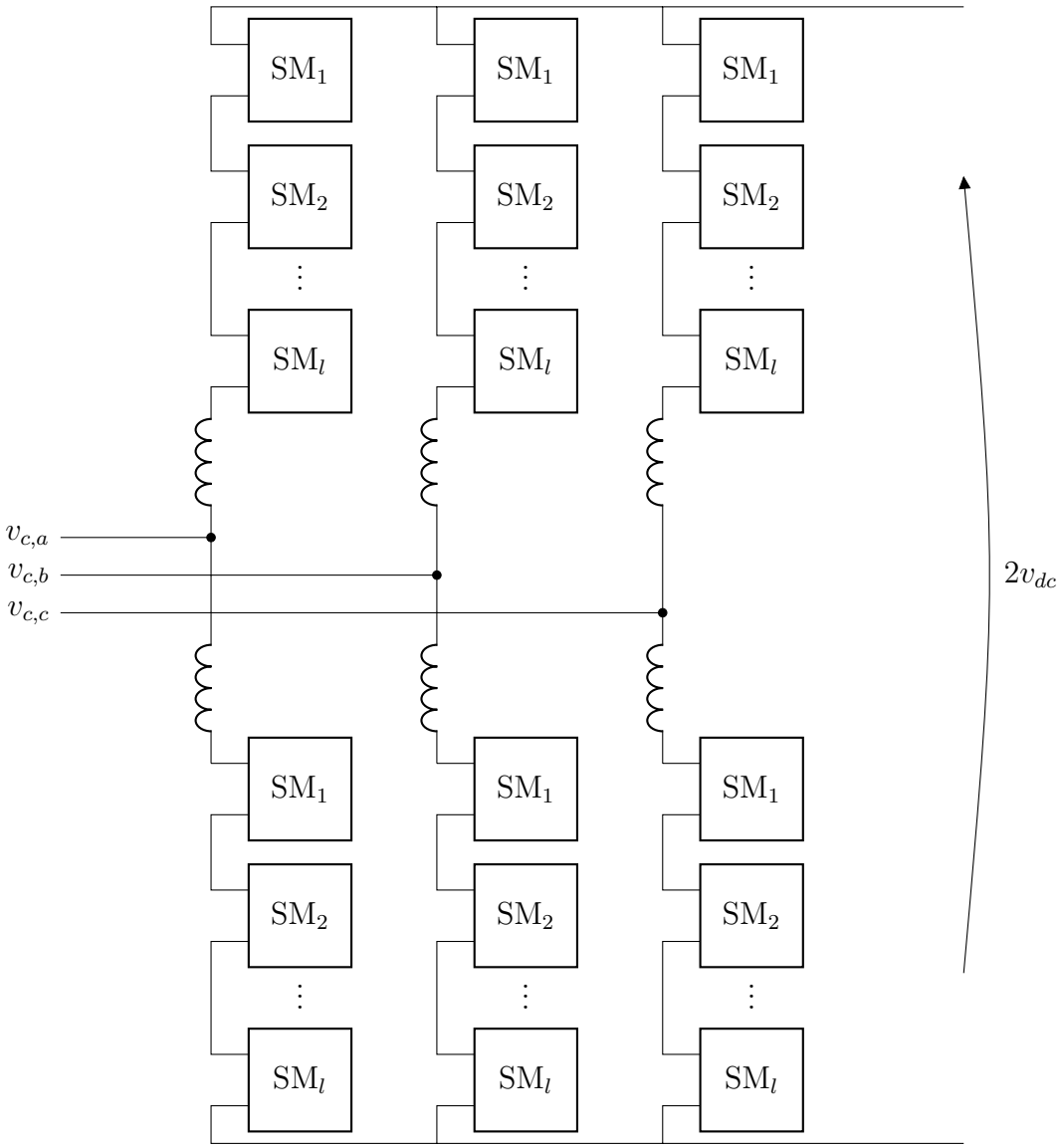

Figure 9 – Modular multilevel converter scheme.

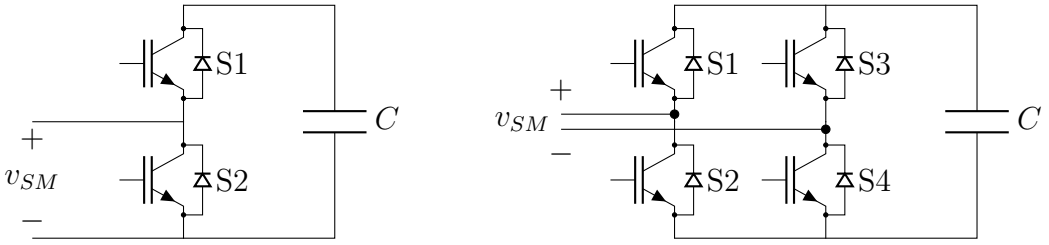

(a) Half-bridge submodule. (b) Full-bridge submodule.

Figure 10 – MMC building blocks.

per submodule [27], resulting in significantly lower switching losses: coming from 3% per converter station in the earliest two-level schemes, the losses have dropped to about 1%, which is in the order of magnitude of the loss figures for CSC HVDC schemes.

Whereas the technological challenge in the two-level topology primarily arose from the switching synchronization, the MMC concepts prove to be rather challenging from a design and control perspective as they involve balancing of the individual cell voltages. Similar to the two-level topology, faults on the DC side cannot be cleared by any converter action: although one can block the IGBTs, this only stops the current from flowing in one direction since the inverse diode connected in parallel to each semiconductor switch cannot be switched off. As a result, the VSC starts to behave as an uncontrolled diode rectifier and the current can only be interrupted by AC breaker actions. For this issue, alternatively to half-bridge cells, full-bridge modules (Fig. 10b) could be used. The full-bridge topology yields the advantage of actively control and interrupt DC fault current, providing DC fault blocking capability at the expense of increased number of switches.

2.4 Multi-terminal HVDC

Since the introduction of HVDC, engineers have been looking into the possibility of extending the technology to multi-terminal schemes. However, the working principles of CSC HVDC technology hamper a straightforward extension to MTDC systems. It is only due the introduction of VSC HVDC that new interest has risen to build MTDC grid systems.

2.4.1 DC grid layout

Fig 12 shows different topologies for connecting multiple nodes in an AC system by means of DC transmission. The term multi-terminal is generally used to describe any DC system with more than two converters interconnected at the DC side. On the contrary, it is not exactly clear what topologies are included and excluded when using the term DC grid. A first option, shown in Fig. 12a, is to build a radial MTDC system. While this topology yields cost reductions compared to point-to-point links, it can hardly be argued to be a true DC grid, as it has no redundancy in the DC system. A second option is to build a grid of DC lines, shown in Fig. 12b, where each DC link is connected to the AC system by a converter at both ends, which has the advantage of having full control over the power flow in each DC connection. The DC links can be either CSC or VSC technology and can also have different transmission voltages. Since the number of converters is twice the number of links, it is expensive. A third option, shown in Fig. 12c, is a meshed DC grid. This topology is redundant in the sense that the power can flow via different paths in case of a line outage. In the remainder of this thesis, the major focus is on meshed DC

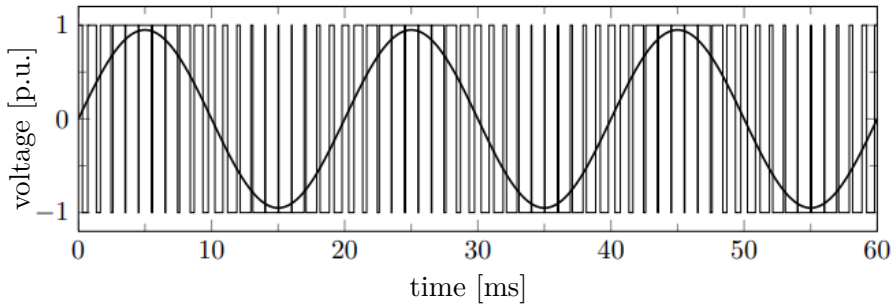

(a) Two-level converter (PWM)

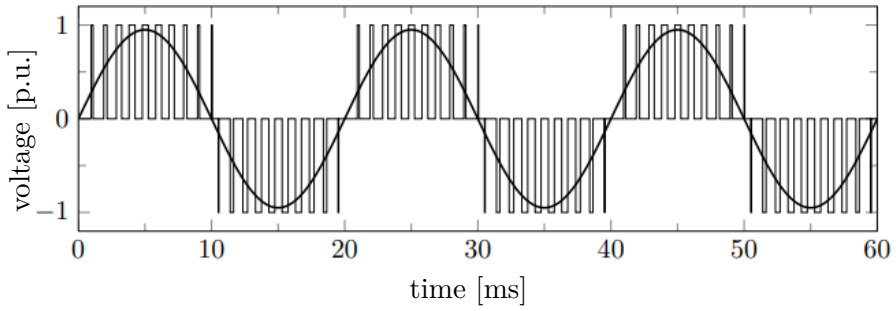

(b) Three-level converter (PWM)

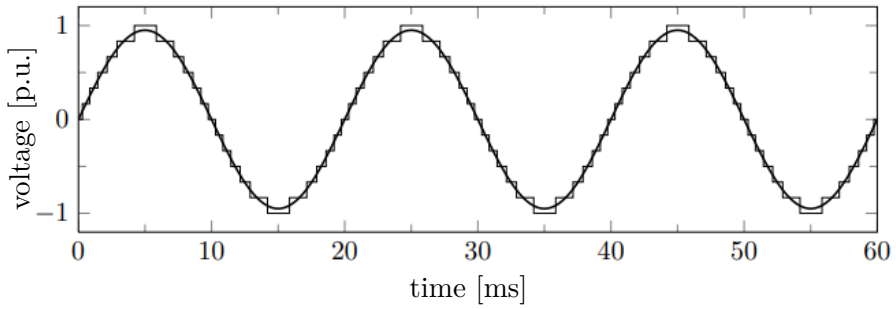

(c) Modular multilevel converter (6 submodules per arm)

Figure 11 – Switching pattern for different converter topologies.

systems, although the developed tools are also applicable to radial MTDC schemes (Fig. 12a) and multiple HVDC links (Fig. 12b).

2.4.2 Multi-terminal CSC HVDC

A classification of CSC MTDC is made based on the series or parallel connection scheme (constant current and constant voltage, respectively), as shown in Fig. 13. A hybrid scheme consisting of both parallel and series converters can also be conceived.

In a series-connected scheme, the same DC current flows through all converters. The voltage rating of a converter in the series scheme is thus proportional to the power rating. The scheme is only grounded at one point, which makes insulation coordination complex and expensive. The advantage of the series-connected scheme is that the power can be reversed at any converter without the need for mechanical switching actions.

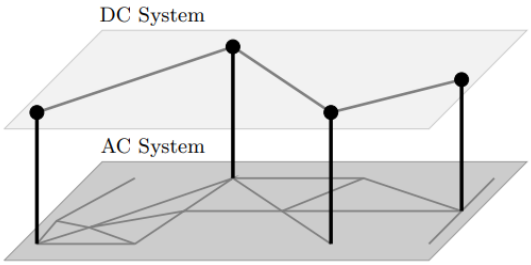

(a) Radial multi-terminal DC system

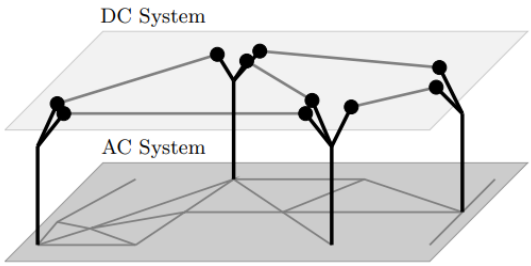

(b) Grid of DC lines

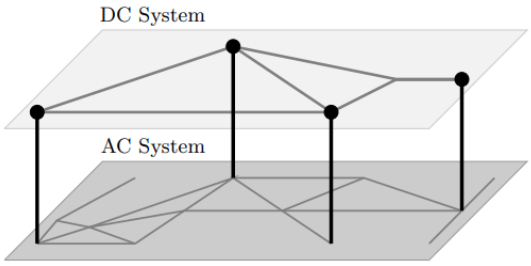

(c) Meshed DC grid

Figure 12 – Different grid topologies for hybrid AC/DC systems [28].

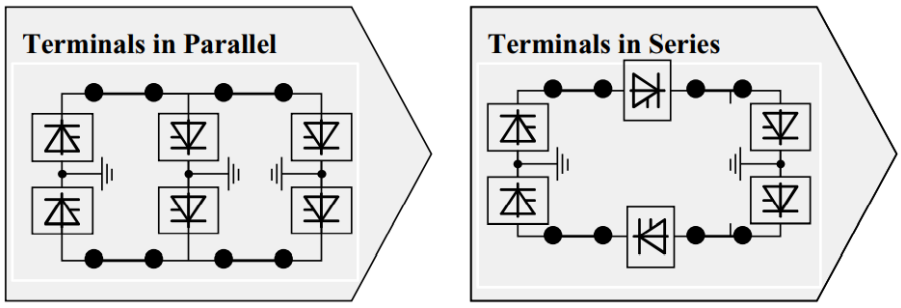

Figure 13 – CSC HVDC multi-terminal connection [14].

Disadvantages are that a line fault causes the interruption of the entire system and that the schemes are not well suited for future extensions.

In parallel schemes, the converters operate at a common DC voltage. As a power reversal in a CSC HVDC scheme is accomplished by changing the voltage polarity while the current polarity is fixed, a power reversal at one particular converter can only be realized by means of mechanical switching actions. Another problem is that commutation failures at any terminal bring down the DC voltage, which draws currents to the faulted converter. The recovery after a commutation failure is therefore more time-sensitive and depends on the AC system strength at the faulted converter terminal.

Clearly, the specifics of the CSC technology only allow for an extension of the technology to MTDC schemes with a limited number of terminals. Realizing a meshed DC grid with a large number of terminals is therefore not practically feasible. For thet, it is normally assumed that HVDC grids can only be built using VSC converters. Thereafter, although the former CSC-based MTDC systems are discussed in this section, the

contributions of this Thesis regarding the MTDC steady-state analysis are orientated to VSC HVDC technology.

2.4.3 Multi-terminal VSC HVDC

Contrary to CSC HVDC technology, VSC HVDC allows a relatively straightforward extension of the operational principles to meshed DC grids. VSC does not suffer from the drawbacks of CSC technology, such as the unavoidability of commutation failures and the strong dependence of the performance on the AC system strength. The main advantage is that with VSC HVDC, no voltage polarity reversal is needed when the energy flow changes direction. Consequently, VSCs can be relatively easy to be connected in parallel and the extension of a MTDC scheme is straightforward.

2.4.4 DC Voltage Control

Mainly three different control approaches have been suggested so far to limit the DC voltage variation: constant voltage control, voltage margin control and voltage droop control. Whereas the constant voltage and voltage margin control are good candidates for relatively small MTDC systems, the latter is preferred to be applied in DC grids because of its distributed nature as explained below.

2.4.4.1 Constant Voltage Control

The constant voltage method, also known as slack bus control, is in a sense similar to the control of two-terminal schemes, where one converter controls the DC voltage at its bus and the other converter controls the active power. Extending this principle to the case of an n-terminal system results in 1 DC voltage controlling terminal (slack bus) and n-1 terminals in constant power control mode. The constant voltage control method has been depicted in Fig. 14, which shows the control of the voltage after the outage of converter 2. For the purpose of illustration, the voltage difference between different nodes in the network has been left out. In this example, converter 1 is the converter controlling the DC voltage. This converter approximately doubles the power injected into the DC system, by first recharging the DC capacitances and afterwards maintaining the power balance, thereby accounting for the outage of converter 2.

2.4.4.2 Voltage Margin Control

The principles of voltage margin control were introduced in [29] for two- and three-terminal schemes. It is a direct extension to the constant voltage method by setting up a distributed control: in case converter 1 hits its current limit before reestablishing the power

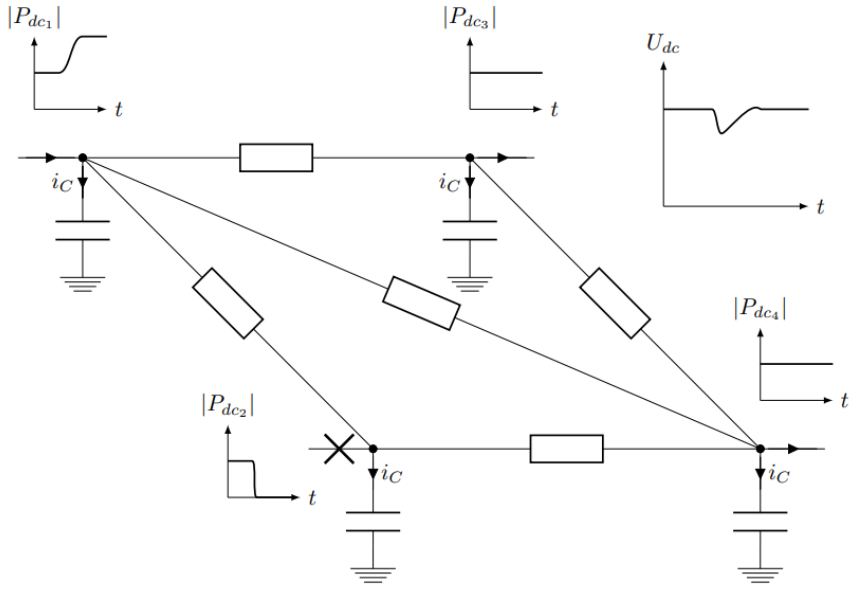

Figure 14 – Constant voltage control.

balance, the voltage decreases further, which would cause one of the remaining converter, i.e. 3 or 4, to take over the voltage control by limiting the power being inverted.

Though a valid option in VSC MTDC schemes with a limited number of terminals, the voltage margin control poses a number of challenges when used in a meshed DC system with a large number of terminals:

- Although the control can be distributed as described above, the responsibility of balancing the DC grid, even for major grid incidents, remains primarily with one particular converter, which might be unacceptable from an operational perspective.
- One has to avoid that different converters at a time start to control the voltage, which causes oscillatory behavior. This condition can e.g. occur as a consequence of improper tuning of the voltage margins with respect to the line voltage drops.
- With the number of terminals increasing, selecting the appropriate voltage margins for the different converters becomes challenging. A first reason is that the large number of converters involved make the voltage margins of some converters unacceptably high in order for them not to overlap with those of others. A second reason relies in the fact that the resulting line voltage drops, which depend on the power flows, become harder to predict and calculate in meshed systems.

2.4.4.3 Voltage Droop Control

As an alternative to voltage margin control, the voltage droop control has been developed. The control method was first presented conceptually in [30] and was later developed further and applied in [31, 32]. Fig. 15 schematically depicts the control actions

taken by the three droop-controlled converters after an outage of converter 2. Contrary to the situation with a slack bus control, converters 3 and 4 also decrease their power taken from the DC grid. Converter 1 still increases its power injection, but to a lesser extent than was the case with the voltage margin control.

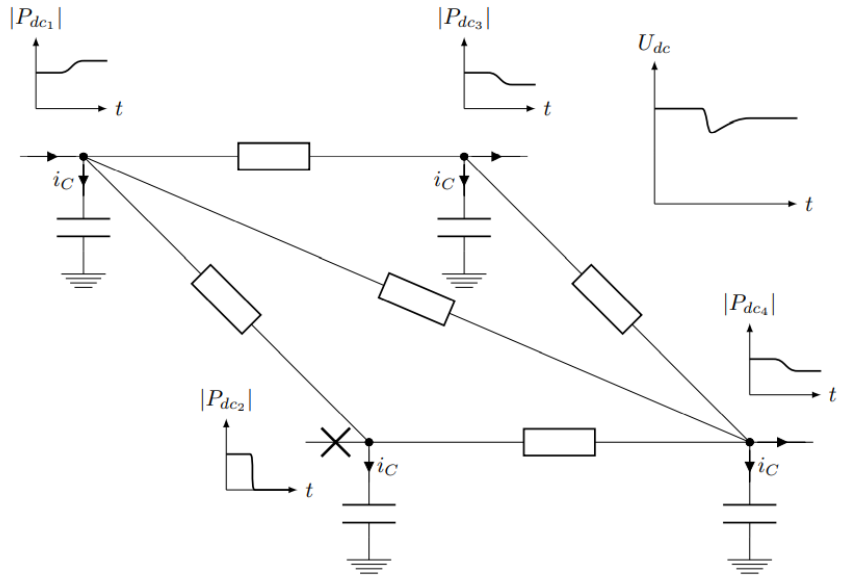

Figure 15 – Voltage droop control.

2.5 Partial Conclusions

This chapter gives a brief contextualization of DC power transmission and a technical overview, primarily focusing on VSC HVDC technology. It can be concluded that VSC HVDC technology provides significant advantages over CSC HVDC technology, which make it a preferred technological candidate for the interconnection of weak AC systems and the connection of wind farms. Furthermore, the technical specifics of VSC HVDC allow a relatively straightforward extension of the operation principles to multi-terminal transmission schemes. Recent evolution in the converter topology yield lower losses, which have been considered a significant drawback of VSC technology for many years.

3 The Generic Complex-Valued Power Flow Analysis (CV-PFA)

In this chapter is presented the derivation of the complex-valued power flow (CV-PFA) [5], derived straightforwardly from Wirtinger's Work [2]. Firstly, the whole power flow modeling starts based on the classical nodal equation as presented in [8]. The analytical model is then derived through the general power flow equations. The main reason for this latter option is the transformer model with tap position off-nominal, including phase-shifters [33, 34]. Further discussions on this issue are addressed throughout the derivation of the approaches. The analytical properties of complex-valued functions and variables, as well as the *Wirtinger Calculus*, which are the foundation of the CV-PFA, are summarized in Appendix A.

3.1 Nodal Equation

The current injections at each bus can be given by

$$\underline{I} = \mathbf{Y}\ \underline{V}, \tag{3.1}$$

where $\mathbf{Y}$ is the network nodal admittance matrix, $\underline{V} = [V_1; V_2; ...; V_n]^T$ is the bus voltage vector and $\underline{I} = [I_1; I_2; ...; I_n]^T$ is the bus current injection for n buses. Thus, the complex nodal power can be expressed as

$$\underline{S} = \underline{V} \odot \underline{I}^*, \tag{3.2}$$

or

$$\underline{S} = \underline{V} \odot (\mathbf{Y}^*\ \underline{V}^*)\,. \tag{3.3}$$

where $\odot$ is the Handamard or element-wise product. Then, the nodal complex power at bus k, i.e., S_k, is

$$S_k = V_k\ Y_{kk}^*\ V_k^* + V_k \sum_{\substack{m=0 \\ m\neq k}}^{N} Y_{km}^*\ V_m^*, \tag{3.4}$$

where $N+1$ is the number of network nodes, and the node 0 is assigned as the *slack node*.

3.2 Complex-Valued Power Flow Equations

The complex-valued power flow equations that model any type of branch in an electrical network, i.e., transmission lines and phase- and phase-shifting-transformers are as follows:

$$S_{km} = V_k \left(\frac{y_{km}^*}{a_{km} a_{km}^*} - j\ b_{km}^{sh} \right) V_k^* - V_k \frac{y_{km}*}{a_{km}^*} V_m^*, \tag{3.5}$$

$$S_{mk} = V_m \left(y_{km}^* - j\ b_{km}^* \right) V_m^* - V_m \frac{y_{km}^*}{a_{km}} V_k^*. \tag{3.6}$$

and

$$S_{km}^* = V_k^* \left(\frac{y_{km}}{a_{km}^* a_{km}} + j\ b_{km}^{sh} \right) V_k - V_k^* \frac{y_{km}}{a_{km}} V_m, \tag{3.7}$$

$$S_{mk}^* = V_m^* \left(y_{km} + j\ b_{km}^{sh} \right) V_m - V_m^* \frac{y_{km}}{a_{km}^*} V_k. \tag{3.8}$$

In the set of equations (3.5-3.8), the general off-nominal tap transformer model is composed by an ideal transformer with complex turns ratio $ae^{j\phi} : 1$ in series with its admittance or impedance [33].

3.3 Wirtinger Derivatives Applied to the Power Flow Equations

Firstly, let us assume that the complex power injections, S_k and S_m, are equal to the power flows S_{km} and S_{mk}, respectively. Then, applying the Wirtinger calculus to the complex power flow equation given by (3.5) yields

$$\left. \frac{\partial S_k}{\partial V_k} \right|_{V_k^* = Const} = \left(\frac{y_{km}^*}{a_{km} a_{km}^*} - j\ b_{km}^{sh} \right) V_k^* - \frac{y_{km}^*}{a_{km}^*} V_m^*, \tag{3.9}$$

$$\left. \frac{\partial S_k}{\partial V_k^*} \right|_{V_k = Const} = V_k \left(\frac{y_{km}^*}{a_{km} a_{km}*} - j\ b_{km}^{sh} \right), \tag{3.10}$$

$$\left. \frac{\partial S_k}{\partial V_m} \right|_{V_m^* = Const} = 0.0, \tag{3.11}$$

$$\left. \frac{\partial S_k}{\partial V_m^*} \right|_{V_m = Const} = - V_k \frac{y_{km}^*}{a_{km}^*}, \tag{3.12}$$

$$\left. \frac{\partial S_k}{\partial a_{km}} \right|_{a_{km}^* = Const} = - V_k \left(\frac{y_{km}^*}{a_{km}^2 a_{km}^*} \right) V_k^*, \tag{3.13}$$

$$\left. \frac{\partial S_k}{\partial a_{km}^*} \right|_{a_{km} = Const} = - V_k \left(\frac{y_{km}^*}{a_{km} (a_{km}^*)^2} \right) V_k^* + V_k \frac{y_{km}^*}{(a_{km}^*)^2} V_m^*. \tag{3.14}$$

and given by (3.6) yields

$$\left.\frac{\partial S_m}{\partial V_m}\right|_{V_m^*=Const} = \left(y_{km}^* - j\ b_{km}^{sh}\right) V_m^* - \frac{y_{km}^*}{a_{km}} V_k^*, \tag{3.15}$$

$$\left.\frac{\partial S_m}{\partial V_m^*}\right|_{V_m=Const} = V_m \left(y_{km}^* - j\ b_{km}^{sh}\right), \tag{3.16}$$

$$\left.\frac{\partial S_m}{\partial V_k}\right|_{V_k^*=Const} = 0.0, \tag{3.17}$$

$$\left.\frac{\partial S_m}{\partial V_k^*}\right|_{V_k=Const} = - V_m \frac{y_{km}^*}{a_{km}}, \tag{3.18}$$

$$\left.\frac{\partial S_m}{\partial a_{km}}\right|_{a_{km}^*=Const} = V_m \frac{y_{km}^*}{a_{km}^2} V_k^*, \tag{3.19}$$

$$\left.\frac{\partial S_m}{\partial a_{km}^*}\right|_{a_{km}=Const} = 0.0. \tag{3.20}$$

and given by (3.7) yields

$$\left.\frac{\partial S_k^*}{\partial V_k}\right|_{V_k^*=Const} = V_k^* \left(\frac{y_{km}}{a_{km}^* a_{km}} + j\ b_{km}^{sh}\right), \tag{3.21}$$

$$\left.\frac{\partial S_k^*}{\partial V_k^*}\right|_{V_k=Const} = \left(\frac{y_{km}}{a_{km}^* a_{km}} + j\ b_{km}^{sh}\right) V_k - \frac{y_{km}}{a_{km}}\ V_m, \tag{3.22}$$

$$\left.\frac{\partial S_k^*}{\partial V_m}\right|_{V_m^*=Const} = - V_k^*\ \frac{y_{km}}{a_{km}}, \tag{3.23}$$

$$\left.\frac{\partial S_k^*}{\partial V_m^*}\right|_{V_m=Const} = 0.0, \tag{3.24}$$

$$\left.\frac{\partial S_k^*}{\partial a_{km}}\right|_{a_{km}^*=Const} = - V_k^* \left(\frac{y_{km}}{a_{km}^* a_{km}^2}\right) V_k + V_k^* \frac{y_{km}}{a_{km}^2} V_m, \tag{3.25}$$

$$\left.\frac{\partial S_k^*}{\partial a_{km}^*}\right|_{a_{km}=Const} = - V_k^* \left(\frac{y_{km}}{(a_{km}^*)^2 a_{km}}\right) V_k. \tag{3.26}$$

Finally, applying Wirtinger calculus to (3.8) yields

$$\left.\frac{\partial S_m^*}{\partial V_k}\right|_{V_k^*=Const} = -\,V_m^*\;\frac{y_{km}}{a_{km}^*}, \tag{3.27}$$

$$\left.\frac{\partial S_m^*}{\partial V_k^*}\right|_{V_k=Const} = 0.0, \tag{3.28}$$

$$\left.\frac{\partial S_m^*}{\partial V_m}\right|_{V_m^*=Const} = V_m^*\left(y_{km}+j\;b_{km}^{sh}\right), \tag{3.29}$$

$$\left.\frac{\partial S_m^*}{\partial V_m^*}\right|_{V_m=Const} = \left(y_{km}+j\;b_{km}^{sh}\right)V_m - \frac{y_{km}}{a_{km}^*}V_k, \tag{3.30}$$

$$\left.\frac{\partial S_m^*}{\partial a_{km}}\right|_{a_{km}^*=Const} = 0.0, \tag{3.31}$$

$$\left.\frac{\partial S_m^*}{\partial a_{km}^*}\right|_{a_{km}=Const} = V_m^*\;\frac{y_{km}}{(a_{km}^*)^2}\;V_k. \tag{3.32}$$

3.4 Bus Models in the Complex Domain

3.4.1 Slack-Bus Type

The complex voltage at a *slack-bus* type is known, once the magnitude and phase-angle values are specified for the reference bus.

3.4.2 PQ-Bus Type

With the active- and reactive-power demand specified for a PQ node, the following complex mismatches functions are expressed as

$$M_k = S_k - (P_{ks} + j\;Q_{ks}), \tag{3.33}$$

$$M_k^* = S_k^* - (P_{ks} - j\;Q_{ks}), \tag{3.34}$$

where P_{ks} and Q_{ks}, are the specified active- and reactive-power injection at node k, respectively.

In order to derive the Newton-Raphson algorithm in the complex domain, the Jacobian matrix elements in complex form corresponding to each $PQ-Bus$ are formed based on the Wirtinger derivatives of M_k and M_k^* with respect to the complex and the complex conjugate nodal voltage magnitudes, yielding

$$\left.\frac{\partial M_k}{\partial V_k}\right|_{V_k^*=Const} = \sum_{m\in\Omega_k}^{N} \left.\frac{\partial S_k}{\partial V_k}\right|_{V_k^*=Const}, \tag{3.35}$$

$$\left.\frac{\partial M_k}{\partial V_k^*}\right|_{V_k=Const} = \sum_{m\in\Omega_k}^{N} \left.\frac{\partial S_k}{\partial V_k^*}\right|_{V_k=Const}, \tag{3.36}$$

$$\left.\frac{\partial M_k}{\partial V_m}\right|_{V_m^*=Const} = 0.0, \tag{3.37}$$

$$\left.\frac{\partial M_k}{\partial V_m^*}\right|_{V_m=Const} = \sum_{m\in\Omega_k}^{N} \left.\frac{\partial S_k}{\partial V_m^*}\right|_{V_m=Const}, \tag{3.38}$$

and

$$\left.\frac{\partial M_k^*}{\partial V_k}\right|_{V_k^*=Const} = \sum_{m\in\Omega_k}^{N} \left.\frac{\partial S_k^*}{\partial V_k}\right|_{V_k^*=Const}, \tag{3.39}$$

$$\left.\frac{\partial M_k^*}{\partial V_k^*}\right|_{V_k=Const} = \sum_{m\in\Omega_k}^{N} \left.\frac{\partial S_k^*}{\partial V_k^*}\right|_{V_k=Const}, \tag{3.40}$$

$$\left.\frac{\partial M_k^*}{\partial V_m}\right|_{V_m^*=Const} = \sum_{m\in\Omega_k}^{N} \left.\frac{\partial S_k^*}{\partial V_m}\right|_{V_m=Const}, \tag{3.41}$$

$$\left.\frac{\partial M_k^*}{\partial V_m^*}\right|_{V_m=Const} = 0.0. \tag{3.42}$$

Here Ω_i in (3.35-3.42) is the set of neighboring buses connected to the $k_{th}-bus$ and N is the total number of buses. Moreover, in (3.37-3.38) and (3.41-3.42), $m \neq 0$ and $m \neq k$. We highlight that the right hand side (rhs) of (3.40) is the nodal complex current at node k while the rhs of (3.35) is the complex conjugate of the nodal current at node k.

3.4.3 PV-Bus Type

As the active-power generation and the terminal voltage magnitude at a $PV-bus$ are both specified, i.e., P_{ks} and V_{ks}, respectively, the sum of M_k in (3.33) and M_k^* in (3.34) gives the complex residual function, M_{kg}, which is related to the active-power constraint as follows:

$$\begin{aligned} M_{kg} &= M_k + M_k^*, \\ &= S_k + S_k^* - 2\times P_{ks}. \end{aligned} \tag{3.43}$$

The second complex residual function E_{kg} for a generator node k is formed, using the voltage magnitude constraint given by

$$|E_{kg}| = |V_k|^2 - |V_{ks}|^2, \tag{3.44}$$

where the $|V_{ks}|$ is the specified voltage magnitude at Node k.

As $|V_k|^2 = V_k V_k^*$, (3.44) can be expressed in the complex domain as

$$E_{kg} = V_k \; V_k^* - |V_{ks}|^2, \tag{3.45}$$

and the Jacobian matrix elements associated with a Generator node k are obtained by taking the partial derivatives of the complex residual functions in (3.43) and (3.45) with respect to V_k and V_k^*, yielding

$$\left.\frac{\partial M_{kg}}{\partial V_k}\right|_{V_k^*=Const} = \left.\frac{\partial M_k}{\partial V_k}\right|_{V_k^*=Const} + \left.\frac{\partial M_k^*}{\partial V_k}\right|_{V_k^*=Const}, \tag{3.46}$$

$$\left.\frac{\partial M_{kg}}{\partial V_k^*}\right|_{V_k=Const} = \left.\frac{\partial M_k}{\partial V_k^*}\right|_{V_k=Const} + \left.\frac{\partial M_k^*}{\partial V_k^*}\right|_{V_k=Const}, \tag{3.47}$$

$$\left.\frac{\partial M_{kg}}{\partial V_m}\right|_{V_m^*=Const} = \left.\frac{\partial M_k}{\partial V_m}\right|_{V_m^*=Const} + \left.\frac{\partial M_k^*}{\partial V_m}\right|_{V_m^*=Const}, \tag{3.48}$$

$$\left.\frac{\partial M_{kg}}{\partial V_m^*}\right|_{V_m=Const} = \left.\frac{\partial M_k}{\partial V_m^*}\right|_{V_m=Const} + \left.\frac{\partial M_k^*}{\partial V_m^*}\right|_{V_m=Const}, \tag{3.49}$$

where in (3.48-3.49), $m \neq 0$ and $m \neq k$. Moreover, note that the rhs of (3.46-3.49) are defined in (3.35-3.42). On the other hand, the partial derivatives of E_{kg} in (3.45) with respect to V_k and V_k^* are expressed as

$$\left.\frac{\partial E_{kg}}{\partial V_k}\right|_{V_k^*=Const} = V_k^*, \tag{3.50}$$

$$\left.\frac{\partial E_{kg}}{\partial V_k^*}\right|_{V_k=Const} = V_k, \tag{3.51}$$

and the partial derivaives with respect to V_m and V_m^* are given by

$$\left.\frac{\partial E_{kg}}{\partial V_m}\right|_{V_m^*=Const} = 0.0, \text{ for } m \neq 0 \text{ and } m \neq k, \tag{3.52}$$

$$\left.\frac{\partial E_{kg}}{\partial V_m^*}\right|_{V_m=Const} = 0.0, \text{ for } m \neq 0 \text{ and } m \neq k, \tag{3.53}$$

3.4.4 PQV-Bus Type

This type of bus is referred to model On-Load-Tap-Changer (OLTC), which can be a phase-transformer for local and nearby bus voltage regulation or a phase-shifting-transformer for controlling the active power flow transmitted over a line [35]. It is also

suited to model a DC link of a voltage-sourced converter [36, 37]. As the active- and reactive-power demand are specified, the complex mismatches functions as stated in (3.33) and (3.34) are employed. Nonetheless, it is worth to recall that the OLTC tap position allows us to regulate the voltage magnitude at either $k-$ or $m-bus$. Let us assume that the $m-bus$ voltage is regulated, leading to the following mismatches functions:

$$M_m = a_{km} - a_{km}^* - 2 \times \Im\{a_{km}\}, \tag{3.54}$$

$$E_m = V_m \; V_m^* - |V_{ms}|^2, \tag{3.55}$$

Here $\Im\{a_{km}\}$ is the specified imaginary part of the complex tap value, e.g, for a phase-transformer, we have $\Im\{a_{km}\} = 0$; otherwise, it is a phase-shifter-transformer and instead of (3.54), (3.43) is used. In (3.55), V_{ms} is the specified voltage at node m, i.e., the regulated nodal voltage, yielding the partial derivatives of (3.54) and (3.55) given by

$$\left.\frac{\partial M_m}{\partial a_{km}}\right|_{a_{km}^*=Const} = \; 1.0, \tag{3.56}$$

$$\left.\frac{\partial M_m}{\partial a_{km}^*}\right|_{a_{km}=Const} = -1.0, \tag{3.57}$$

and

$$\left.\frac{\partial E_m}{\partial V_m}\right|_{V_m^*=Const} = \; V_m^*, \tag{3.58}$$

$$\left.\frac{\partial E_m}{\partial V_m^*}\right|_{V_m=Const} = \; V_m. \tag{3.59}$$

When (3.43) is used, the corresponding partial derivatives are those defined in (3.13-3.14) and (3.25-3.26).

3.5 Complex-Valued Iterative Solution

3.5.1 The Newton-Raphson Algorithm

When the slack bus is excluded, the state variables vector in the complex conjugate coordinate becomes

$$\underline{\mathbf{x}}_c = [V_1, V_2, \ldots, V_{N-1}, V_1^*, V_2^*, \ldots, V_{N-1}^*]^T, \tag{3.60}$$

and the mismatches vector reduces to

$$\underline{M}(\underline{\mathbf{x}}_c) = [M_1, M_2, \ldots, M_{N-1}, M_1^*, M_2^*, \ldots, M_{N-1}^*]^T. \tag{3.61}$$

If Node k (for $k = 1, 2, \ldots, N-1$) is a $PV - bus$ or a $PQV - bus$, the pair of elements M_k and M_k^* in (3.61) are replaced by M_{kg} and E_{kg} as in (3.43) and (3.45) or replaced by M_m and E_m as in (3.54) and (3.55), respectively. Here, the objective is to calculate $\underline{\mathbf{x}}_c$ that satisfies

$$\underline{M}(\underline{\mathbf{x}}_\mathbf{c}) = 0. \tag{3.62}$$

It follows that the linearization of (3.62) from one step to the sequel is given by

$$\underline{M}\left(\underline{\mathbf{x}}_\mathbf{c}{}^{(\nu-1)}\right) + \mathbf{J}\left(\underline{\mathbf{x}}_\mathbf{c}{}^{(\nu-1)}\right)\Delta\underline{\mathbf{x}}_\mathbf{c}{}^{(\nu)} = 0, \tag{3.63}$$

and

$$\underline{\mathbf{x}}_\mathbf{c}{}^{(\nu)} = \underline{\mathbf{x}}_\mathbf{c}{}^{(\nu-1)} - \left[\mathbf{J}^{(\nu-1)}\right]^{-1}\underline{M}\left(\underline{\mathbf{x}}_\mathbf{c}{}^{(\nu-1)}\right), \tag{3.64}$$

or

$$\Delta\underline{\mathbf{x}}_\mathbf{c}{}^{(\nu)} = -\left[\mathbf{J}^{(\nu-1)}\right]^{-1}\underline{M}\left(\underline{\mathbf{x}}_\mathbf{c}{}^{(\nu-1)}\right), \tag{3.65}$$

where $\mathbf{J}$ is the complex-valued Jacobian matrix in the complex conjugate coordinate. So, the update equation is given by

$$\underline{\mathbf{x}}_\mathbf{c}{}^{(\nu)} = \underline{\mathbf{x}}_\mathbf{c}{}^{(\nu-1)} + \Delta\underline{\mathbf{x}}_\mathbf{c}{}^{(\nu)}. \tag{3.66}$$

The convergence criterion can be the same that is often assumed in the $\mathbb{R}-domain$, i.e.,

$$\left\|\Delta\underline{\mathbf{x}}_c^{(\nu)}\right\|_\infty \leq tol\ (\approx 10^{-3}), \tag{3.67}$$

where $\|\cdot\|_\infty$ is defined as the infinity norm and ν is the iteration counter. In the complex domain, the convergence criterion is chosen to be the infinity norm of the $\Delta\underline{\mathbf{x}}_\mathbf{c}{}^{(\nu)}$ of the complex conjugate partition as explained next.

3.5.2 Structure of the Complex-Valued Power Flow Jacobian Matrix

The complex-valued power flow Jacobian matrix exhibits the following structure:

$$\mathbf{J} = \begin{bmatrix} \frac{\partial M_{kg}}{\partial V_k} & \frac{\partial M_{kg}}{\partial V_m} & \frac{\partial M_{kg}}{\partial a_{km}} & \frac{\partial M_{kg}}{\partial V_k^*} & \frac{\partial M_{kg}}{\partial V_m^*} & \frac{\partial M_{kg}}{\partial a_{km}^*} \\ \frac{\partial M_k}{\partial V_k} & \frac{\partial M_k}{\partial V_m} & \frac{\partial M_k}{\partial a_{km}} & \frac{\partial M_k}{\partial V_k^*} & \frac{\partial M_k}{\partial V_m^*} & \frac{\partial M_k}{\partial a_{km}^*} \\ 0.0 & 0.0 & \frac{\partial M_m}{\partial a_{km}} & 0.0 & 0.0 & \frac{\partial M_m}{\partial a_{km}^*} \\ \frac{\partial E_{kg}}{\partial V_k} & 0.0 & 0.0 & \frac{\partial E_{kg}}{\partial V_k^*} & 0.0 & 0.0 \\ \frac{\partial M_k^*}{\partial V_k} & \frac{\partial M_k^*}{\partial V_m} & \frac{\partial M_k^*}{\partial a_{km}} & \frac{\partial M_k^*}{\partial V_k^*} & \frac{\partial M_k^*}{\partial V_m^*} & \frac{\partial M_k^*}{\partial a_{km}^*} \\ 0.0 & \frac{\partial E_m}{\partial V_m} & 0.0 & 0.0 & \frac{\partial E_m}{\partial V_m^*} & 0.0 \end{bmatrix}. \tag{3.68}$$

In (3.68), the partial derivatives in the 1^{st} and 4^{th} rows correspond to $PV-buses$, those in the 2^{nd} and 5^{th} rows correspond to $PQ-buses$ and those in the 3^{th} and 6^{th} rows correspond to $PQV-buses$. In order to factorize the CV-Jacobian matrix in (3.68), two QR-algorithms are considered and investigated [38, 39]; the latter is written in polar coordinates. Both are the extension of the well-known real-valued algorithm described in [40], which was successfully applied to PSSE by [41, 42, 43]. Recall that the QR-algorithm should be applied to an augmented matrix in order to avoid explicitly storing the Q-matrix. To this end, the QR-transformation is applied to $\mathbf{J_a}$ given by

$$\mathbf{J_a}^{(\nu-1)} = \left[\mathbf{J}^{(\nu-1)} \; \underline{M}\left(\underline{\mathbf{x}}_{\mathbf{c}}{}^{(\nu-1)}\right)\right]. \tag{3.69}$$

On the other hand, it turns out that if we store the sequence of rotations in compact form, the complex-valued Jacobian matrix can be kept constant, implying that only the right-hand-side vector is updated throughout the final iterations. Here, the solution of (3.65) is reached by performing a simple back-substitution over the factorization of (3.69), yielding

$$\widetilde{\mathbf{J}}_{\mathbf{a}}^{(\nu)} \;=\; \left[\mathbf{T_c} \; \widetilde{\underline{\mathbf{M}}}_c\right], \tag{3.70}$$

where $\mathbf{T_c}$ is an upper triangular matrix of dimension - $2n \times 2n$, and $\widetilde{\underline{\mathbf{M}}}_c$ comprises the corresponding rows in the updated rhs vector, dimension - $2n \times 1$, for $n = N-1$. Then, (3.65) can be expressed through

$$\Delta\underline{\mathbf{x}}_c^{(\nu)} = \mathbf{T_c} \; \widetilde{\underline{\mathbf{M}}}_c. \tag{3.71}$$

4 Exact CV-Power Flow Analysis

The exact real-valued load flow formulation is not a new issue in the state-of-the-art literature. In order to achieve a more accurate model, Sachdev and Medicherla [44] proposed a second-order method in polar coordinates formulation. Nonetheless, this approach still neglects all the higher-order terms in Taylor's series expansion of the load flow equations. On the other hand, Iwamoto and Tamura [45] proposal is developed using rectangular coordinates and showed that no terms of Taylor's series expansion need to be neglected in their method. Moreover, the Hessian matrix calculation is not required in their proposal if all the constraint functions are quadratic.

Further enhancements to the second-order load flow were proposed by Roy and Rao [46], who showed that the use of a particular starting point and some suited approximations become his approach faster and require less memory than the fast decoupled load flow (FDLF), which was taken as the benchmark in his work. In [47] some improvements in the exact load flow formulation are suggested aiming to overcome the FDLF slow convergence rate and failures when it is carried out on systems with large R/X ratios and capacitive series branches. It is conjectured that the poor FDLF performance under those conditions might be due to the approximations made while developing the FDLF model itself. In addition, a new technique is added for handling Q limit violations at PV buses. A comparative analysis of the convergence characteristics of second-order load flow methods is conducted in [48] but focused on FDLF. More recently, in [49] a new second-order load flow method is proposed. It is based on the constant Jacobian matrix in polar coordinates and requires the Hessian matrix calculation. In any case, the algorithms regarding all works mentioned earlier are aimed to solve the exact power flow problem formulated in the real domain. This procedure is followed because the power flow equations should be written in rectangular coordinates, splitting into real and imaginary parts. So, if the mismatch equations are quadratic functions, their second-order expansion in the Taylor series is exact.

As the quadratic power flow equations in the complex plane are naturally formulated in rectangular coordinates, a second-order complex-valued power flow formulation is straightforwardly derived in this chapter. In order to present the effectiveness of the new method, three classes of algorithms are considered in this chapter and their performances are compared. The first one is the well-known Newton-Raphson method in the real domain and written in polar coordinates, which is taken as a benchmark. The second one is the generic complex-valued NR power flow as presented in Chapter 3. The third one is the proposed second-order power flow derived from Iwamoto's approach as described in [45], otherwise developed in the complex plane.

4.1 The Iwamoto's Approach in Complex Plane

The most noteworthy feature aiming the CV power flow equations expansion Taylor series is that no terms beyond the second order derivative exist because the original equations (3.5-3.8) are quadratic functions in x and x^*. Indeed, this feature is used to develop the proposed algorithm, i.e., the exact 2^{nd}-order complex-valued power flow (CV-EPF), once it allows to retain the nonlinearity without introducing any approximation or assumption into the model. Thus, without any loss of exactness, this work employs the very nice property presented by Iwamoto's approach in [45], i.e., the Hessian matrix calculation can be avoided. Consequently, the power flow problem expanded in a 2^{nd}-order Taylor's series becomes

$$\mathbf{J}\ \Delta\underline{x}_c = \underline{Y}_c^{spec} - \underline{Y}_c\left(\underline{x}_c\right) - \underline{Y}_c\left(\Delta\underline{x}_c\right), \tag{4.1}$$

where $\underline{Y}_c^{spec}$ is a vector of constant terms referred as specified quantities. $\underline{Y}_c\left(\underline{x}_c\right)$ and $\underline{Y}_c\left(\Delta\underline{x}_c\right)$ are the vector of calculated quantities and the 2^{nd}-order term of the Taylor serie expansion, respectively. Thereby, this latter is equivalent to the Hessian matrix which is complicated and of high dimensionality [45, 50]. Consequently, its calculation is advantageously avoided as described in Appendix B. Notice that the only difference between $\underline{Y}_c\left(\underline{x}_c\right)$ and $\underline{Y}_c\left(\Delta\underline{x}_c\right)$ is their argument. Writing (4.1) in terms of $\Delta\underline{x}_c$, leads to

$$\Delta\underline{x}_c = \mathbf{J}^{-1}\ \left[\ \underline{Y}_c^{spec} - \underline{Y}_c\left(\underline{x}_c\right) - \underline{Y}_c\left(\Delta\underline{x}_c\right)\ \right]. \tag{4.2}$$

As $\underline{Y}_c\left(\Delta\underline{x}_c\right)$ is function of $\Delta\underline{x}_c$, a numerical solution is needed to find the exact correction vector. Hence, (4.2) can be iteratively solved:

$$\Delta\underline{x}_c^{(\nu+1)} = \left(\mathbf{J}^{(0)}\right)^{-1}\ \left[\ \underline{Y}_c^{spec} - \underline{Y}_c\left(\underline{x}_c^{(0)}\right) - \underline{Y}_c\left(\Delta\underline{x}_c^{(\nu)}\right)\ \right]. \tag{4.3}$$

In this algorithm, the starting values assigned to the state variables stay constant throughout the iterations. Thus, also $\underline{Y}_c(\underline{x}_c^{(\nu=0)})$ and $\mathbf{J}^{(\nu=0)}$ which are functions of $\underline{x}_c^{(\nu=0)}$ remain constant during the iterative process. Consequently, only $\Delta\underline{x}_c^{(\nu+1)}$ and $\underline{Y}_c(\Delta\underline{x}_c^{(\nu)})$ change their values in the iteration process. Now, it is worth highlighting the fact that the Jacobian matrix is factorized only once, significantly lighting the computing burden. Notice that null values are assigned to $\Delta\underline{x}_c^{(\nu=0)}$ in the first iteration of the exact power flow loop [45]. Consequently, it is the former Newton-Raphson method. The recommended convergence criterion to be satisfied is

$$\left\|\Delta\underline{\mathbf{x}}_c^{(\nu+1)} - \Delta\underline{\mathbf{x}}_c^{(\nu)}\right\|_\infty \leq tol\ \left(e.g., 10^{-6}\right), \tag{4.4}$$

where $\Delta\underline{\mathbf{x}}_c$ physically means the total (or exact) voltage correction vector. Hence, the state variables updating only occurs once the convergence has been reached, yielding

$$\underline{x}_c^{(\star)} = \underline{x}_c^{(0)} + \Delta\underline{x}_c^{(\nu+1)}, \tag{4.5}$$

where $\underline{x}_c^{(\star)}$ is the solution vector for the power flow problem. Nonetheless, as any iterative process, the outcome to reach the solution is prone to the starting values assigned to the state variables. If needed, the starting point can be enhanced by making at least one iteration, e.g., through the Newton-Raphson method, as shown in Fig. 16b. Thus, (4.5) has to be re-written, leading to

$$\underline{x}_c^{(\star)} = \underline{x}_c^{(1)} + \Delta\underline{x}_c^{(\nu+1)}. \tag{4.6}$$

Fig. 16 depicts both possibilities, i.e., (4.5-4.6), where the state variables are updated only once, i.e., after the iterative process is over.

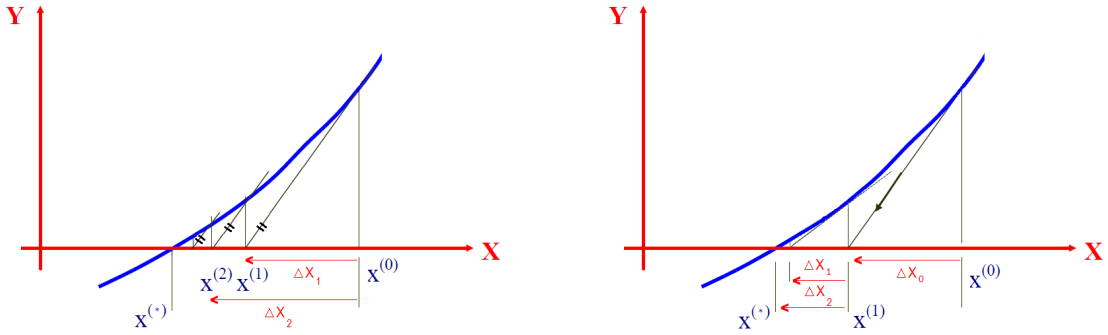

(a) Starting point; (b) Enhanced Starting point.

Figure 16 – Exact power flow solutions through Iwamoto's approach.

4.1.1 The Second-Order Complex-Valued Power Flow Formulation

In order to simplify notation, it is considered in this section a power system where all buses are PQ-buses, except, of course, the slack-bus, for which terms are removed since its voltage is known. The vector of state variables $\underline{x}_c$ is defined as in (3.60) and the correction vector $\Delta\underline{x}_c$ have the same structure. The terms of (4.3) are given by:

$$\underline{Y}_c^{spec} = \begin{bmatrix} \underline{S}^{spec} \\ \underline{S}^{*\ spec} \end{bmatrix} = \begin{bmatrix} \underline{P}^{spec} + j\ \underline{Q}^{spec} \\ \underline{P}^{spec} - j\ \underline{Q}^{spec} \end{bmatrix}, \tag{4.7}$$

$$\underline{Y}_c\left(\underline{V}_c^{(0)}\right) = \begin{bmatrix} \underline{S}\left(\underline{V}_c^{(0)}\right) \\ \underline{S}^*\left(\underline{V}_c^{(0)}\right) \end{bmatrix} = \begin{bmatrix} \underline{V}^{(0)} \odot \mathbf{Y}^*\ \underline{V}^{*(0)} \\ \underline{V}^{*(0)} \odot \mathbf{Y}\ \underline{V}^{(0)} \end{bmatrix}, \tag{4.8}$$

and

$$\underline{Y}_c\left(\Delta\underline{V}_c^{(\nu)}\right) = \begin{bmatrix} \underline{S}\left(\Delta\underline{V}_c^{(\nu)}\right) \\ \underline{S}^*\left(\Delta\underline{V}_c^{(\nu)}\right) \end{bmatrix} = \begin{bmatrix} \Delta\underline{V}^{(\nu)} \odot \mathbf{Y}^*\ \Delta\underline{V}^{*(\nu)} \\ \Delta\underline{V}^{*(\nu)} \odot \mathbf{Y}\ \Delta\underline{V}^{(\nu)} \end{bmatrix}. \tag{4.9}$$

The generalization for PV and PQV-buses is made in this same manner considering its respective constraints modeled in Chapter 3. The flow chart scheme for this algorithm

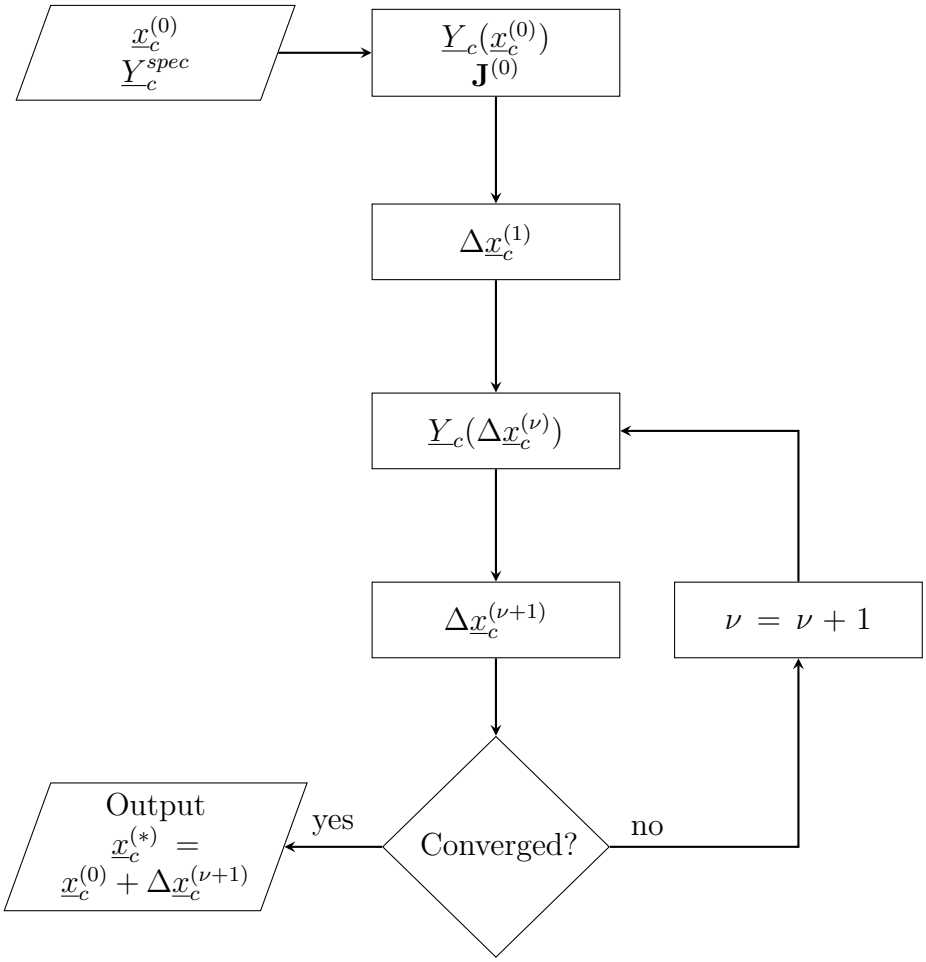

Figure 17 – Flow chart of the 2^{nd}-order CV power flow algorithm.

is illustrated in Fig. 17. It is clear now how simple is the 2^{nd}-order expansion of the CV power flow formulation when considering the Hessian equivalent function from the Iwamoto approach. The numerical performance for such implementation is evaluated in the next section.

4.2 Numerical Results

In this section, the performance of the exact CV power flow algorithm is evaluated. As described earlier, a total of three algorithms were implemented in order to compare their performances. In this section they are identified as follows:

1. RV-PFA Classic real-valued Newton-Raphson method in polar coordinates;

2. CV-PFA Complex-valued Newton-Raphson power flow as presented in Chapter 3;

3. CV-EPF Complex-valued exact 2^{nd}-order power flow algorithm.

All algorithms described here were encoded in Matlab by using the sparsity technique and column approximate minimum degree (*colamd*) ordering scheme. The numerical tests were executed by using an Intel® Core™ i5-4200 CPU @ 1.60Hz 2.30 GHz; 6GB of RAM and 64-bit operating system. A flat start condition is assigned to the state variables in all simulations. The tolerance adopted for the convergence criterion in all simulations is 10^{-6}. All simulations are carried out on the standard IEEE-14, -30, -57, and -118 bus systems, and on the SIN-1916 bus systems.

4.2.1 IEEE / SIN Test Systems

Table 1 provides the network features of the well-conditioned IEEE / SIN test systems. Whereas, Table 2 allows us to make a comparative analysis of the performance referred to all algorithms carried out on the simulations regarding the number of iterations and time consuming to reach the solution. For the CPU time comparison, the well-known real-valued Newton-Raphson method in polar coordinates is taken as the benchmark, i.e., Table 2 shows how faster the processing times are for the algorithms **2. CV-PFA** and **3. CV-EPF** compared to **1. RV-PFA**. Regardless of power system dimension, **2. CV-PFA** has shown to have a quite similar performance compared to **1. RV-PFA**, for either the number of iterations to converge and computing time. This emphasizes that modern processors can compute complex arithmetic with no apparent extra burden [4]. Due the Iwamoto's Approach characteristics, the proposed algorithm **3. CV-EPF** naturally demands more iterations to reach the solution. However, avoiding the need for building and factorizing the Jacobian matrix at each iteration allows the algorithm to be quite fast. Indeed, the simulation results have shown a better performance for **3. CV-EPF** for all test systems, especially the larger one, reaching the problem solution 2.89 times faster than the classic **1. RV-PFA** algorithm.

Table 1 – Features of the IEEE / SIN Test systems

IEEE-Test Bus Systems / SIN-	14	30	57	118	1916
No. of PV-bus (N_{PV})	4	5	6	53	163
No. of PQ-bus (N_{PQ})	9	24	50	64	1753
No. of transformers	3	4	15	9	835
No. of TL + shunt	21	43	83	200	3197
$\mathbb{R}$V-$^{(p)}$: $n = (N_{PV} + 2 \times N_{PQ})$	22	53	106	181	3669
$\mathbb{C}$V-$^{(r)}$: $n = 2 \times (N_{PV} + N_{PQ})$	26	58	112	234	3832

TL - Transmission Line

Table 2 – Performance in the IEEE/SIN test systems (tol. = 1.0×10^{-6})

	Algorithms	Number of Iters.	Time / iteration (× faster)	Total time (× faster)
IEEE-14	1. RV-PFA	3	1	1
	2. CV-PFA	3	0.97	0.88
	3. CV-EPF	7	7.61	1.58
IEEE-30	1. RV-PFA	3	1	1
	2. CV-PFA	3	1.06	0.98
	3. CV-EPF	7	8.28	1.65
IEEE-57	1. RV-PFA	3	1	1
	2. CV-PFA	3	1.07	1.03
	3. CV-EPF	9	10.45	1.50
IEEE-118	1. RV-PFA	3	1	1
	2. CV-PFA	3	1.08	1.04
	3. CV-EPF	6	9.03	1.20
SIN-1916	1. RV-PFA	6	1	1
	2. CV-PFA	6	1.01	1.07
	3. CV-EPF	26	67.24	2.89

4.3 Partial Conclusions

In this chapter is developed a complex-valued exact power flow solution (CV-EPF) by adapting the Iwamoto approach to the complex plane formulation. The proposed algorithm is compared to the well-known RV Newton-Raphson method in polar coordinates, besides the CV Newton-Raphson power flow algorithm as discussed in Chapter 3. It is shown that the proposed CV exact power flow algorithm is faster and very easily can be implemented.

5 Complex-Valued Power Flow Analysis for Hybrid AC/DC Transmission Grids

Nowadays, the ever growing need for transmission capacity in power systems, and integration with renewable energy sources and offshore grids, has led to an increased interest in transmission based on Multi-Terminal High Voltage Direct Current (MTDC) technology. MTDC emplying Voltage Source Converter (VSC) is an enhanced HVDC technology of attractive application in the industry because of their well-known advantages over conventional Current Source Commutated (CSC) [13], which allow the relatively straightforward extension of the multi-terminal configurations.

Many research efforts has been conducted on the development of a steady-state VSC MTDC model applicable to integrated AC/DC power flow algorithms. In the state-of-the-art, mainly two power flow formulations aiming to model the integrated AC/DC grids can be found. In the first, the solution method is sequential [51, 52, 53, 54, 55], while in the second, the solution is formulated in a unified fashion [56, 57, 58, 59]. In sequential methods, the AC and DC equations are solved sequentially, whereas the hybrid systems are solved together in the unified methods. Comparing their implementation effort, the sequential approach is more advantageous mainly because it allows embedding an MTDC system to an existing AC-based power flow software [60]. However, the sequential solution requires an additional iterative process to solve the DC grid power flow because its inner losses are not known a priori.

The major contribution presented in this chapter is the development of a detailed, general complex-valued (CV) VSC-MTDC steady-state model and, from that, the development of a set of hybrid AC/DC power flow solutions in complex plane. The main motivation is that the complex-valued power flow is more suited to modern processors and lends itself to an easier software implementation, as further discussed in Chapter 3. To demonstrate the CV VSC-MTDC model applicability, both sequential and unified power flow formulations for hybrid AC/DC transmission grid were developed in the complex plane.

The formulation is solved, likewise [5], by Newton's method using Wirtinger's calculus, preserving the powerful convergence property of Newton's method [8]. The full complex power flow equations with no restrictions on the topology or configuration of the AC and DC networks are assumed. Moreover, without any loss of generality, the former VSC-HVDC model showed in Fig. 18 is adopted in this chapter [52]. The main reason is that power flow equations are functions only of the network's state variables, including the

AC side of the converter. Consequently, regardless of the Newton-Raphson iterative power flow algorithms, i.e., sequential or unified approach, usually it requires fewer number of iterations to reach the solution than other equivalent algorithms which model the state variables inner the converter explicitly [61, 56]. This model also includes a representation of converter transformer, AC filter and phase reactor as a part of the converter model.

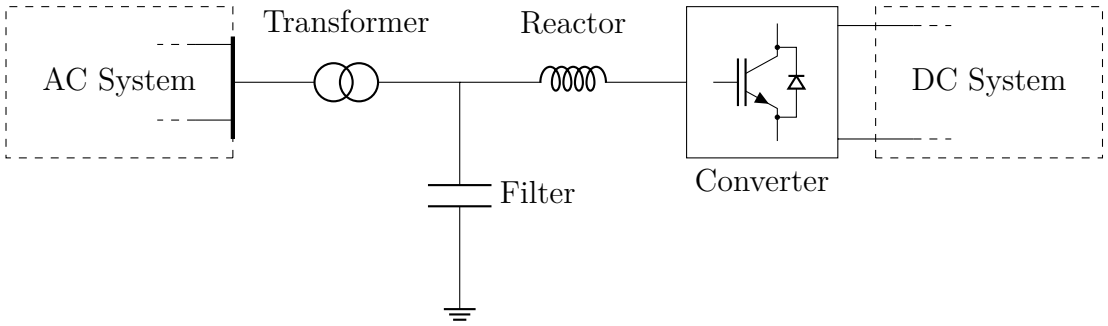

Figure 18 – VSC HVDC scheme.

5.1 The Generalized Complex-Valued VSC-MTDC Formulation

The two most basic VSC-HVDC configurations are the back-to-back and point-to-point in either monopolar or bipolar fashions. Two monopolar VSC-HVDC links are shown schematically in Fig. 19, where each converter comprises a voltage-source-converter (VSC) and an interfacing load-tap-changer (LTC) transformer, AC filter and phase reactor. Remark that the two VSCs are series-connected on their DC sides, both sharing a capacitor, in the back-to-back configuration (Fig. 19a), or a DC cable, in the point-to-point configuration (Fig. 19b). Whereas on the converters' AC side, the converter transformers are connected to the AC Point of Common Coupling (PCC), which makes each VSC to be shunt-connected with the AC system, just as if they were two STATCOM [62].

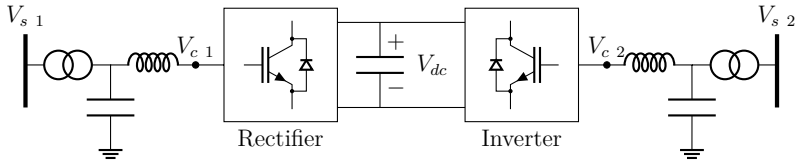

(a) Back-to-back.

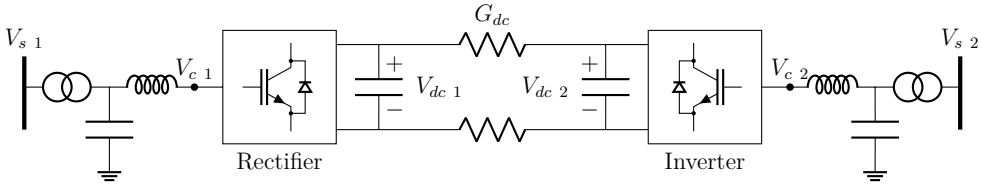

(b) Point-to-point.

Figure 19 – VSC HVDC link scheme.

The VSC-HVDC shown in Fig. 19b is extended to a generic VSC-MTDC hybrid AC/DC transmission grids' one-line diagram, depicted in Fig. 20. In spite of the VSC-HVDC, this VSC-MTDC model can be extended to any number of terminals. Furthermore, despite other FACTS devices are not shown, e.g., a battery energy storage system (BESS), a DFIG-based wind farm or a photovoltaic generation system (PV), to cite a few, they can be equally DC grid-connected.

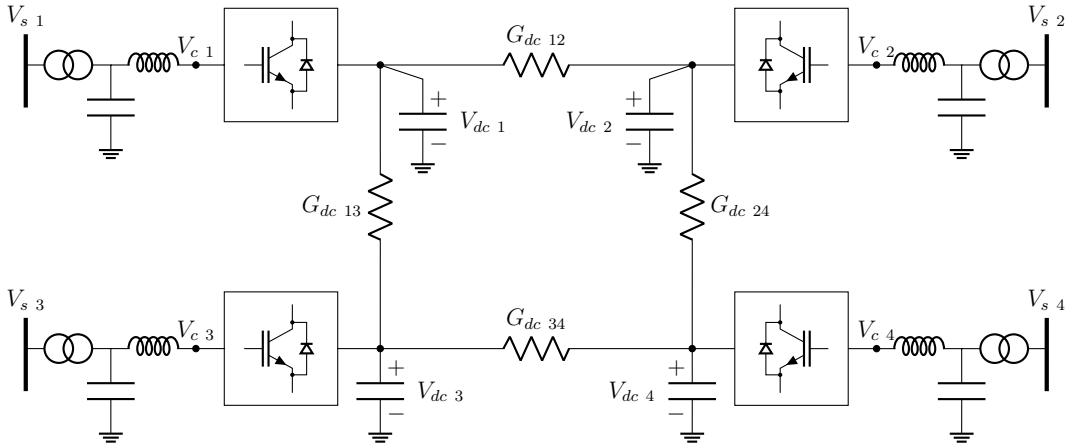

Figure 20 – VSC MTDC scheme.

5.1.1 The equivalent VSC model

The equivalent circuit of a generalized VSC-HVDC converter is presented in Fig. 21.

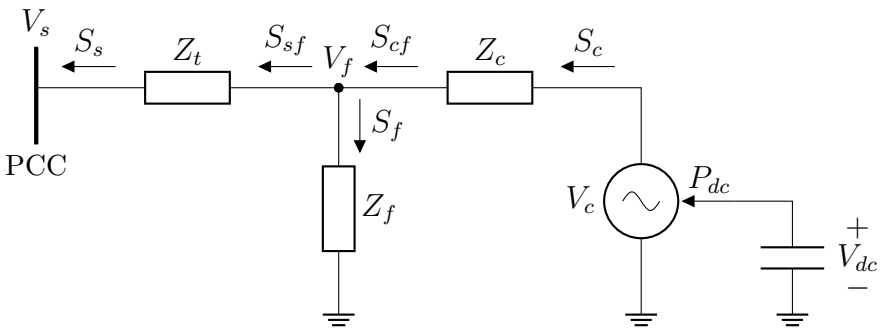

Figure 21 – VSC HVDC equivalent model.

Assuming the AC system as well the VSC are three-phase balanced, each former VSC based power flow model can be represented at the fundamental (power grid) frequency by the complex bus voltage V_c. Based on these assumptions, the general complex power flow equations at PCC and at the converter AC-terminal are:

$$S_s = V_s\ I_s^* = V_s\ Y_t^*\ (V_s^* - V_f^*), \tag{5.1}$$

and

$$S_c = V_c \; I_c^* = V_c \; Y_c^* \; (V_c^* - V_f^*), \tag{5.2}$$

while the expressions for the power flowing through the transformer, phase reactor and filter are

$$S_{sf} = V_f \; Y_t^* \; (V_f^* - V_s^*), \tag{5.3}$$

$$S_{cf} = V_f \; Y_c^* \; (V_f^* - V_c^*), \tag{5.4}$$

and

$$S_f = V_f \; Y_f^* \; V_f^*, \tag{5.5}$$

where $Y_{\{\cdot\}} = 1/Z_{\{\cdot\}}$ and $Z_{\{\cdot\}} = (R_{\{\cdot\}} + j \; X_{\{\cdot\}})$ are the impedance of the converter coupling components. The losses in the converter can be represented as a function of the reactor current magnitude I_{cm}, as first discussed in [63]:

$$P_{loss} = a + b \; I_{cm} + c \; I_{cm}^2, \tag{5.6}$$

$$\text{with} \quad I_{cm} = \frac{1}{\sqrt{3}} \sqrt{\frac{S_c \; S_c^*}{V_c \; V_c^*}}. \tag{5.7}$$

Furthermore, the sum of losses and reactive power absorption between the converter AC-terminal and PCC bus, here defined as S_{loss}, is given by

$$S_{loss} = S_c - S_s = Z_{tf} \; I_s \; I_s^* + Z_f \; I_f \; I_f^* + Z_c \; I_c \; I_c^*, \tag{5.8}$$

and the overall active power losses between the converter DC-terminal and PCC bus is named P_{losses} and given by

$$P_{losses} = P_{dc} - \Re\{S_s\} = P_{loss} + \Re\{S_{loss}\}. \tag{5.9}$$

Regarding VSC-HVDC with a Modular Multilevel Converter (MCC) topology, the filtering requirements are greatly reduced because of the generation of high-quality AC voltage [13]. Thus, AC filters might not be necessary and such conversors can be modelled as shown in Fig. 22, which leads to the following power flow equations:

$$S_s = V_s \; I_s^* = V_s \; Y_{eq}^* \; (V_s^* - V_c^*), \tag{5.10}$$

and

$$S_c = V_c \; I_c^* = V_c \; Y_{eq}^* \; (V_c^* - V_s^*), \tag{5.11}$$

where $Y_{eq} = 1/(Z_t + Z_c)$.

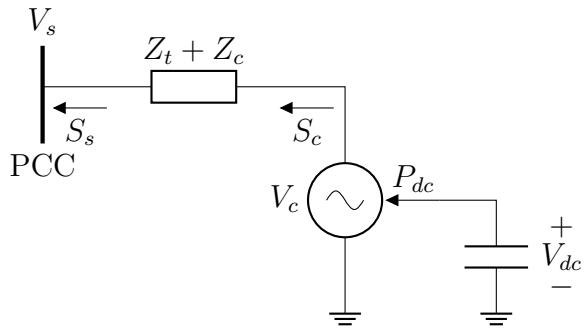

Figure 22 – MMC VSC HVDC equivalent model (no filter).

5.1.2 The VSC-MTDC control strategies

A VSC converter can independently control the active and reactive power injection into the AC system. Such technology allows different control strategies for both AC- and DC-side of the converter.

5.1.2.1 AC-side control strategies

PQ-constraint mode

The converters setted in this mode model the active and reactive HVDC power absorptions as seen from the AC network. They are under the following complex power constraints:

$$S_s - S_s^{spec} = 0 \tag{5.12}$$

and

$$S_s^* - S_s^{*\ spec} = 0, \tag{5.13}$$

where $S_s^{spec} = (P_s^{spec} + j\ Q_s^{spec})$ is the complex power specified at the converter corresponding PCC bus.

PV-constraint mode

Here, the VSC is under the active power flow constraint and adapts the reactive power injection to obtain a constant AC bus voltage magnitude. Thus, the complex power control established in (5.12, 5.13) have to be replaced by

$$S_s + S_s^* - 2 \times P_s^{spec} = 0 \tag{5.14}$$

and

$$V_s\ V_s^* - (V_s^{spec})^2 = 0. \tag{5.15}$$

5.1.2.2 DC-side control strategies

Very often the converters under power constraint are referred to as *primary converters*. In turn, the converters that control the active power flow in order to sustain the DC voltage are referred to as *secondary converters* [37, 57], and hereafter also referred as *sec-conv* for short. In this section, two DC voltage control strategies are discussed, as follows.

Constant DC Voltage Control

The converter responsible to control the DC Voltage adapts its AC active power flow constraint, which is injected into the DC bus in order to establish the DC Voltage under the following constraint:

$$V_{dc}\, V_{dc}^{*} - (V_{dc}^{spec})^2 = 0, \tag{5.16}$$

which is equivalent to

$$V_{dc} - V_{dc}^{spec} = 0, \tag{5.17}$$

where: $V_{dc} = (V_{dc} + j\ 0.0)$. This feature allows us to infer that the DC network constraints functions are analytic or holomorphic functions, i.e., they are not function of their complex conjugate state variables. Thereby, the Cauchy-Riemann equations hold (please, see Section II of [11]), and only the complex DC state variable, i.e., $V_{dc} = (V_{dc} + j\ 0.0)$, is needed to solve the problem posed in (3.62). This property applies to every DC-side constraint, once all its variables has null imaginary values in the complex plane.

Notice this converter plays the role of a *slack bus* for the DC grid, and hereafter will be referred as so. The rest constraint, i.e., the active power exchange balance among the n converters coupled through the DC network, including their losses, leads to

$$\sum P_{dc} = \ P_{dc,1} + P_{dc,2} + ... + P_{dc,n} + \sum P_{dc\ loss} = 0. \tag{5.18}$$

Voltage Droop Control

The reliability of the dc grid can be significantly enhanced by droop control since multiple converters can simultaneously contribute to the dc voltage stability. Various types of dc voltage droop characteristics, including voltage-power (V-P) droop [31, 64], voltage-current (V-I) droop [65] and voltage droop with different dead-bands and limits [66], have been proposed for MTDC. Although firstly addressed for dynamic studies, the steady-state aspect of those droop techniques is detailed in [55].

A basic V-P droop characteristic is shown in Fig. 23a. Generally, if V-P droop is employed by a dc grid of n buses, the power flow problem can be described as how to

solve the operating point of the system with a series of k specified V-P characteristics and $(n-k)$ given nodal or branch powers. If the V-P droop is used for terminal, the converter rectifying power would be controlled according to

$$P_{dc,i} = K_i \ (V_{dc,i}^{ref} - V_{dc,i}) + P_{dc,i}^{ref}, \tag{5.19}$$

where K_i is the droop control gain, which indicates the sensitivity of the converter power to the local dc voltage. By setting K to zero, a VSC terminal in power control mode or with known power generation can also be represented by (5.19). This feature of V-P droop makes it easier to analyze the power flow of the DC grid in a more generic way. Furthermore, the droop characteristics could be a combination of multiple linear or nonlinear functions of DC voltage, increasing the voltage control capability. For instance, when the voltage droop with a power dead-band shown in Fig. 23b is implemented, the scheduled power will be produced by the converter as the dc voltage is maintained close to its nominal value. Once the voltage exceeds the dead-band zone, the converter power will adjust to contribute to the stabilization of the dc grid.

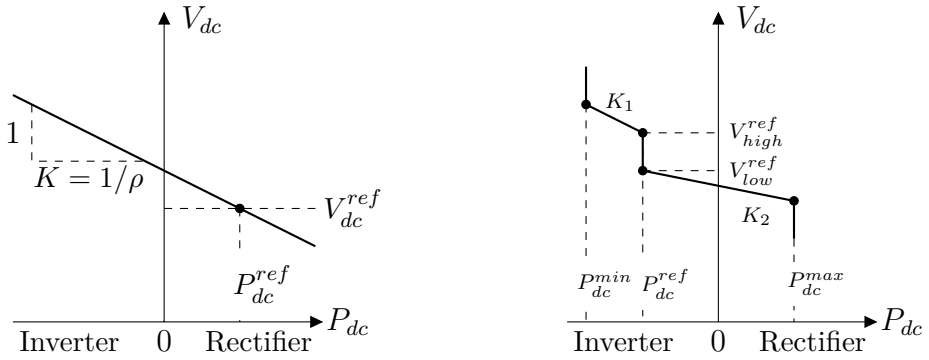

(a) Basic V-P droop (b) V-P droop with dead-band.

Figure 23 – V-P droop characteristics.

5.1.3 The DC network power flow formulation

The DC networks is represented by a resistive network with current injections. The power flow equations of a DC grid may be represented by

$$\underline{P}_{dc} = p \cdot \underline{V}_{dc} \odot (\mathbf{Y}_{dc} \ \underline{V}_{dc}), \tag{5.20}$$

where $\mathbf{Y}_{dc}$ is the DC network nodal admittance matrix; $\underline{V}_{dc}$ is the DC bus voltage vector which in expanded form is $\underline{V}_{dc} = [V_{dc,1}; V_{dc,2}; ...; V_{dc,n}]^T$ and $\underline{P}_{dc}$ is the DC network bus active power injection vector, represented by $\underline{P}_{dc} = [P_{dc,1}; P_{dc,2}; ...; P_{dc,n}]^T$ for n buses; $p = 1$ for a monopolar system or $p = 2$ for a monopolar symmetrically grounded or bipolar system; and $\odot$ the Handamard or element-wise product.

5.2 The Complex-Valued AC/DC Sequential Algorithm (CV-ADS)

Currently, Beerten's work [51] is still one of the most cited sequential AC/DC power flow in the state-of-art, and in [52] he extends his proposal to a more generalized VSC model, as considered in this chapter. In the light of that, in this section a Complex-Valued VSC-MTDC Power Flow Algorithm is developed following the same principals aiming to emphasise the generality of the CV power flow models.

In order to simplify notation, it is assumed in this section that interconnected AC and DC buses have the same bus number, all interconnected with VSC converters. For convenience, the analysis will be confined to one AC grid and one DC grid with n buses each and n converters, of which k control the DC voltage ($k = 1$ or $1 < k \leq 2$ for a MTDC with slack or droop voltage control, respectively). The method can easily be extended to include multiple AC and DC grids.

In the sequential approach, the DC grid variables are used as inputs to solve the AC equations and vice versa, which allows an easy embeddedness of DC grids into existing AC power flow programs. Fig. 24 shows the flow chart of the sequential power flow algorithm. Thus, each network, i.e., the DC as well as the AC network have to be solved iteratively. Due to the converters loss inclusion, an extra inner loop is required to calculate the secondary converter active power injections as a result of the nonlinear DC power flow solution, which is described below in this section. After that, the former iteration is needed to ensure the overall solution converges while the overall power flow solution changes due to the updates of the DC slack bus power injection. Further formulation details of the sequential hybrid power flow can be tracked in [51, 54].

5.2.1 AC network power flow

The non-linear set of power flow equations for all AC buses can be solved using the CV-PFA described in Chapter 3. However, the converters AC-side constraints must be included at the AC buses they are connected on, described as follows.

The converter complex and complex-conjugated power injections, S_s and S_s^*, are included in the power mismatch vectors M and M^* as negative loads. The power mismatch vectors from (3.33)-(3.34) can be rewritten as

$$M = S - (P^{spec} + j\ Q^{spec}) - S_s, \tag{5.21}$$

$$M^* = S^* - (P^{spec} - j\ Q^{spec}) - S_s^*. \tag{5.22}$$

The specified active power injection of a converter setted as DC slack bus is changed in order to control the DC grid voltages. As a first estimate to initiate the iteration, the DC system is assumed to be lossless, hence

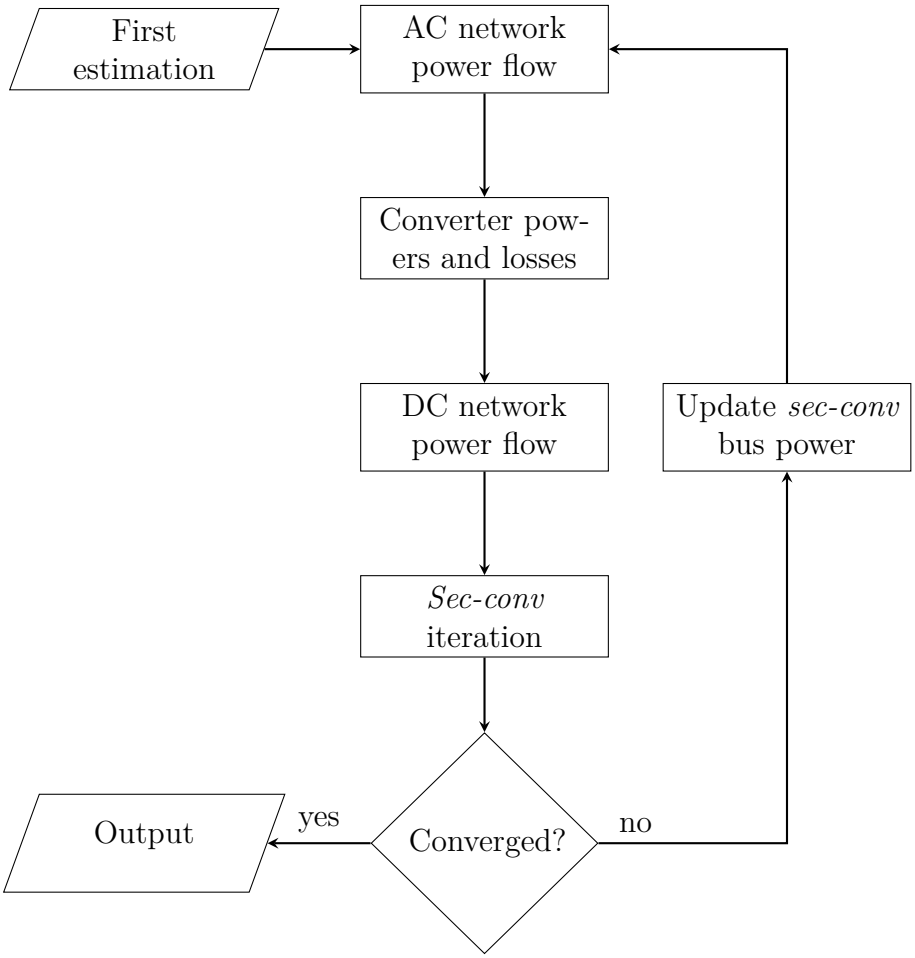

Figure 24 – Flow chart of the sequential VSC AC/DC power flow algorithm.

$$P_{s,slack}^{(0)} = -\sum_{i \neq slack}^{k} P_{s,i}. \tag{5.23}$$

For subsequent iterations, the solution from the previous iteration is used for $P_{s,slack}$.

Furthermore, converters in PV-constraint mode are represented as AC generators and their respective AC buses are changed from PQ-nodes to PV-nodes.

5.2.2 Converter Calculations

With each converter voltage V_s and power injection S_s at PCC known, the converter side voltage and currents can be calculated. For the VSC model in Fig. 21, the filter bus voltage V_f can be written as

$$V_f = V_s + Z_t \; I_s, \tag{5.24}$$

where

$$I_s = \frac{S_s^*}{V_s^*}. \tag{5.25}$$

The converter current I_c is calculated as

$$I_c = I_s + \frac{V_f}{Z_f}, \tag{5.26}$$

which magnitude, denoted as I_{cm}, can be substituted in (5.6) to calculate the converter losses. The converter voltage V_c can be calculated as

$$V_c = V_f + Z_c\ I_c. \tag{5.27}$$

The power injection at the converter terminal is given by

$$S_c = V_c\ I_c^*. \tag{5.28}$$

With all quantities on the AC side known, the DC grid's injected power becomes

$$P_{dc} = -\Re\{S_c\} - P_{loss}. \tag{5.29}$$

5.2.3 DC network power flow

The non-linear DC network equations from (5.20) can be solved with a NR method

$$\mathbf{J}_{dc}\ \Delta\underline{V}_{dc} = \Delta\underline{P}_{dc}. \tag{5.30}$$

The power mismatch vector $\Delta\underline{P}_{dc}$ is given by

$$\Delta\underline{P}_{dc} = \underline{P}_{dc}^{ref} + \underline{K}\ \left(\underline{V}_{dc}^{ref} - \underline{V}_{dc}\right) - \underline{P}_{dc}\left(\underline{V}_{dc}\right), \tag{5.31}$$

where $\underline{P}_{dc}\left(\underline{V}_{dc}\right)$ is calculated from (5.20) in each inner DC iteration and $\underline{P}_{dc}^{ref}$ is given by (5.29) from the outer iteration. $\underline{K}$ is the droop control gain vector, represented by $\underline{K} = [K_1; K_2; ...; K_k]^T$, which has *null* values for the converters not setted in droop control mode.

The Jacobian matrix $\mathbf{J}_{dc}$ is

$$\mathbf{J}_{dc} = \frac{\partial \mathbf{P}_{dc}}{\partial \mathbf{V}_{dc}} = p \cdot \mathbf{Y}_{dc} \odot \underline{V}_{dc}^T + \mathbf{K}, \tag{5.32}$$

with $\mathbf{K}$ being the diagonal matrix of the vector $\underline{K}$.

Similar to the AC power flow, the equations and terms corresponding to the DC slack bus are removed since its voltage is given by (5.17). After convergence, the voltages on all DC buses are known, while the resulting secondary converter power injections can be found using (5.20).

5.2.4 Secondary converter iteration

After calculating the DC network, the complex power $S_{s,k}$ injected into the AC grid by each secondary converter k is calculated from its DC power $P_{dc,k}$ by accounting for the converter and components losses. As the losses from (5.6) and (5.8) depend on the converter state variables, which in turn depend on $S_{s,k}$, an additional iteration is needed. The procedure put forward in this section uses the previous AC grid state to calculate the secondary converter power injection $S_{s,k}$, i.e., the voltage at the PCC of each secondary converter $V_{s,k}$ is kept constant since it is the solution for the iteration cycle under consideration.

This additional iteration is depicted in Fig. 25. The subscript k to indicate a secondary converter has been omitted to simplify the notation. To start the iteration, an initial estimate is needed for the converter side active power injection. Using the power injection resulting from the DC power flow and an initial estimation of the converter losses P_{loss} deducted from the results of the AC network power flow in the overall iteration cycle, S_c is updated by

$$S_c = P_{dc} - P_{loss} + j\ \Im\{S_s + S_{loss}\}. \tag{5.33}$$

A NR iteration based on V_c and V_f as variables is internally used to update the converter losses:

$$\begin{bmatrix} \frac{\partial S_c}{\partial V_c} & 0 & \frac{\partial S_c}{\partial V_c^*} & \frac{\partial S_c}{\partial V_f^*} \\ 0 & \frac{\partial S_f}{\partial V_f} & \frac{\partial S_f}{\partial V_c^*} & \frac{\partial S_f}{\partial V_f^*} \\ \frac{\partial S_c^*}{\partial V_c} & \frac{\partial S_c^*}{\partial V_f} & \frac{\partial S_c^*}{\partial V_c^*} & 0 \\ \frac{\partial S_f^*}{\partial V_c} & \frac{\partial S_f^*}{\partial V_f} & 0 & \frac{\partial S_f^*}{\partial V_f^*} \end{bmatrix} \begin{bmatrix} \Delta V_c \\ \Delta V_f \\ \Delta V_c^* \\ \Delta V_f^* \end{bmatrix} = \begin{bmatrix} \Delta S_c \\ \Delta S_f \\ \Delta S_c^* \\ \Delta S_f^* \end{bmatrix}. \tag{5.34}$$

The power mismatches ΔS_c and ΔS_f can be calculated by

$$\Delta S_c = S_c - S_c(V_c, V_c^*, V_f^*), \tag{5.35}$$

$$\Delta S_f = 0 - S_f(V_c^*, V_f, V_f^*), \tag{5.36}$$

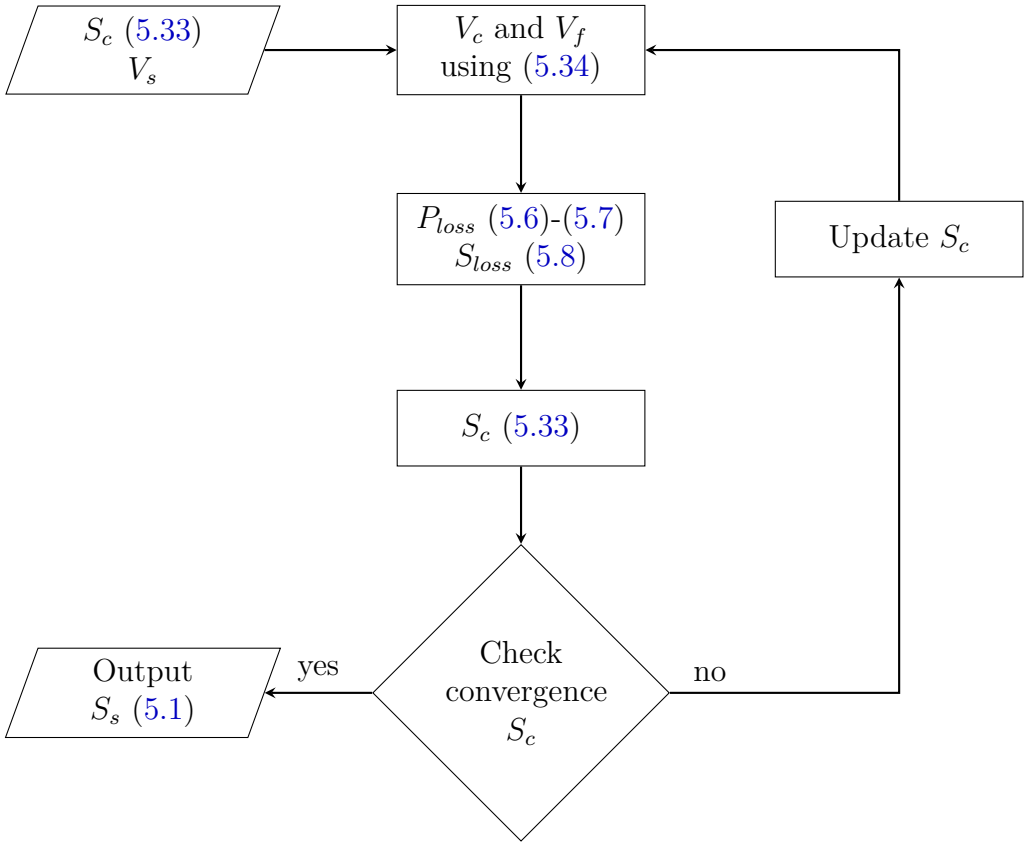

Figure 25 – Secondary converter iteration flow chart.

where $S_c(V_c, V_c^*, V_f^*)$ is from (5.2) and $S_f(V_c^*, V_f, V_f^*)$ is given by

$$S_f(V_c^*, V_f, V_f^*) = V_f \ \left(Y_{ff}^* \ V_f^* - Y_t^* \ V_s^* - Y_c^* \ V_c^*\right), \tag{5.37}$$

with $Y_{ff} = Y_t + Y_c + Y_f$.

The elements of the Jacobian matrix can be analytically derived from (5.2) and (5.37) directly. The resulting derivations are given in the following set of equations:

$$\frac{\partial S_c}{\partial V_c} = Y_c^* \left(V_c^* - V_f^*\right), \qquad \frac{\partial S_f}{\partial V_f} = Y_{ff}^* V_f^* - Y_t^* V_s^* - Y_c^* V_c^*,$$
$$\frac{\partial S_c}{\partial V_c^*} = V_c Y_c^*, \qquad \frac{\partial S_f}{\partial V_f^*} = V_f Y_f^*,$$
$$\frac{\partial S_c^*}{\partial V_c} = V_c^* Y_c, \qquad \frac{\partial S_f^*}{\partial V_f} = V_f^* Y_f,$$
$$\frac{\partial S_c^*}{\partial V_c^*} = Y_c \left(V_c - V_f\right), \qquad \frac{\partial S_f^*}{\partial V_f^*} = Y_{ff} V_f - Y_t V_s - Y_c V_c,$$

$$\frac{\partial S_c}{\partial V_f} = 0, \qquad \frac{\partial S_f}{\partial V_c} = 0,$$
$$\frac{\partial S_c}{\partial V_f^*} = -V_c Y_c^*, \qquad \frac{\partial S_f}{\partial V_c^*} = -V_f Y_c^*,$$
$$\frac{\partial S_c^*}{\partial V_f} = -V_c^* Y_c, \qquad \frac{\partial S_f^*}{\partial V_c} = -V_f^* Y_c,$$
$$\frac{\partial S_c^*}{\partial V_f^*} = 0, \qquad \frac{\partial S_f^*}{\partial V_c^*} = 0.$$

After a convergence of S_c, the power injected into the AC network S_s is calculated (Fig. 25) and thereafter checked for convergence in the overall iteration loop (Fig. 24).

5.3 A Simplified Complex-Valued AC/DC Sequential Algorithm (CV-ADS-S)

The Sequential Algorithm as presented above has a deep concern on calculating the most exact correction possible for the complex power $S_{s,k}$ injected into the AC grid by a secondary converter k at each global iteration. This calculation requires the third inner NR iteration described in subsection 5.2.4. In this section, as suggested in [60], a modification on the sequential algorithm [51] is made: an approximated correction for the $S_{s,k}$ is calculated aiming to dismiss the need for the secondary converter iteration and, consequently, making the sequential algorithm faster and easier to implement.

The algorithm structure remains the same as shown in Fig. 24, only the *sec-conv* iteration is substituted by the *sec-conv* calculation as follows.

5.3.1 Secondary converter calculation

After calculating the DC network, the complex power $S_{s,k}$ injected into the AC grid by each secondary converter k is calculated from its DC power $P_{dc,k}$ by accounting for

the overall converter losses. Regard that, even though the losses from (5.9) depend on the converter state variables, the correction of those losses is significantly small, even more if compared with the magnitude of the power injected. Thus, the procedure put forward in this section uses the previous converter losses to calculate the power injection $S_{s,k}$. By doing so, the whole *sec-conv* iteration can be replaced by this single calculation:

$$S_{s,k} = -P_{dc,k} - P_{losses,k} + j\ \Im\{S_{s,k}\}. \tag{5.38}$$

5.3.2 Another considerations on the sequential algorithm

One of the main advantages of the sequential algorithms over the unified ones is the easy embedding into existing AC power flow programs, as mentioned earlier. However, for implementations where the AC power flow is built into the algorithm, the converters' calculations can run together with the AC and DC iterations. In practice, this means that no inner iterations are needed at all. In other words, the AC grid, the converters, and the DC grid state variables are still computed sequentially, but under only the global iteration, allowing the algorithm to be even faster. The flow chart in this case, still similar to Fig. 24, is better represented by Fig. 26.

The sequential algorithm built this way gets real close to a unified one, in terms of either structure or performance. In fact, it might be considered as unified once it is not a sequence of inner iterations anymore, although the AC and DC state variables corrections are still calculated sequentially. However, by going further and coupling the AC and DC system equations in a single NR power flow, the algorithm would definitely become a unified one. From that, the following Unified AC/DC Power Flow is straightforwardly developed.

5.4 The Complex-Valued AC/DC Unified Algorithm (CV-ADU)

In the literature, a several number of different VSC-MTDC unified power flow models can be found. Although each one might use a singular model for the hybrid AC/DC problem, they all can be summarized in the following NR linearization:

$$\begin{bmatrix} \mathbf{J}_{ac} & \mathbf{J}_{ac/vsc} & \mathbf{J}_{ac/dc} \\ \mathbf{J}_{vsc/ac} & \mathbf{J}_{vsc} & \mathbf{J}_{vsc/dc} \\ \mathbf{J}_{dc/ac} & \mathbf{J}_{dc/vsc} & \mathbf{J}_{dc} \end{bmatrix} \begin{bmatrix} \Delta\underline{V}_{ac} \\ \Delta\underline{V}_{vsc} \\ \Delta\underline{V}_{dc} \end{bmatrix} = \begin{bmatrix} \Delta\underline{S}_{ac} \\ \Delta\underline{S}_{vsc} \\ \Delta\underline{P}_{dc} \end{bmatrix}, \tag{5.39}$$

which terms, in general, are described as:

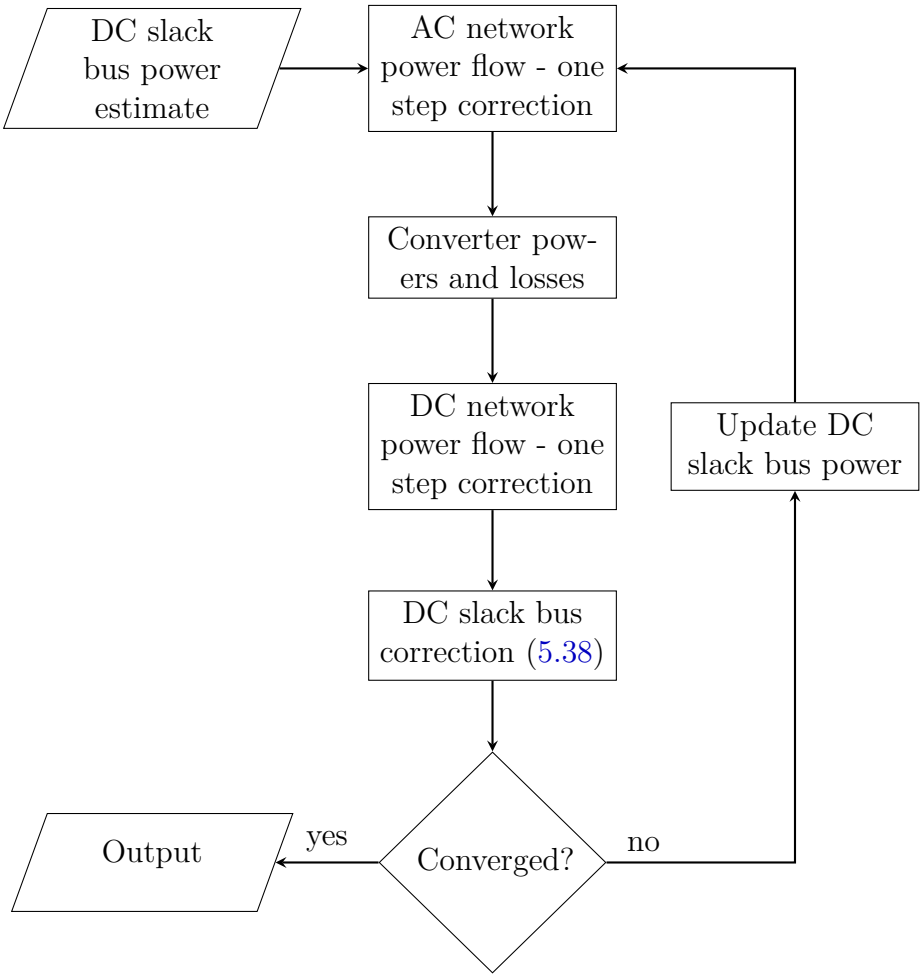

Figure 26 – Flow chart of the sequential VSC AC/DC power flow algorithm.

$\Delta\underline{V}_{ac}$ incremental vector of complex and complex conjugate AC network state variables, which in expanded form is $\Delta\underline{V}_{ac} = [\Delta V_1; \Delta V_2; ...; \Delta V_n; \Delta V_1^*; \Delta V_2^*; ...; \Delta V_n^*]^T$, for n AC buses;

$\Delta\underline{V}_{vsc}$ incremental vector of complex and complex conjugate converters state variables, which in expanded form is $\Delta\underline{V}_{vsc} = [\Delta V_{c,1}; \Delta V_{c,2}; ...; \Delta V_{c,n}; \Delta V_{c,1}^*; \Delta V_{c,2}^*; ...; \Delta V_{c,n}^*]^T$, for n converters;

$\Delta\underline{V}_{dc}$ incremental vector of complex DC network state variables, which in expanded form is $\Delta\underline{V}_{dc} = [\Delta V_{dc,1}; \Delta V_{dc,2}; ...; \Delta V_{dc,n}]^T$, for n DC buses;

$\Delta\underline{S}_{ac}$ AC network bus complex and complex conjugate power mismatches, which in expanded form is $\Delta\underline{S}_{ac} = [\Delta S_1; \Delta S_2; ...; \Delta S_n; \Delta S_1^*; \Delta S_2^*; ...; \Delta S_n^*]^T$;

$\Delta\underline{S}_{vsc}$ Converters complex and complex conjugate power mismatches, which in expanded form is $\Delta\underline{S}_{vsc} = [\Delta S_{c,1}; \Delta S_{c,2}; ...; \Delta S_{c,n}; \Delta S_{c,1}^*; \Delta S_{c,2}^*; ...; \Delta S_{c,n}^*]^T$;

$\Delta\underline{P}_{dc}$ DC network bus power mismatches, which in expanded form is $\Delta\underline{P}_{dc} = [\Delta P_1; \Delta P_2; ...; \Delta P_n]^T$;

$\mathbf{J}_{\{\cdot\}}$ The Jacobians of each subsystem;

$\mathbf{J}_{\{\cdot\}/\{\cdot\}}$ The Jacobians of each combination of subsystems.

This is an overall representation in complex plane for the unified algorithms present in the state-of-art. The linearized problem may vary according to the specific model adopted in each proposal. In the Baradars' proposal [59], for instance, the converters state variables are calculated separately, except the power losses for the ones assigned for the DC voltage control, reducing the size of the problem. However, in all cited proposals, the Jacobian of the combined subsystems has to be constructed and it is done by an arduous algebra task, which makes the implementation more complex compared to the sequential method [60]. However, the considerations on the sequential method stated in Section 5.3 allow the implementation of a much simpler linearization of the AC/DC power flow equations, as shown bellow:

$$\begin{bmatrix} & & & 0 & \cdots & 0 \\ & \mathbf{J}_{ac} & & \vdots & \ddots & \vdots \\ & & & 0 & \cdots & 0 \\ & & & & & \\ 0 & \cdots & 0 & & & \\ \vdots & \ddots & \vdots & & \mathbf{J}_{dc} & \\ 0 & \cdots & 0 & & & \end{bmatrix} \begin{bmatrix} \Delta \underline{V}_{ac} \\ \\ \Delta \underline{V}_{dc} \end{bmatrix} = \begin{bmatrix} \Delta \underline{S}_{ac} \\ \\ \Delta \underline{P}_{dc} \end{bmatrix}. \tag{5.40}$$

Here, the Jacobian matrix is directly built by coupling the AC and DC network Jacobians, respectively $\mathbf{J}_{ac}$ from (3.68) and $\mathbf{J}_{dc}$ from (5.32). Similar to Baradar's unified method [59], the converters' state variables are assumed constant in this set of power flow equation and are calculated separately. In addition to that, so are the losses on the converters in DC voltage control mode. With this, the need for deriving the power flow equations of the combined subsystems is avoided.

Thereafter, the Jacobian has null elements interconnecting the AC and DC systems, resulting in a perfectly decouplable system. Although factorizing two decoupled matrices instead of a larger one can be faster for some applications. Whereas, in hybrid AC/DC systems the DC system is usually much smaller than the AC grid, which in turn makes the factorizing of the coupled Jacobian more effective.

The converters' state variables, losses and power injections are calculated in the same way as described for the sequential algorithm. Fig. 27 shows the flow chart for this unified power flow algorithm.

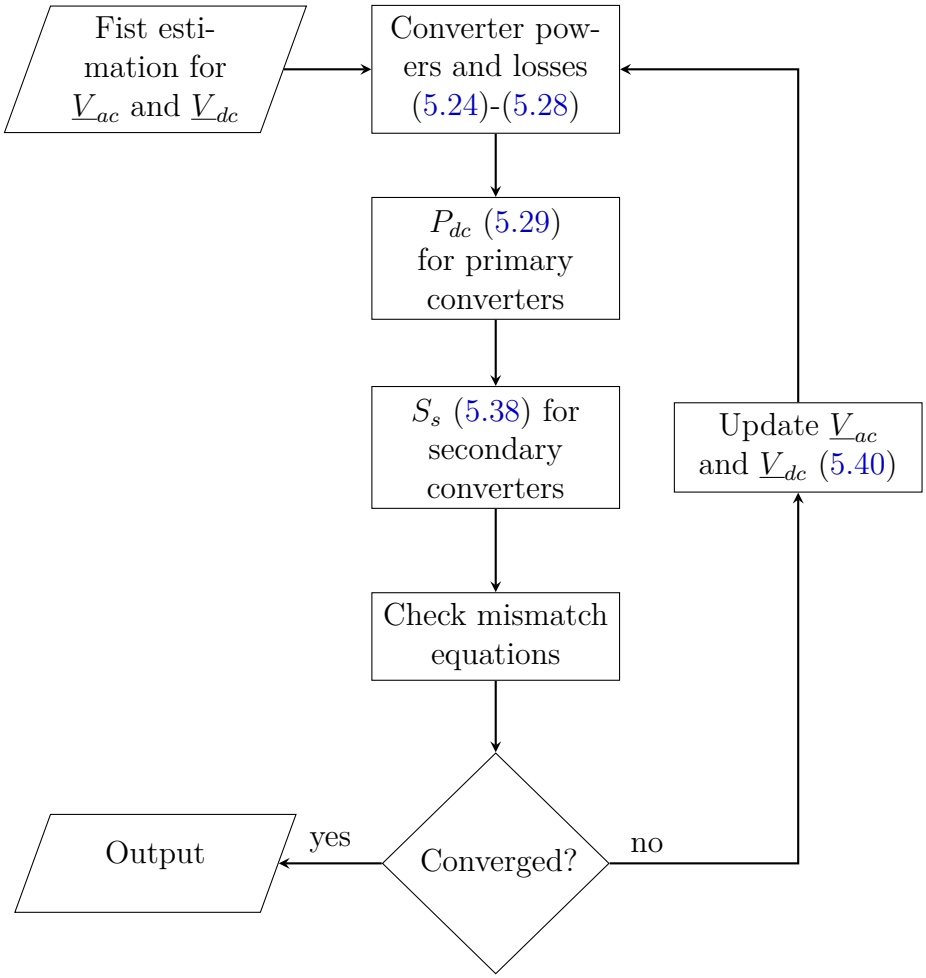

Figure 27 – Flow chart of the unified VSC AC/DC power flow algorithm.

5.5 The Exact Complex-Valued AC/DC Unified Algorithm (CV-ADU-E)

As discussed above, the unified AC/DC power flow algorithm has, by definition, both AC and DC power flow problems comprised in one single Newton-Raphson iterative formulation, although the converter state variables can be updated aside. Furthermore, by formulating the unified method in the complex plane, the set of equations to be solved is fully quadratic.

With such distinct characteristics, a the unified AC/DC power flow formulation, as presented in Section 5.4 above, can be easily expanded in a second-order Taylor series in order to find the exact state variables correction vector in a faster algorithm. Thus, in this section a 2^{nd}-order Unified AC/DC Power Flow is proposed. This is done by applying the Iwamoto approach as it was applied in the complex-valued AC power flow in Chapter 4, although one correction step is required as described below.

The iterative solution for a 2^{nd}-order Taylor series expanded problem is summarized in solving the problem given by (4.3), reproduced here for better convenience:

$$\Delta \underline{x}_c^{(\nu+1)} = \left(\mathbf{J}^{(0)}\right)^{-1} \left[\underline{Y}_c^{spec} - \underline{Y}_c\left(\underline{x}_c^{(0)}\right) - \underline{Y}_c\left(\Delta \underline{x}_c^{(\nu)}\right) \right]. \tag{5.41}$$

In therms of the proposed unified method, (5.41) can be rewritten as:

$$\begin{bmatrix} \Delta \underline{V}_{ac}^{(\nu+1)} \\ \Delta \underline{V}_{dc}^{(\nu+1)} \end{bmatrix} = \left(\mathbf{J}_{ac/dc}^{(0)}\right)^{-1} \left(\begin{bmatrix} \underline{S}_{ac}^{spec}\left(\underline{P}_{losses}^{(\nu)}\right) \\ \underline{P}_{dc}^{spec}\left(\underline{P}_{losses}^{(\nu)}\right) \end{bmatrix} - \begin{bmatrix} \underline{S}_{ac}\left(\underline{V}_{ac}^{(0)}\right) \\ \underline{P}_{dc}\left(\underline{V}_{dc}^{(0)}\right) \end{bmatrix} - \begin{bmatrix} \underline{S}_{ac}\left(\Delta \underline{V}_{ac}^{(\nu)}\right) \\ \underline{P}_{dc}\left(\Delta \underline{V}_{dc}^{(\nu)}\right) \end{bmatrix} \right). \tag{5.42}$$

Regard that, differently from the original Iwamoto approach, the vector of specified values is not constant for the proposed unified method. For instance, a primary converter who controls the active power at PCC will have its DC-side power specified by $P_{dc}^{spec} = -\Re\{S_s^{spec}\} - P_{losses}$. In turn, the converters on DC voltage control mode will specify the active power injection into PCC by (5.38), according to the demanded active power from the DC grid and accounting its respective losses.

For calculating those losses and correct the specified values, the DC and the converters state variables must be updated through the iteration process by

$$\begin{bmatrix} \underline{V}_s^{(\nu)} \\ \underline{V}_{dc}^{(\nu)} \end{bmatrix} = \begin{bmatrix} \underline{V}_s^{(0)} \\ \underline{V}_{dc}^{(0)} \end{bmatrix} + \begin{bmatrix} \Delta \underline{V}_s^{(\nu)} \\ \Delta \underline{V}_{dc}^{(\nu)} \end{bmatrix}. \tag{5.43}$$

Where $\underline{V}_s$ and $\Delta \underline{V}_s$ refer to the state variables of the PCC buses and are therms in $\underline{V}_{ac}$ and $\Delta \underline{V}_{ac}$, respectively. Notice that, in this iteration process, those state variables are updated from its initial guess. With those considerations, the 2^{nd}-order Unified AC/DC Power Flow Algorithm can be summarized in Fig. 28.

5.6 Numerical Results

In this chapter, four Complex-Valued Newton-Raphson Power Flow formulations were proposed for solving the VSC-MTDC hybrid AC/DC power flow, and they are identified as follows:

1. **CV-ADS** The full sequential algorithm with an internal loop for solving the secondary converters power and losses, as detailed in Section 5.2;

2. **CV-ADS-S** The same sequential algorithm, but without this former inner loop, as discussed in Section 5.3;

3. **CV-ADU** The unified algorithm as proposed in Section 5.4.

4. **CV-ADU-E** The 2^{nd}-order unified algorithm as proposed in Section 5.5.

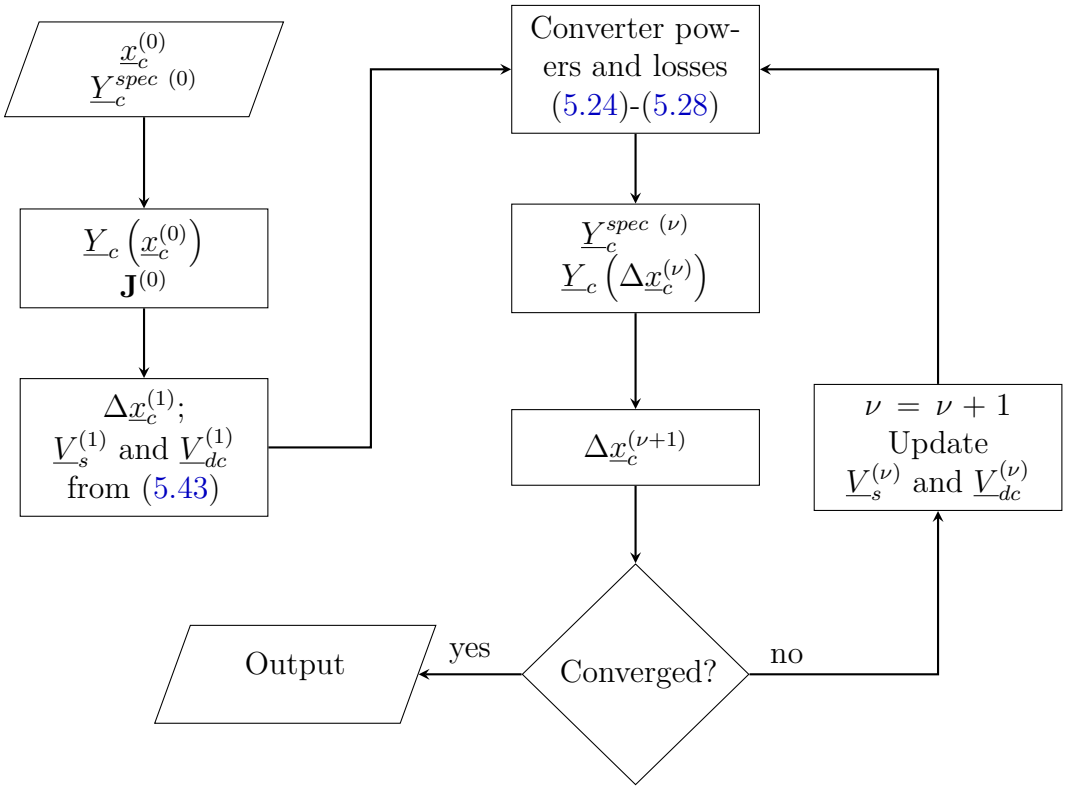

Figure 28 – Flow chart of the 2^{nd}-order unified VSC AC/DC power flow algorithm.

All algorithms described here were encoded in Matlab by using sparsity technique and column approximate minimum degree (*colamd*) ordering scheme. The numerical tests were executed by using an Intel® Core™ i5-4200 CPU @ 1.60Hz 2.30 GHz; 6GB of RAM and 64-bit operating system. Two hybrid AC/DC test systems were simulated: a modified IEEE Two Area RTS-96 test system with two coupled MTDC networks, duplicated here from [52], and a proposed test system as presented in Fig. 32, where a MTDC grid is interconnecting different standard IEEE-test systems, i.e., IEEE-14, -57 and -118 bus systems, operating under different scenarios. A flat start condition is assigned to the state variables in all simulations. The tolerance adopted for the convergence criterion in all simulations is 10^{-6}.

5.6.1 Modified IEEE Two Area RTS-96 test system with two coupled MTDC networks

In order to validate the effectiveness of the aforementioned developed algorithms in complex plane, they are carried out on the Beerten's modified version [52] of the IEEE Two Area RTS-96 (MRTS) network [67] as presented in Fig. 29. In this MRTS network, the three interconnections between the two areas have been replaced by MTDC systems: in the 138 kV system, line 107 - 203 has been replaced by a 3-terminal 150 kV MTDC system connecting the two asynchronous systems with a 150 MW offshore wind farm (buses 301 and 302). In the 345 kV system, lines 113 - 215 and 123 - 217 have been

replaced by a 4-terminal 300 kV MTDC system. The parameters of the VSC converters can be found in Tab. 3. The 3-terminal DC system between buses 107 and 203 represents a filterless MMC VSC MTDC system, the 4-terminal MTDC scheme includes low-pass filters and represents a 2-level PWM VSC MTDC system. Both 3- and 4-terminal MTDC grids are highlighted in red and blue, respectively, in Fig. 29.

Table 3 – VSC Converter Data.

Converter parameters ($p.u.$)		Rating & Converter loss data No.	1,2	3	4,6	5,7
X_t	0.1121	P_{dc} (MW)	100	200	200	100
R_t	0.0015	$\pm V_{dc}$ (kV)	150	150	300	300
X_c	0.16428	a (MW)	1.103	2.206	1.103	2.206
R_c	0.0001	b (kV)	0.887	0.887	1.800	1.800
B_f	0.0087[a]	c_{rec} (Ω)	2.885	1.442	5.94	11.88
		c_{inv} (Ω)	4.371	2.185	9	18

[a] Only included for converters 4 - 7.

The three AC networks operate asynchronously, with reference (slack) buses at 113, 213 and 302. They can be solved either separately or in one row. A generator (U100), producing 80 MW, at bus 107 and a generator (U76), producing 76 MW, at bus 201 have been disabled and replaced by the production of 150 MW in bus 302. The active power injections of the 4-terminal MTDC grid converters closely resemble the line flows between the different zones in the original two-area MRTS network. All converters are set to PQ-constraint control except for converter 2, which is controlling the voltage magnitude at bus 203. Converters 1 and 4 are responsible for controlling the DC Voltage of the two DC grids.

The AC/DC hybrid power flow solution is summarized in Table 4. The same results presented in [52] were achieved by all algorithms developed in the complex plane. Their performance over iterations and time to reach the solution are shown in Table 5. 1. CV-ADS is taken as the benchmark for time comparison. The processing time samples were taken by running each algorithm a thousand times in a row and calculating the median time.

Table 4 – Voltages and power injections report

Converter at		*AC* Side								*DC* Side	
		PCC				**VSC**				Voltage	Power
bus	Control mode	V_s (pu)	θ_s (deg)	P_s (MW)	Q_s $(MVAr)$	V_c (pu)	θ_c (deg)	P_c (MW)	Q_c $(MVAr)$	V_{dc} (pu)	P_{dc} (MW)
107	Slack - Q	1.025	-9.31	66.84	0.00	1.042	0.65	66.91	11.75	1.000	-68.47
203	P - V	1.000	-5.04	75.00	5.86	1.038	6.47	75.09	21.50	0.999	-76.76
301	P - Q	1.050	-0.08	-150.00	0.00	1.120	-20.73	-149.67	56.40	1.006	146.16
113	Slack - Q	1.020	0.00	124.43	0.00	1.061	18.41	124.67	31.36	1.000	-127.49
123	P - Q	1.050	10.13	-50.00	0.00	1.042	2.92	-49.96	-3.46	1.008	48.60
215	P - Q	1.014	10.22	-135.00	0.00	1.062	-9.92	-134.72	39.26	1.010	131.67
217	P - Q	1.039	14.58	50.00	0.00	1.033	21.94	50.04	-3.14	1.006	-51.37

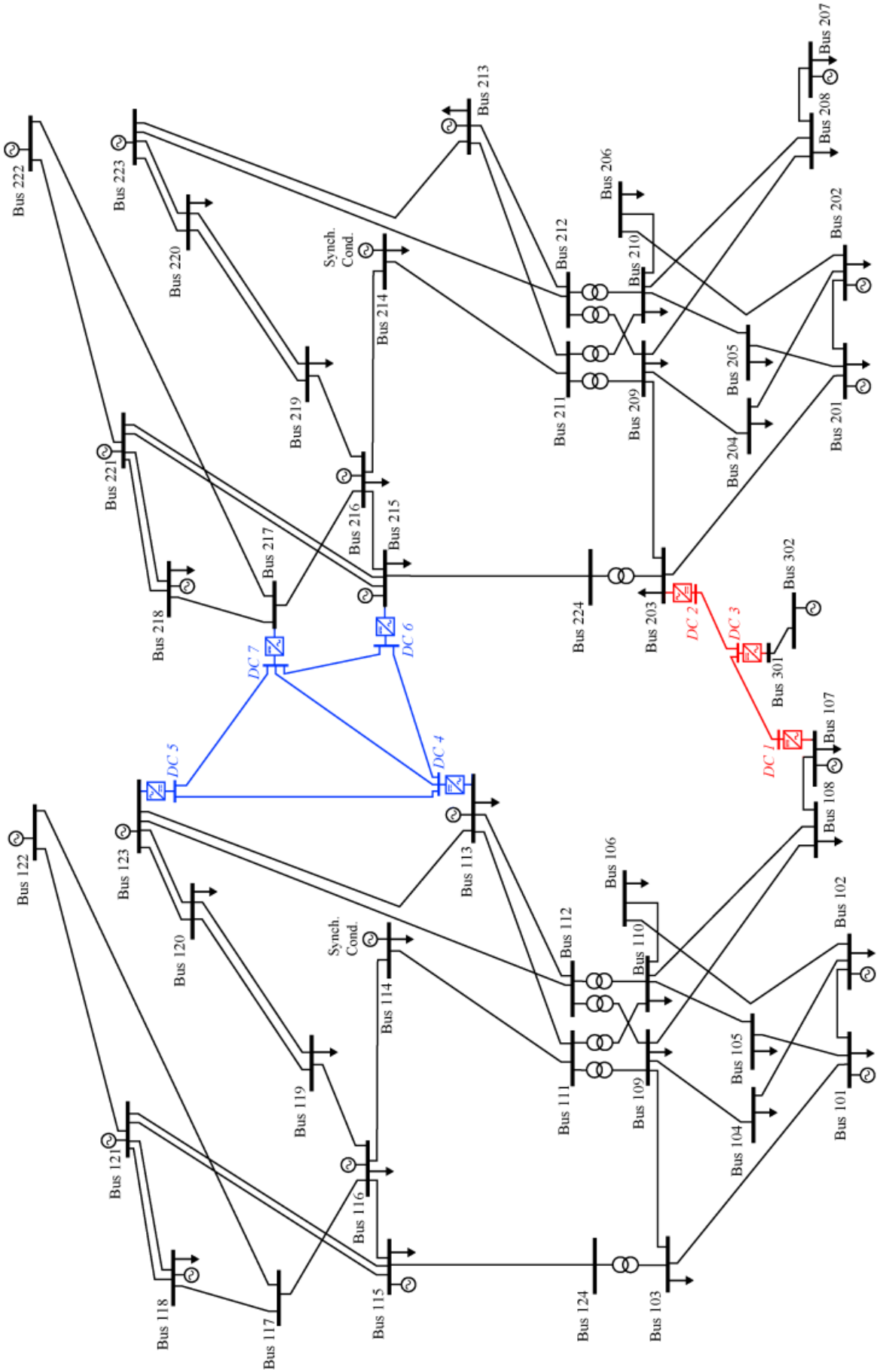

Figure 29 – Modified two-area RTS-96 system with 2 MTDC systems [52].

Table 5 – Comparison between the sequential and unified algorithm 10^{-6}

Algorithm	Number of iterations				Elapsed time	
	AC	DC	Slack DC	Global	per iteration	total
1. CV-ADS	7	5	5	3	4.94 ms	14.85 ms
2. CV-ADS-S	8	6	-	4	3.29 ms (1.50x faster)	13.20 ms (1.12x faster)
3. CV-ADU	-	-	-	5	1.64 ms (3.01x faster)	8.53 ms (1.74x faster)
4. CV-ADU-E	-	-	-	13	0.34 ms (14.49x faster)	5.92 ms (2.51x faster)

By avoiding the need of a third inner iteration, **2. CV-ADS-S** demands an extra outer iteration to converge compared to **1. CV-ADS**, and yet presents a better computing time. Thus, it is shown that the implementation of an extra inner iteration in **1. CV-ADS** can indeed be avoided without any loss of accuracy or efficiency, retaining the aptitude to be incorporated with an external AC power flow software.

Still, the proposed **3. CV-ADU** has a solid advantage in computing time over the sequential methods. Those results are expected, once the unified method synthesizes the whole problem in further less calculations. In a software implementation point of view, for the cases where the AC system must be derived, the unified methodology might be more attractive than the sequential one. This is even more relatable when considering the proposed **3. CV-ADU**, which dismiss the need for constructing the combining AC/DC Jacobian as it is still done in the state-of-art. Furthermore, by being implemented in the complex plane, **3. CV-ADU** can easily be enhanced by the Iwamoto approach, resulting in the proposed **4. CV-ADU-E**, with even further timing performance.

Droop control

With the proposed algorithms validated and their performances compared, a different scenario for the MRTS network is simulated: the VSC converters 1 and 2 at the 3-terminal MTDC grid are now set for DC voltage droop control, both with the V-P droop approach. The first converter is prioritized in the task of controlling the DC voltage by setting it with a higher gain K than the converter 2. In turn, converter 2 has a dead-band which allows the converter having a constant power absorption from the DC grid while its DC voltage is under an interval, i.e., VSC 2 will only contribute to the DC voltage control when the voltage goes off this interval. The converters parameters for this droop control and the DC voltage characteristic are shown in Fig. 30. The active power and DC voltage of reference were obtained from the power flow solution in Table 4.

A series of power flows are solved with this DC voltage control implemented, as the scheduled power provided by the offshore wind farm and rectified by the converter 3 varies from 0 to 300 MW. The steady-state responses of the converter powers are presented in Fig. 31.

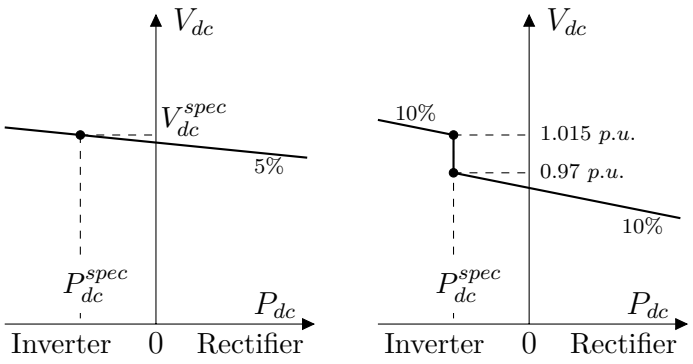

(a) VSC 1 (b) VSC 2

Figure 30 – V-P droop characteristics.

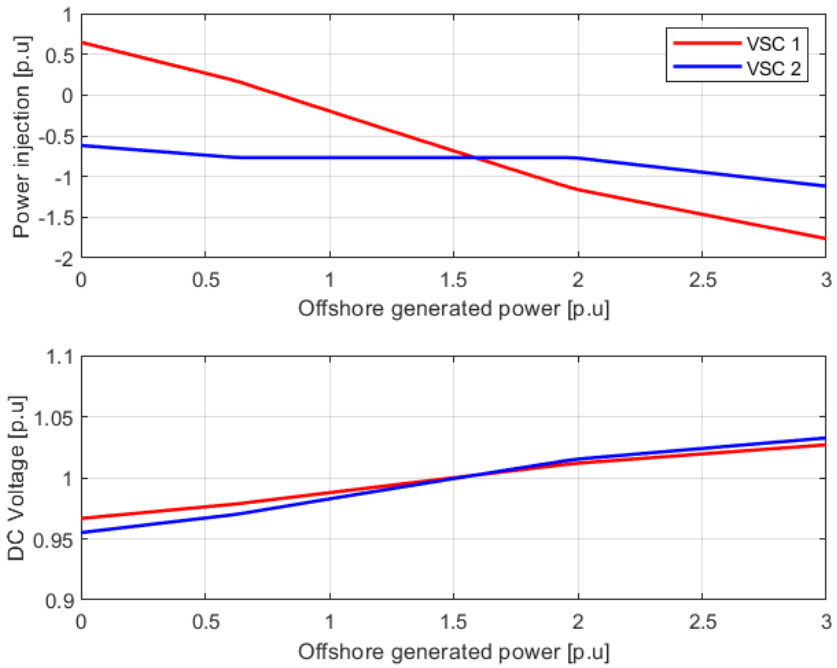

Figure 31 – Steady-state variations of the power injections and DC voltage on VSC 1-2.

5.6.2 IEEE-Standard systems interconnect through MTDC grid

In the sequence are provided the results obtained via simulations carried out on a AC/DC hybrid transmission test system built by interconnecting three well-know IEEE test systems with a 3-bus MTDC, as shown in Fig. 32. considering the converters with the same specifications as the converters 1-3 from Table 3. From the picture below, one can infer that the IEEE-test systems are operated as isolated AC subsystems, but all are interconnected through the DC grid. This latter is operated either in a mono- or bipolar configuration. Thus, it allows us to simulate many scenarios taking AC isolated networks importing or exporting active power to each other. In order to demonstrate the generality of the algorithms developed in complex plane, different scenarios of operation are considered hereafter. Basically, in all simulations a common assumption is considered,

i.e., the IEEE-118 bus system is taken as an export market because of its larger number of power sources. The simulations are conducted as follows:

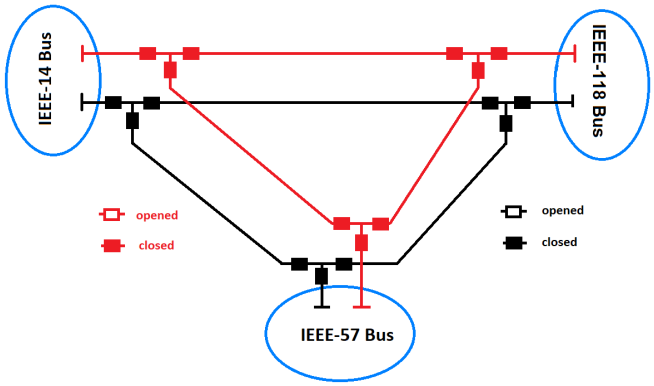

Figure 32 – Hybrid AC&DC one-line diagram.

Case 1: IEEE-118 bus system is exporting energy to the remainder subsystems.

Case 2: The converters coupled to IEEE-14 and -57 bus systems are co-located in the same substation. The power exchanges among all subsystems are the same as considered in Case 1.

Case 3: Likely to Case 1, except that the *DC* link between the IEEE-14 and IEEE-57 subsystems is out of service. Consequently, the DC grid topology becomes radial.

Tables 6 and 7 show the results obtained through the simulations described above. Notice that both DC grid operation mode are equally simulated and included in all cases, i.e., monopolar and bipolar. In all cases, regardless the operation mode, 7 iterations are required to reach the final solution. Moreover, the VSC voltages regarding the subsystems IEEE-14 and -57 bus suffer small changes as can be seen in Table 6 in all cases as well.

On the other hand, Table 7 presents the power flow values at each branch in the *DC* grid. Remark that the losses variation are approximately linear concerning the operation mode of the converters. The total losses under bipolar operation mode is approximately the half of those resulted under monopolar operation mode. Highlight as expected there are no losses in the link which connects the subsystems IEEE-14 and -57 bus in Case 2 once the converters referred to those subsystems are co-located in the same substation. Finally, in Case 3 the total losses have decreased because the link which connects the subsystems IEEE-14 and -57 bus is out of service.

Table 6 – Voltages and power injections report.

	Converter at				*AC* Side						*DC* Side	
					VSC		Power Injection		Modulation index		Voltage	Power
Cases	Operation Mode	System	bus (type)	Control mode	V_{sh}	θ_{sh}	P_{sh}	Q_{sh}	m	φ_{sh}	V_{dc}	P_{dc}
					(pu)	(deg)	(MW)	$(MVAr)$	(pu)	(deg)	(pu)	(MW)
Case 1	Monopolar	118-bus	59 (PV)	P - Q	0.969	-12.318	-60.00	-40.00	1.110	-12.318	1.008	-58.59
		57-bus	18 (PQ)	Slack - V	1.006	-11.239	20.70	11.41	1.161	-11.239	1.000	21.86
		14-bus	5 (PQ)	P - Q	1.021	-3.632	35.00	5.00	1.182	-3.632	0.998	36.19
	Bipolar	118-bus	59 (PV)	P - Q	0.969	-12.318	-60.00	-40.00	1.114	-12.318	1.004	-58.59
		57-bus	18 (PQ)	Slack - V	1.006	-11.188	20.97	11.44	1.161	-11.188	1.000	22.13
		14-bus	5 (PQ)	P - Q	1.021	-3.632	35.00	5.00	1.181	-3.632	0.999	36.19
Case 2	Monopolar	118-bus	59 (PV)	P - Q	0.969	-12.318	-60.00	-40.00	1.109	-12.318	1.009	-58.59
		57-bus	18 (PQ)	Slack - V	1.006	-11.235	20.72	11.41	1.161	-11.235	1.000	21.86
		14-bus	5 (PQ)	P - Q	1.021	-3.632	35.00	5.00	1.180	-3.632	1.000	36.19
	Bipolar	118-bus	59 (PV)	P - Q	0.969	-12.318	-60.00	-40.00	1.114	-12.318	1.004	-58.59
		57-bus	18 (PQ)	Slack - V	1.006	-11.186	20.98	11.45	1.161	-11.186	1.000	22.14
		14-bus	5 (PQ)	P - Q	1.021	-3.632	35.00	5.00	1.180	-3.632	1.000	36.19
Case 3	Monopolar	118-bus	59 (PV)	P - Q	0.969	-12.318	-60.00	-40.00	1.112	-12.318	1.006	-58.59
		57-bus	18 (PQ)	Slack - V	1.006	-11.252	20.63	11.40	1.161	-11.252	1.000	21.79
		14-bus	5 (PQ)	P - Q	1.021	-3.632	35.00	5.00	1.188	-3.632	0.993	36.19
	Bipolar	118-bus	59 (PV)	P - Q	0.969	-12.318	-60.00	-40.00	1.115	-12.318	1.003	-58.59
		57-bus	18 (PQ)	Slack - V	1.006	-11.194	20.93	11.44	1.161	-11.194	1.000	22.10
		14-bus	5 (PQ)	P - Q	1.021	-3.632	35.00	5.00	1.184	-3.632	0.996	36.19

Table 7 – Power flow report: *DC* side.

Cases	Operation Mode	Branch	Direct Flow P_{dc} (MW)	Reverse Flow P_{dc} (MW)	Power Loss P_{dc} (MW)
Case 1	Monopolar	59 - 18	30.62	-30.38	0.24
		59 - 5	27.98	-27.70	0.28
		18 - 5	8.51	-8.49	0.02
		Total Power Loss			0.54
	Bipolar	59 - 18	30.67	-30.55	0.12
		59 - 5	27.93	-27.79	0.14
		18 - 5	8.41	-8.40	0.01
		Total Power Loss			0.27
Case 2	Monopolar	59 - 18	33.84	-33.55	0.29
		59 - 5	24.75	-24.53	0.22
		18 - 5	11.66	-11.66	0.00
		Total Power Loss			0.51
	Bipolar	59 - 18	33.84	-33.69	0.15
		59 - 5	24.75	-24.64	0.11
		18 - 5	11.55	-11.55	0.00
		Total Power Loss			0.26
Case 3	Monopolar	59 - 18	21.92	-21.79	0.13
		59 - 5	36.67	-36.19	0.48
		Total Power Loss			0.61
	Bipolar	59 - 18	22.16	-22.10	0.06
		59 - 5	36.43	-36.19	0.24
		Total Power Loss			0.30

5.7 Partial Conclusions

This chapter develops Newton-Raphson power flow algorithms in the complex plane aiming to evaluate the performance of VSC-MTDC hybrid AC/DC transmission grids, in both sequential and unified fashion. In addition, a unified exact power flow based on the Iwamoto's approach is proposed. It is shown that the implementation in the complex plane is straightforward and is much easier to encode than in the former domain. Moreover, all of the computations in the complex plane can be carried out in a very similar manner, making many tools and methods already developed readily available to be used in the industry.

6 Conclusions and Future Work

6.1 Conclusions

This thesis is a contribution on the study of complex-valued formulations for steady-state analysis for power systems, in particular hybrid AC/DC power systems with multi-terminal VSC-HVDC grid. Wirtinger calculus and compact expressions of complex variable vector derivatives are the basis of the presented proposals. The underlying mathematical formulation is elegant and leads to a computer code that can be easily implemented and maintained.

In Chapter 3, the generic Newton-Raphson power flow algorithm formulation in the complex plane was presented, which was the base for the proposed algorithms in the subsequent chapters. It was shown how the Wirtinger Calculus can be used for deriving the power flow equations in their natural complex form, dismissing the need for splitting those equations in the Real Domain.

In Chapter 4, the Iwamoto's approach for expanding the quadratic real-valued power flow equations in rectangular coordinates was applied for the complex-valued formulation, once it is also formulated with quadratic equations. This resulted in a faster power flow algorithm based on an exact correction vector iteration, which does not require updating and re-factorizing the Jacobian matrix.

The context presented in Chapter 2 was the motivation for directing the research focus in CV steady-state analysis to hybrid AC/DC power systems, which resulted in contributions presented in Chapter 5.

In Chapter 5 the complex-valued generalized VSC-MTDC model was presented, with no restrictions on DC grid topology or VSC technology. The sequential algorithm proposed by Beerten was reformulated in the Complex Domain, resulting in simpler formulations due to the nature of the complex-value power flow equations without any loss of accuracy. It was also shown that the sequential method could be simplified by avoiding the inner iteration loop for VSC power losses balancing. A unified method was proposed in a fashion where the Jacobian matrix is built by considering the AC and DC grids decoupled, resulting in an easy and very concise implementation. Furthermore, the Iwamoto approach could also be used to reformulate the proposed unified algorithm by doing simple adjustments in the framework, resulting in a faster algorithm.

6.2 Future Work

An immediate goal to be investigated is the building of an enhanced power flow aiming VSC-MTDC hybrid AC/DC transmission grids that include a variety of FACTS devices and renewable energy sources. For instance, the unified power flow controller (UPFC) which controls the real and imaginary parts of the total complex power over a transmission line, i.e., active and reactive power, simultaneously; a battery energy storage system (BESS); a PMSG-based wind farm and a photovoltaic generation system (PV), to cite a few.

The studied second-order power flow, or exact power flow, has reported very good results for well-conditioned AC or AC/DC systems, however, its performance in ill-conditioned cases has not been explored yet. This line should lead to developing universal solvers, able to outperform NR in well-conditioned systems and successfully solve ill-conditioned cases.

The studied techniques should be considered for other related tools like the Continuation Power Flow, Optimal Power Flow, and Security Analysis, for instance. Additionally, the use of complex variables is ideally suited for handling the phasor measurements straightforwardly, being promising for state estimation frameworks and Energy Management System (EMS) applications.

6.3 Publications

Published

1. Pires, R.; Chagas, G.; Mili, L. - Robust complex-valued Levenberg-Marquardt algorithm as applied to power flow analysis, *International Journal of Electrical Power and Energy Systems*, v.113, December 2019.

2. Pires, R.; Chagas, G. - Enhanced power flow solution in complex plane, *International Journal of Electrical Power and Energy Systems*, v.135, September 2021.

In review

3. Chagas, G.; Pires, R.; Mili, L. - The Sequential Power Flow in Complex Plane for Solving the VSC-MTDC Hybrid AC/DC Transmission Grids, submitted to *International Journal of Electrical Power and Energy Systems*, 2022.

In prep

4. Chagas, G.; Pires, R. - The Unified AC/DC VSC-MTDC Second-order Power Flow in Complex Plane.

Appendix

APPENDIX A – Complex-Valued Functions and Variables

A.1 The Complex-Valued Wirtinger Calculus

This appendix contains some of the definitions and properties of complex-valued functions, its differentiability, and the Wirtinger Calculus as summarized in Professor Pires work (2018) - [5].

A.2 Complex Differentiability

A complex function is defined as

$$f(x) = u(a,b) + j\ v(a,b), \tag{A.1}$$

where $x = a + j\ b$ and $u(a,b)$, $v(a,b)$ are real functions, $u,\ v : \mathbb{R}^2 \to \mathbb{R}$. Functions like (A.1) are in general complex, but may be real-valued in special cases, e.g.: squared error cost function $\mathscr{J}(|\mathbf{e}^2|)$. The definition of complex differentiability requires that the derivatives defined as the limit be independent of the direction in which Δx approaches 0 in complex plane.

$$f'(x_0) = \lim_{\Delta x \to 0} \frac{f(x + \Delta x) - f(x)}{\Delta x}. \tag{A.2}$$

This requires that the Cauchy-Riemann equations be satisfied, i.e.,

$$\frac{\partial u}{\partial a} = \frac{\partial v}{\partial b}, \qquad \frac{\partial v}{\partial a} = -\frac{\partial u}{\partial b}. \tag{A.3}$$

These conditions are necessary for $f(x)$ to be complex-differentiable. If the partial derivatives of $u(a,b)$ and $v(a,b)$ are continuous on their entire domain, then they are sufficient as well. Therefore, the complex function $f(x)$ is called an analytic or holomorphic function [68]. As an example, let $f(x) = x^2$ be a complex function with $x = a + j\ b$. Then,

$$f(x) = x^2 = \underbrace{a^2 - b^2}_{=u} + j\ \underbrace{2ab}_{=v} = y,$$

which under differentiation rule leads to

$$\tfrac{\partial u}{\partial a} = 2a = \tfrac{\partial v}{\partial b} = 2a; \qquad \tfrac{\partial u}{\partial b} = -2b = -\left(\tfrac{\partial v}{\partial a} = 2b\right).$$

These results show that the Cauchy-Riemann equations hold and hence $f(x) = y = x^2$ is a holomorphic function.

A.3 *CR-Calculus* or Wirtinger Calculus

Introduced by Wilhelm Wirtinger in 1927 [2], the *CR-Calculus*, also known as the Wirtinger calculus, provides a way to differentiate non-analytic functions of complex variables. Specifically, this calculus is applicable to a function $f(x)$ given by (A.1) *if and only if* $u(a,b)$ and $v(a,b)$ have continuous partial derivatives with respect to a and b, yielding:

$$\frac{\partial f}{\partial x} = \frac{\partial f}{\partial a}\frac{\partial a}{\partial x} + \frac{\partial f}{\partial b}\frac{\partial b}{\partial x}. \tag{A.4}$$

Considering that:

$$a = \frac{(x + x^*)}{2}, \qquad \partial a = \frac{(\partial x + \partial x^*)}{2}, \tag{A.5}$$

$$b = j\,\frac{(x^* - x)}{2}, \qquad \partial b = j\,\frac{(\partial x^* - \partial x)}{2}, \tag{A.6}$$

and by setting $\frac{\partial x^*}{\partial x}$ to zero, it follows that:

$$\frac{\partial f}{\partial x} = \frac{1}{2}\left(\frac{\partial f}{\partial a} - j\,\frac{\partial f}{\partial b}\right). \tag{A.7}$$

Note that the Cauchy-Riemann conditions for $f(\cdot)$ to be analytic in x can be expressed compactly using the gradient as $\frac{\partial f}{\partial x^*} = 0$, i.e., $f(\cdot)$ is a function of only x.

Similarly, if the derivative of $f(\cdot)$ is taken with respect to x^*, i.e.,

$$\frac{\partial f}{\partial x^*} = \frac{\partial f}{\partial a}\frac{\partial a}{\partial x^*} + \frac{\partial f}{\partial b}\frac{\partial b}{\partial x^*}, \tag{A.8}$$

by setting $\frac{\partial x}{\partial x^*}$ to zero, it becomes:

$$\frac{\partial f}{\partial x^*} = \frac{1}{2}\left(\frac{\partial f}{\partial a} + j\,\frac{\partial f}{\partial b}\right). \tag{A.9}$$

Again, the Cauchy-Riemann conditions for $f(\cdot)$ to be analytic in x^* can be expressed compactly using the gradient as $\frac{\partial f}{\partial x} = 0$, i.e., $f(\cdot)$ is a function only of x^*.

In other words, the gradient (respectively conjugate gradient) operator acts as a partial derivative with respect to x (respectively to x^*), treating x^* (respectively x) as a constant. This is formally given by:

$$\frac{\partial f(x_c)}{\partial x} = \frac{\partial f(x,x^*)}{\partial x}\Big|_{x^*=Const} = \frac{1}{2}\left(\frac{\partial f}{\partial a} - j\,\frac{\partial f}{\partial b}\right), \tag{A.10}$$

$$\frac{\partial f(x_c)}{\partial x^*} = \frac{\partial f(x,x^*)}{\partial x^*}\Big|_{x=Const} = \frac{1}{2}\left(\frac{\partial f}{\partial a} + j\,\frac{\partial f}{\partial b}\right). \tag{A.11}$$

As an example, let $f(x_c) = f(x,x^*) = x^*\,x = \|x\|^2 = a^2 + b^2$, be a real function of complex variable which is the squared Euclidean distance to the origin, with $x = a + j\,b$. Then,

$$f(x_c) = f(x, x^*) = x^* x = \underbrace{a^2 + b^2}_{=u} + j \underbrace{(ab - ab)}_{0=v} = y$$

as $v = 0$, clearly the Cauchy-Riemann equations do not hold and hence $f(x_c) = f(x, x^*) = x^* x$ is not analytic or non-holomorphic function. To overcome this apparent difficult, by applying the *CR-Calculus* leads to

$$\frac{\partial f(x_c)}{\partial x} = x^*; \qquad \frac{\partial f(x_c)}{\partial x^*} = x,$$

which suggests the geometric interpretation showed in Fig. 33.

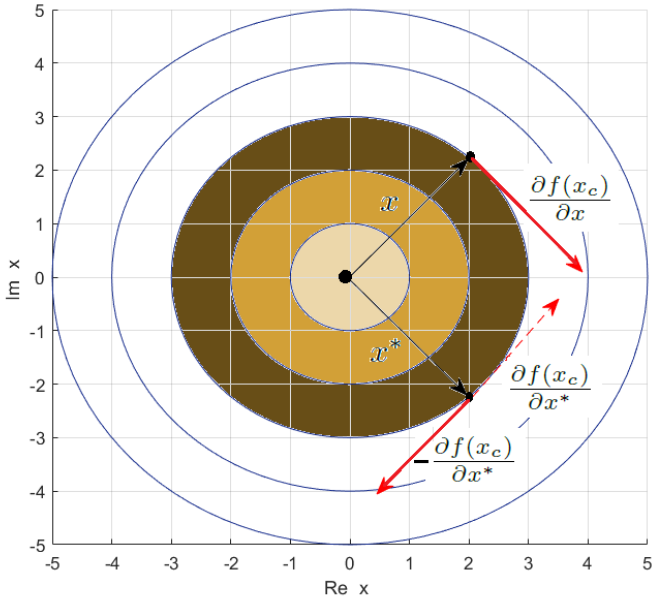

Figure 33 – Contour plot of the real function of complex variable.

Its analysis allow us to infer that the direction of maximum rate of change of the objective function is given by the conjugate gradient defined in (A.11). Notice that its positive direction is referred to a maximization problem (dot arrow) whereas the opposite direction concerns to the cost function minimization.

APPENDIX B – Numerical Equivalence $f(\Delta\underline{\mathbf{x}}_e) \equiv \frac{1}{2}\, H(\underline{\mathbf{x}}_e)\, \Delta\underline{\mathbf{x}}_e^2$

Let us consider the following simple system of quadratic equations and the starting values assigned to the unknowns as being $\underline{\mathbf{x}}_e^{(\nu=0)} = [1.0; 1.0]$:

$$\begin{aligned} f_1(x) &= +2x_1^2 - 2x_1x_2 + 2x_2^2 - 2.24 \\ f_2(x) &= -2x_1^2 - 1x_1x_2 + 2x_2^2 - 0.64, \end{aligned} \tag{B.1}$$

which in matrix form becomes

$$\begin{aligned} \begin{bmatrix} \\ y_s \\ \\ \end{bmatrix} &= \begin{bmatrix} 2 & -1 & -1 & 2 \\ & & & \\ -2 & -0.5 & -0.5 & 2 \end{bmatrix} \cdot \begin{bmatrix} x_1x_1 \\ x_1x_2 \\ x_2x_1 \\ x_2x_2 \end{bmatrix} \\ &= \begin{bmatrix} 2 & -2 & 2 \\ & & \\ -2 & -1 & 2 \end{bmatrix} \cdot \begin{bmatrix} x_1x_1 \\ x_1x_2 \\ x_2x_2 \end{bmatrix} \end{aligned} \tag{B.2}$$

where $y_s = [2.24; 0.64]^T$. Hence, the Taylor series expansion of (B.2) leads to

$$\begin{aligned} \begin{bmatrix} \\ y_s \\ \\ \end{bmatrix} = \begin{bmatrix} \\ y(x_e) \\ \\ \end{bmatrix} + \begin{bmatrix} \frac{\partial y_1}{\partial x_1} & \frac{\partial y_1}{\partial x_2} \\ & \\ \frac{\partial y_2}{\partial x_1} & \frac{\partial y_2}{\partial x_2} \end{bmatrix} \cdot \begin{bmatrix} \Delta x_1 \\ \\ \Delta x_2 \end{bmatrix} + \\ + \frac{1}{2} \begin{bmatrix} \frac{\partial^2 y_1}{\partial x_1^2} & 2\,\frac{\partial^2 y_1}{\partial x_1 \partial x_2} & \frac{\partial^2 y_1}{\partial x_2^2} \\ & & \\ \frac{\partial^2 y_2}{\partial x_1^2} & 2\,\frac{\partial^2 y_2}{\partial x_1 \partial x_2} & \frac{\partial^2 y_2}{\partial x_2^2} \end{bmatrix} \cdot \begin{bmatrix} \Delta x_1^2 \\ \Delta x_1 \Delta x_2 \\ \Delta x_2^2 \end{bmatrix}, \end{aligned} \tag{B.3}$$

or

$$\begin{bmatrix} 2.24 \\ \\ 0.64 \end{bmatrix} = \begin{bmatrix} f_1(x_e^{(\nu)}) \\ \\ f_2(x_e^{(\nu)}) \end{bmatrix} + \begin{bmatrix} 4\ x_{e_1}^{(\nu)} - 2\ x_{e_2}^{(\nu)} & -2\ x_{e_1}^{(\nu)} + 4\ x_{e_2}^{(\nu)} \\ \\ -4\ x_{e_1}^{(\nu)} - x_{e_2}^{(\nu)} & -x_{e_1}^{(\nu)} + 4\ x_{e_2}^{(\nu)} \end{bmatrix} \begin{bmatrix} \Delta x_1^{(\nu)} \\ \\ \Delta x_2^{(\nu)} \end{bmatrix} + \frac{1}{2} \begin{bmatrix} 4 & 2\ (-2) & 4 \\ \\ -4 & 2\ (-1) & 4 \end{bmatrix} \begin{bmatrix} \Delta x_1^{2(\nu)} \\ \Delta x_1^{(\nu)} \Delta x_2^{(\nu)} \\ \Delta x_2^{2(\nu)} \end{bmatrix}, \tag{B.4}$$

and alternatively,

$$\begin{bmatrix} 2.24 \\ \\ 0.64 \end{bmatrix} = \begin{bmatrix} f_1(x_e^{(\nu)}) \\ \\ f_2(x_e^{(\nu)}) \end{bmatrix} + \begin{bmatrix} 4\ x_{e_1}^{(\nu)} - 2\ x_{e_2}^{(\nu)} & -2\ x_{e_1}^{(\nu)} + 4\ x_{e_2}^{(\nu)} \\ \\ -4\ x_{e_1}^{(\nu)} - x_{e_2}^{(\nu)} & -x_{e_1}^{(\nu)} + 4\ x_{e_2}^{(\nu)} \end{bmatrix} \begin{bmatrix} \Delta x_1{}^{(\nu)} \\ \\ \Delta x_2{}^{(\nu)} \end{bmatrix} + \begin{bmatrix} f_1(\Delta x_1^{(\nu)}) \\ \\ f_2(\Delta x_2^{(\nu)}) \end{bmatrix}, \tag{B.5}$$

where the 2nd order term in (B.4) is replaced by the 1st order term in (B.5) except that now its arguments are the corrections imposed to the unknowns. Thus, (B.5) in the first iteration becomes

$$\begin{bmatrix} 2.24 \\ \\ 0.64 \end{bmatrix} = \begin{bmatrix} 2 \\ \\ -1 \end{bmatrix} + \begin{bmatrix} 2 & 2 \\ \\ -5 & 3 \end{bmatrix} \cdot \begin{bmatrix} \Delta x_1 \\ \\ \Delta x_2 \end{bmatrix}, \tag{B.6}$$

which can be re-written and solved, yielding

$$\begin{bmatrix} \Delta x_1 \\ \\ \Delta x_2 \end{bmatrix} = -\begin{bmatrix} 2 & 2 \\ \\ -5 & 3 \end{bmatrix}^{-1} \cdot \begin{bmatrix} -0.24 \\ \\ -1.64 \end{bmatrix} = \begin{bmatrix} -0.16 \\ \\ 0.28 \end{bmatrix}. \tag{B.7}$$

Now, it allow us to infer about the equivalence between the 2nd order term in (B.4) and the third term in (B.5), yielding

$$\frac{1}{2}\begin{bmatrix} 4 & -4 & 4 \\ \\ -4 & -2 & 4 \end{bmatrix} \cdot \begin{bmatrix} (-0.16)^2 \\ (-0.16)(0.28) \\ (0.28)^2 \end{bmatrix} = \begin{bmatrix} 0.2976 \\ \\ 0.1504 \end{bmatrix}$$

$$\equiv \quad \begin{bmatrix} f_1(-0.16) \\ \\ f_2(0.28) \end{bmatrix} = \begin{bmatrix} 0.2976 \\ \\ 0.1504 \end{bmatrix}. \tag{B.8}$$

This nice property holds at each iteration. Therefore, taking in mind larger systems, the use of equation (B.5) instead (B.4) is computationally much more advantageous.

Annex

Electrical Power and Energy Systems 113 (2019) 383–392

Contents lists available at ScienceDirect

Electrical Power and Energy Systems

journal homepage: www.elsevier.com/locate/ijepes

Robust complex-valued Levenberg-Marquardt algorithm as applied to power flow analysis

Robson Pires[a,*], Lamine Mili[b], Guilherme Chagas[a]

[a] Institute of Electric Systems and Energy, Federal University of Itajubá, Minas Gerais, MG 37500-903, Brazil
[b] Bradley Department of Electrical and Computer Engineering, Virginia Polytechnic Institute and State University, VA 22043, USA

ARTICLE INFO

Keywords:
Complex-valued power flow analysis
Newton-Raphson and Levenberg-Marquardt algorithms
Conjugate rectangular coordinates system
Bi-quadratic convergence property

ABSTRACT

This paper deals with a robust complex-valued Levenberg-Marquardt algorithm specially developed for solving ill-conditioned power flow problems. Moreover, it can also be a useful tool for voltage instability and voltage collapse studies. Because power flow models are nonlinear, the Wirtinger calculus is applied to develop iterative algorithms based on Taylor series expansions of nonlinear functions of complex variables and their complex conjugates. Our proposal in complex plane is straightforward derived in rectangular coordinates. Consequently, its performance is compared to the well-known optimized multiplier based load flow method. Aiming this purpose, we show that few changes in the codes are required to transform the complex-valued Newton-Raphson power flow algorithm into the complex-valued Levenberg-Marquardt power flow one. Furthermore, we show that the latter lends itself well to modeling new smart grid technologies while exhibiting a bi-quadratic convergence rate and superior performance as compared to the former procedure. The performance of our proposal is demonstrated and analyzed on well-conditioned IEEE-14, −30, −57 and −118 bus systems and the Brazilian Southern-equivalent system termed SIN-1916 bus. Furthermore, its performance is also demonstrated on the ill-conditioned IEEE-11, −43 bus systems besides the SIN-1916 under stressed operating conditions or higher R/X ratios of transmission lines.

1. Introduction

Traditionally, algorithms for solving various power system applications are developed in the real domain. Examples are power flow analysis and power system state estimation, among others. Evidently, real-valued models are not natural representations of complex-valued voltage and current phasors; they lead to solution methods that may suffer from large computing times and ill-conditioned problems. To circumvent these weaknesses, iterative and non-iterative algorithms carried out in the complex plane were recently proposed in the literature; examples are [1–4] for iterative methods and [5–7] for non-iterative methods. Iterative complex-valued power flow calculation is addressed by Wang [5] and by Nguyen and Vu [1] by using the Wirtinger calculus [8]. Besides in power flow analysis, *CR* calculus was also extended to power system state estimation [9,10]. Additionally, complex-valued optimization has also found applications in applied mathematics, signal processing [11–15], control theory, neural networks [16] and biomedicine, among others. The Wirtinger calculus makes use of the property that if a function is analytic in the space spanned by $\Re\{x\}$ and $\Im\{x\}$ in the $\mathbb{R} - domain$, it is also analytic in the space spanned by x and x^* in the $\mathbb{C} - domain$. The latter is known as the conjugate coordinates system and it is also referred as $CR - Calculus$.

In the state-of-the-art literature of numerical analysis, a number of methods have been proposed to solve ill-conditioned nonlinear system of equations; the reader is referred to [17–19] for further details. In power systems analysis, [20–23] were advocating the use of the Brown's and Brent's methods while recently, Pourbagher and Derakhshandeh [24] were promoting the Levenberg-Marquardt algorithm as described in [25]. We carry out a thorough comparison between various methods described in [25–27] on test functions posed in [17]. Our study reveals that the algorithm proposed by Yang [25] exhibits the best trade-off between easy encoding task, low computational overhead and very good robustness. Thus, this algorithm is chosen as the algorithm to solve the problem posed in complex-valued power flow analysis. Enhancements to the Yang's proposal can be found in [27,28], but they are beyond the scope of this work. Nonetheless, as our goal is to improve the numerical robustness of the Newton-Raphson power flow algorithm, the Barel's format equation [14] is used in this work because it is based on the Jacobian instead of the gain matrix [25], which

* Corresponding author.
E-mail address: rpires@unifei.edu.br (R. Pires).

https://doi.org/10.1016/j.ijepes.2019.05.032
Received 19 November 2018; Received in revised form 14 April 2019; Accepted 12 May 2019
Available online 29 May 2019

Nomenclature

$\underline{x}_c$	vector of the state variables in the conjugate coordinate system
x, x^*	complex and complex conjugate state variables
a, a^*	complex and complex conjugate tap position
$\Re\{\cdot\}$, $\Im\{\cdot\}$	real and imaginary part of a complex variable
$\mathbf{J}$	complex-valued Jacobian matrix
$\underline{M}$	complex-valued mismatch vector
$(\cdot)_c$	quantity in the conjugate coordinate system
$\|\cdot\|^2$	squared Euclidean norm
$\|\cdot\|_\infty$	infinity norm
$cond(\cdot)$	matrix condition number
$\eta > 0$	the Levenberg-Marquardt (LM) regularization parameter
ν	iteration counter

mainly aimed to speed up the search of a solution. Notice that we have successfully applied the Levenberg-Marquardt algorithm and compared its performance to others classical methods widely known in power system state estimation [29].

The complex-valued Newton-Raphson and Levenberg-Marquardt power flow algorithms, respectively termed (CV-NR) and (CV-LM) for short, were developed by using Wirtinger calculus. When compared to the former, the latter involves Jacobian matrices with enhanced sparsity property; is naturally formulated in the rectangular coordinates and the mismatch vector can be built based on quadratic functions. Consequently, the iterative solution emerged from the Taylor series expansion allow us to retain the exact non-linearity of the power flow equations. Notice that the 2nd-order term is based on the Iwamoto's contribution [30] instead of the classical Hessian matrix because it implies less computational overhead; possesses higher numerical robustness when the power system is heavily loaded or presents branches with high R/X ratio [20–24,29–32], and exhibits a bi-quadratic convergence rate [25,27], which is clearly superior to the quadratic convergence rate of the Newton-Raphson algorithm. Many others contributions on the issues raised above are stated in [33–36], to cite a few. In order to conduct a comparative analysis a family of algorithms as applied to power flow analysis is used for evaluating the performance of our proposal and each one is identified as follows:

(1) $RV-NR^{(p,r)}$: Real-Valued Newton-Raphson algorithms in polar and rectangular coordinates are the conventional methods used today by the industry.
(2) $RV-LM^{(p,r)}$: Real-Valued Levenberg-Marquadt in real-domain, e.g., polar and rectangular coordinates. The algorithm is the counterpart of our proposal in complex plane [25] in both coordinates.
(3) $RV-OM^{(r)}$: Real-Valued Optimized Multiplier method in rectangular coordinates as developed by Tamura & Iwamoto [30] is a robust algorithm dealing with ill-conditioned power flow problems [34,35]. This application is taken as a benchmark in the simulations presented and discussed in this paper.
(4) $CV-OM^{(r)}$: Complex-Valued Optimized Multiplier method in rectangular coordinates. It is the counterpart of the benchmark application taken in complex plane.
(5) $CV-NR^{(r)}$: Complex-Valued Newton-Raphson algorithm in rectangular coordinates which has been proposed in [1].
(6) $CV-LM^{(r)}$: Complex-Valued Levenberg-Marquadt method in rectangular coordinates is our proposal described in the sequel.

This paper is organized as follows. The theoretical foundation of the proposal is based on the Wirtinger Calculus as presented in Section 2. In Section 3 is derived the bus models as applied to power flow analysis. Section 4 shows the derivation of the robust complex-valued Levenberg-Marquardt algorithm which is emerged in an unified complex conjugate coordinates system, including its Jacobian matrix. Section 5 presents a small example followed by the simulations carried out on well- and ill-conditioned IEEE-test systems. The Section 6 states some conclusions and future works.

2. Theoretical foundation

2.1. Complex differentiability

A complex function is defined as

$$f(x) = u(a, b) + jv(a, b), \tag{1}$$

where $x = a + jb$ and $u(a, b)$, $v(a, b)$ are real functions, $u, v : \mathbb{R}^2 \to \mathbb{R}$. Functions like (1) are in general complex, but may be real-valued in special cases, e.g.: squared error cost function $\mathscr{J}(|\mathbf{e}^2|)$. The definition of complex differentiability requires that the derivatives defined as the limit be independent of the direction in which Δx approaches 0 in complex plane.

$$f'(x_0) = \lim_{\Delta x \to 0} \frac{f(x + \Delta x) - f(x)}{\Delta x}. \tag{2}$$

This requires that the Cauchy-Riemann equations be satisfied, i.e.,

$$\frac{\partial u}{\partial a} = \frac{\partial v}{\partial b}, \qquad \frac{\partial v}{\partial a} = -\frac{\partial u}{\partial b}. \tag{3}$$

These conditions are necessary for $f(x)$ to be complex-differentiable. If the partial derivatives of $u(a, b)$ and $v(a, b)$ are continuous on their entire domain, then they are sufficient as well. Therefore, the complex function $f(x)$ is called an analytic or holomorphic function [37]. As an example, let $f(x) = x^2$ be a complex function with $x = a + jb$. Then,

$$f(x) = x^2 = \underbrace{a^2 - b^2}_{=u} + j\underbrace{2ab}_{=v} = y,$$

which under differentiation rule leads to

$$\frac{\partial u}{\partial a} = 2a = \frac{\partial v}{\partial b} = 2a; \qquad \frac{\partial u}{\partial b} = -2b = -\left(\frac{\partial v}{\partial a} = 2b\right).$$

These results show that the Cauchy-Riemann equations hold and hence $f(x) = y = x^2$ is a holomorphic function.

2.2. CR-Calculus or Wirtinger calculus

Introduced by Wilhelm Wirtinger in 1927 [8], the *CR-Calculus*, also known as the Wirtinger calculus, provides a way to differentiate non-analytic functions of complex variables. Specifically, this calculus is applicable to a function $f(x)$ given by (1) if $u(a, b)$ and $v(a, b)$ have continuous partial derivatives with respect to a and b, yielding

$$\frac{\partial f}{\partial x} = \frac{\partial f}{\partial a}\frac{\partial a}{\partial x} + \frac{\partial f}{\partial b}\frac{\partial b}{\partial x}. \tag{4}$$

Since we have

$$a = \frac{(x + x^*)}{2}, \; \partial a = \frac{(\partial x + \partial x^*)}{2}, \tag{5}$$

$$b = j\frac{(x^* - x)}{2}, \; \partial b = j\frac{(\partial x^* - \partial x)}{2}, \tag{6}$$

and by setting $\frac{\partial x^*}{\partial x}$ to zero, it follows that

$$\frac{\partial f}{\partial x} = \frac{1}{2}\left(\frac{\partial f}{\partial a} - j\frac{\partial f}{\partial b}\right). \tag{7}$$

Note that the Cauchy-Riemann conditions for $f(\cdot)$ to be analytic in x can be expressed compactly using the gradient as $\frac{\partial f}{\partial x^*} = 0$, i.e., $f(\cdot)$ is a function of only x.

Similarly, if we take the derivative of $f(\cdot)$ with respect to x^*, that is,

$$\frac{\partial f}{\partial x^*} = \frac{\partial f}{\partial a}\frac{\partial a}{\partial x^*} + \frac{\partial f}{\partial b}\frac{\partial b}{\partial x^*}. \tag{8}$$

By setting $\frac{\partial x}{\partial x^*}$ to zero, we get

$$\frac{\partial f}{\partial x^*} = \frac{1}{2}\left(\frac{\partial f}{\partial a} + j\frac{\partial f}{\partial b}\right). \tag{9}$$

Again, the Cauchy-Riemann conditions for $f(\cdot)$ to be analytic in x^* can be expressed compactly using the gradient as $\frac{\partial f}{\partial x} = 0$, i.e., $f(\cdot)$ is a function only of x^*.

In other words, the gradient (respectively conjugate gradient) operator acts as a partial derivative with respect to x (respectively to x^*), treating x^* (respectively x) as a constant. Formally, we have

$$\frac{\partial f(x_c)}{\partial x} = \frac{\partial f(x, x^*)}{\partial x}\bigg|_{x^*=Const} = \frac{1}{2}\left(\frac{\partial f}{\partial a} - j\frac{\partial f}{\partial b}\right), \tag{10}$$

$$\frac{\partial f(x_c)}{\partial x^*} = \frac{\partial f(x, x^*)}{\partial x^*}\bigg|_{x=Const} = \frac{1}{2}\left(\frac{\partial f}{\partial a} + j\frac{\partial f}{\partial b}\right). \tag{11}$$

As an example, let $f(x_c) = f(x, x^*) = x^*x = \|x\|^2 = a^2 + b^2$, be a real function of complex variable which is the squared Euclidean distance to the origin, with $x = a + jb$. Then,

$$f(x_c) = f\left(x, x^*\right) = x^*x = \underbrace{a^2 + b^2}_{=u} + j\underbrace{(ab - ab)}_{=v} = y$$

as $v = 0$, clearly the Cauchy-Riemann equations do not hold and hence $f(x_c) = f(x, x^*) = x^*x$ is not analytic or non-holomorphic function. To overcome this apparent difficult, by applying the *CR-Calculus* leads to

$$\frac{\partial f(x_c)}{\partial x} = x^*; \qquad \frac{\partial f(x_c)}{\partial x^*} = x,$$

which suggests the geometric interpretation showed in Fig. 1.

Its analysis allow us to infer that the direction of maximum rate of change of the objective function is given by the conjugate gradient defined in (11). Observe that its positive direction is referred to a maximization problem (dot arrow) whereas the opposite direction concerns to the cost function minimization.

Remarks: (1) Hereafter, a real-valued or complex-valued function and its argument are provided with a subscript c if it is a function in the complex conjugate coordinates, i.e., (x, x^*). (2) When the *CR-Calculus* is extended to the vector case, it is denoted the multivariate *CR-Calculus* and the basic rules for the scalar case remain unchanged.

3. Complex-valued power flow modeling

3.1. Complex-valued power flow equations

The complex-valued power flow equations that model any type of branch in an electrical network, i.e., transmission lines and phase- and phase-shifting-transformers are as follows:

$$S_{km} = V_k\left(\frac{y^*_{km}}{a_{km}a^*_{km}} - jb^{sh}_{km}\right)V^*_k - V_k\frac{y^*_{km}}{a_{km}}V^*_m, \tag{12}$$

$$S_{mk} = V_m(y^*_{km} - jb^{sh}_{km})V^*_m - V_m\frac{y^*_{km}}{a^*_{km}}V^*_k. \tag{13}$$

and their complex conjugate counterpart are

$$S^*_{km} = V^*_k\left(\frac{y_{km}}{a^*_{km}a_{km}} + jb^{sh}_{km}\right)V_k - V^*_k\frac{y_{km}}{a^*_{km}}V_m, \tag{14}$$

$$S^*_{mk} = V^*_m(y_{km} + jb^{sh}_{km})V_m - V^*_m\frac{y_{km}}{a_{km}}V_k. \tag{15}$$

In (12)–(15), the general off-nominal tap transformer model is composed by an ideal transformer with complex turns ratio $ae^{-j\phi}$: 1 in series with its admittance or impedance [38]. Notice that the Eqs. (12)–(15) are written in rectangular coordinates. Thus, this feature allow us to solve the power flow equations formulated as a set of quadratic algebraic equations which takes into account all terms of the Taylor series expansion as outlined by Iwamoto [32]. Therefore, the exact non-linearity of the complex power flow equations is naturally retained in its formulation. Besides that, one take the advantage of replacing the Hessian matrix calculation by the mismatch vector which makes use of quadratic functions having as argument instead of current state variables (estimates) makes use of correction state variables values, i.e., Δx_i.

3.2. Bus models in the complex domain

3.2.1. Slack-bus type

The complex voltage at a *slack*-bus type is known, once the magnitude and phase-angle values are specified for the reference bus.

3.2.2. PQ-Bus Type

With the active- and reactive-power demand specified for a *PQ* node, the complex mismatches functions are expressed as

$$M_k = S_k - (P_{ks} + jQ_{ks}), \tag{16}$$

$$M^*_k = S^*_k - (P_{ks} - jQ_{ks}), \tag{17}$$

where P_{ks} and Q_{ks} are the specified active- and reactive-power injection at node k, respectively.

In order to derive the Newton-Raphson algorithm in the complex domain, the Jacobian matrix elements in complex form corresponding to each $PQ - Bus$ are formed based on the Wirtinger derivatives of M_k and M^*_k with respect to the complex and the complex conjugate nodal voltage unknowns, yielding

$$\frac{\partial M_k}{\partial V_k}\bigg|_{V^*_k=Const} = \sum_{m\in\Omega_k}\frac{\partial S_{km}}{\partial V_k}\bigg|_{V^*_k=Const}, \tag{18}$$

$$\frac{\partial M_k}{\partial V^*_k}\bigg|_{V_k=Const} = \sum_{m\in\Omega_k}\frac{\partial S_{km}}{\partial V^*_k}\bigg|_{V_k=Const}, \tag{19}$$

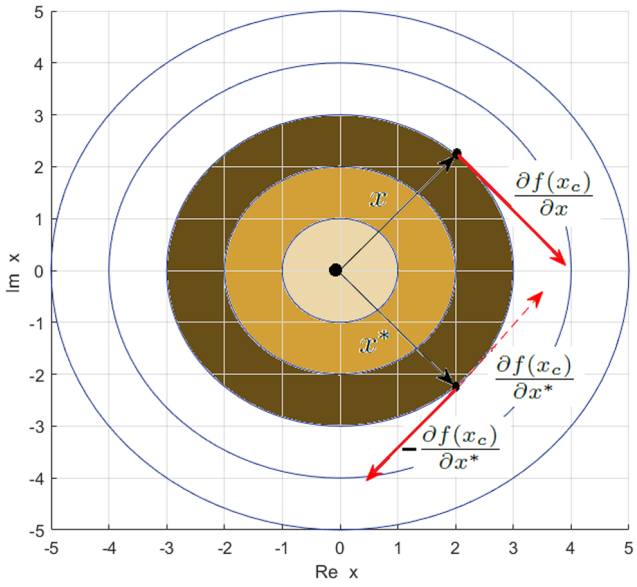

Fig. 1. Contour plot of the real function of complex variable.

$$\left.\frac{\partial M_k}{\partial V_m}\right|_{V_m^*=Const} = 0.0, \tag{20}$$

$$\left.\frac{\partial M_k}{\partial V_m^*}\right|_{V_m=Const} = \sum_{m\in\Omega_k}\left.\frac{\partial S_{km}}{\partial V_m^*}\right|_{V_m=Const}, \tag{21}$$

and

$$\left.\frac{\partial M_k^*}{\partial V_k}\right|_{V_k^*=Const} = \sum_{m\in\Omega_k}\left.\frac{\partial S_{km}^*}{\partial V_k}\right|_{V_k^*=Const}, \tag{22}$$

$$\left.\frac{\partial M_k^*}{\partial V_k^*}\right|_{V_k=Const} = \sum_{m\in\Omega_k}\left.\frac{\partial S_{km}^*}{\partial V_k^*}\right|_{V_k=Const}, \tag{23}$$

$$\left.\frac{\partial M_k^*}{\partial V_m}\right|_{V_m^*=Const} = \sum_{m\in\Omega_k}\left.\frac{\partial S_{km}^*}{\partial V_m}\right|_{V_m=Const}, \tag{24}$$

$$\left.\frac{\partial M_k^*}{\partial V_m^*}\right|_{V_m=Const} = 0.0. \tag{25}$$

where Ω_k in (18)–(25) is the set of neighboring buses connected to the $k^{th}-bus$. Moreover, in (20) and (21) and (24) and (25), $m \neq 0$ and $m \neq k$. We highlight that the *right hand side (rhs)* of (23) is the nodal complex current at node k while the *rhs* of (18) is the complex conjugate of the nodal current at node k.

3.2.3. PV-bus type

As the active-power generation and the terminal voltage magnitude at a $PV-bus$ are both specified, i.e., P_{ks} and V_{ks}, respectively, the sum of M_k in (16) and M_k^* in (17) gives the complex residual function, M_{kg}, which is related to the active-power constraint as follows:

$$\begin{aligned} M_{kg} &= M_k + M_k^*, \\ &= S_k + S_k^* - 2\times P_{ks}. \end{aligned} \tag{26}$$

The second complex residual function E_{kg} for a generator node k is formed, using the voltage magnitude constraint given by

$$|E_{kg}| = |V_k|^2 - |V_{ks}|^2, \tag{27}$$

where the $|V_{ks}|$is the specified voltage magnitude at Node k.

Using $|V_k|^2 = V_k V_k^*$, (27) can be written in the complex domain as

$$\begin{aligned} E_{kg} &= V_k V_k^* - |V_{ks}|^2, \\ &= e_k^2 + f_k^2 - |V_{ks}|^2, \end{aligned} \tag{28}$$

where e_k and f_k, respectively, are the real and imaginary part of V_k. So, it should be noted that the derivation of the current formulation in complex plane is as the rectangular formulation in real domain, i.e., it requires an extra equation at each PV bus in the system, due to the need to maintain the specified voltage magnitude (28). Consequently, the rectangular formulation has a larger equation and variable count relative to the polar formulation because of the number of PV buses in the system. Then, the Jacobian matrix elements associated with a generator node k are obtained by taking the partial derivatives of the complex residual functions in (26) and (28) with respect to V_k and V_k^*, yielding

$$\left.\frac{\partial M_{kg}}{\partial V_k}\right|_{V_k^*=Const} = \left.\frac{\partial M_k}{\partial V_k}\right|_{V_k^*=Const} + \left.\frac{\partial M_k^*}{\partial V_k}\right|_{V_k^*=Const}, \tag{29}$$

$$\left.\frac{\partial M_{kg}}{\partial V_k^*}\right|_{V_k=Const} = \left.\frac{\partial M_k}{\partial V_k^*}\right|_{V_k=Const} + \left.\frac{\partial M_k^*}{\partial V_k^*}\right|_{V_k=Const}, \tag{30}$$

$$\left.\frac{\partial M_{kg}}{\partial V_m}\right|_{V_m^*=Const} = \left.\frac{\partial M_k}{\partial V_m}\right|_{V_m^*=Const} + \left.\frac{\partial M_k^*}{\partial V_m}\right|_{V_m^*=Const}, \tag{31}$$

$$\left.\frac{\partial M_{kg}}{\partial V_m^*}\right|_{V_m=Const} = \left.\frac{\partial M_k}{\partial V_m^*}\right|_{V_m=Const} + \left.\frac{\partial M_k^*}{\partial V_m^*}\right|_{V_m=Const}, \tag{32}$$

where in (31) and (32), $m \neq 0$ and $m \neq k$. Note that the *rhs* of (29)–(32) are defined in (18)–(25).

Similarly, the partial derivatives of E_{kg} in (28) with respect to V_k and V_k^* are expressed as

$$\left.\frac{\partial E_{kg}}{\partial V_k}\right|_{V_k^*=Const} = V_k^*, \tag{33}$$

$$\left.\frac{\partial E_{kg}}{\partial V_k^*}\right|_{V_k=Const} = V_k, \tag{34}$$

while its partial derivatives with respect to V_m and V_m^* are given by

$$\left.\frac{\partial E_{kg}}{\partial V_m}\right|_{V_m^*=Const} = 0.0, \text{ for } m \neq 0 \text{ and} m \neq k, \tag{35}$$

$$\left.\frac{\partial E_{kg}}{\partial V_m^*}\right|_{V_m=Const} = 0.0, \text{ for } m \neq 0 \text{ and } m \neq k, \tag{36}$$

3.2.4. PQV-bus type

This type of bus is referred to On-Load-Tap-Changer (*OLTC*) transformer bus, which can be connected to a phase-transformer for local and nearby bus voltage regulation or to a phase-shifting-transformer for controlling the active power flow transmitted over a line [39]. It is also suited to model a DC link of a voltage-sourced converter [40]. When specifying the active- and reactive-power demand, the complex mismatch functions as stated in (16) and (17) are employed. It is worth to recall that the *OLTC* tap position allows us to regulate the voltage magnitude at either k- or m-bus. Let us assume that the m-bus voltage is regulated, leading to the following mismatches functions:

$$M_m = a_{km} - a_{km}^* - 2\times\Im\{a_{km}\}, \tag{37}$$

$$E_m = V_m V_m^* - |V_{ms}|^2, \tag{38}$$

Here, $\Im\{a_{km}\}$ is the specified imaginary part of the complex tap value. For example, for a phase-transformer, we have $\Im\{a_{km}\} = 0.0$; otherwise, it is a phase-shifter-transformer and instead of (37), (26) is used. In (38), V_{m_s} is the specified voltage at node m, i.e., the regulated nodal voltage, yielding the partial derivatives of (37) and (38) given by

$$\left.\frac{\partial M_m}{\partial a_{km}}\right|_{a_{km}^*=Const} = 1.0, \tag{39}$$

$$\left.\frac{\partial M_m}{\partial a_{km}^*}\right|_{a_{km}=Const} = -1.0, \tag{40}$$

and

$$\left.\frac{\partial E_m}{\partial V_m}\right|_{V_m^*=Const} = V_m^*, \tag{41}$$

$$\left.\frac{\partial E_m}{\partial V_m^*}\right|_{V_m=Const} = V_m. \tag{42}$$

4. Complex-valued iterative solution

4.1. The $CV-NR^{(r)}$ and $CV-LM^{(r)}$ algorithms

When the slack bus is excluded, the state variables vector becomes

$$\underline{x}_c = [V_1, V_2, ..., V_{N-1}, V_1^*, V_2^*, ..., V_{N-1}^*]^T, \tag{43}$$

and the mismatches vector reduces to

$$\underline{M}(\underline{x}_c) = [M_1, M_2, ..., M_{N-1}, M_1^*, M_2^*, ..., M_{N-1}^*]^T. \tag{44}$$

If Node k (for $k = 1, 2, ..., N-1$) is a $PV-bus$ or a $PQV-bus$, the pair of elements M_k and M_k^* in (44) are replaced by M_{kg} and E_{kg} as in (26)

and (28) or are replaced by M_m and E_m as in (37) and (38), respectively. Here, the objective is to calculate $\underline{x}_c$ that satisfies

$$\underline{M}(\underline{x}_c) = 0. \tag{45}$$

At this point, one should call the reader attention toward the mismatch vector as stated in (46) where the quadratic term of Taylor serie expansion may or not be included, yielding

$$\underline{M}(\underline{x}_c^{(\nu-1)}) = \underline{Y}_e(\underline{x}_c^{(\nu-1)}) + \underline{Y}(\Delta\underline{x}_c^{(\nu-1)}) - \underline{Y}_s, \tag{46}$$

where in (46) $\underline{Y}_s$ is a vector of specified quantities, i.e., constant term; $\underline{Y}_e(\underline{x}_c^{(\nu-1)}) = J_c^{(\nu-1)}\Delta\underline{x}_c^{(\nu-1)}$ is a vector of calculated quantities at current iteration, while $\underline{Y}(\Delta\underline{x}_c^{(\nu-1)})$ is equivalent to the 3^{th} term of the Taylor serie expansion, i.e., it retains the exact Hessian matrix effect as proved in [30]. When it is included in (46), null values are assigned to its argument, i.e., $\Delta\underline{x}_c^{(\nu=0)} = 0$. Thus, only $\underline{Y}(\Delta\underline{x}_c^{(\nu-1)})$ is updated because the term $\underline{x}_c^{(\nu=0)} = J_c^{(\nu=0)^{-1}}\underline{Y}_e(\underline{x}_c^{(\nu=0)})$ is kept constant throughout the iterative process. Consequently, the Jacobian matrix is factorized just once and the state variables are updated after convergence is reached, i.e., $\underline{x}_c = \underline{x}_c^{(\nu=0)} + \Delta\underline{x}_c^{(\nu)}$. This approach is beyond the scope of this paper and will be further developed in future work.

Let us now describe the algorithm that we have implemented. The linearization of (45) from one step to the sequel is given by

$$\begin{pmatrix}\underline{M}(\underline{x}_c^{(\nu-1)})\\ 0\end{pmatrix} + \begin{pmatrix}\mathbf{J}^{(\nu-1)}\\ \sqrt{\eta_{(\nu)}}\mathbf{I}\end{pmatrix}\Delta\underline{x}_c^{(\nu)} = 0, \tag{47}$$

or

$$\Delta\underline{x}_c^{(\nu)} = -\begin{pmatrix}\mathbf{J}^{(\nu-1)}\\ \sqrt{\eta_{(\nu)}}\mathbf{I}\end{pmatrix}^{\dagger}\begin{pmatrix}\underline{M}(\underline{x}_c^{(\nu-1)})\\ 0\end{pmatrix}, \tag{48}$$

where $\mathbf{J}$ is the complex-valued Jacobian matrix; $\mathbf{I}$ is an identity matrix of *dimension*-$2n \times 2n$;$(\cdot)^{\dagger}$ operator is defined as the Moore-Penrose pseudoinverse [41]; Finally, in (47) and (48) $\eta_{(\nu)} > 0$ is the Levenberg-Marquardt (LM) regularization parameter which influences both the length and direction of the states corrections aiming to speed up the solution reaching. As shown in Fig. 1, recall that the direction of the solution reaching is defined by $-\frac{\partial f(x_c)}{\partial x^*}$, i.e., opposite direction of the complex conjugate gradient. This important feature will be exploited in power flow problems and also extended to power system state estimation. Actually, these investigations are the partial motivation for the next forthcoming papers.

Remark that if $\eta_{(\nu)} = 0$ at the first step of LM given by (47) and (48), the LM algorithm becomes the classical Newton-Raphson method. Otherwise, it is calculated as

$$\eta_{(\nu)} = \mu_{(\nu)}\ \|\underline{M}(\underline{x}_c^{(\nu-1)})\|^{\delta}, \tag{49}$$

where the initial value of $\mu_{(\nu=0)}$ is set to 10^{-5} and δ is chosen from the range: $1 \leqslant \delta \leqslant 2$, being $\delta = 1$ a recommended value [25]. Now, instead of using only one LM step as stated in (48), two additional approximation steps are computed by utilizing the previous Jacobian matrix. The second correction step is

$$\Delta\underline{y}_c^{(\nu)} = -\begin{pmatrix}\mathbf{J}^{(\nu-1)}\\ \sqrt{\eta_{(\nu)}}\mathbf{I}\end{pmatrix}^{\dagger}\begin{pmatrix}\underline{M}(\underline{y}_c^{(\nu-1)})\\ 0\end{pmatrix}, \tag{50}$$

being $\underline{y}_c^{(\nu-1)} = \underline{x}_c^{(\nu)} = \underline{x}_c^{(\nu-1)} + \Delta\underline{x}_c^{(\nu)}$. And the third step is

$$\Delta\underline{z}_c^{(\nu)} = -\begin{pmatrix}\mathbf{J}^{(\nu-1)}\\ \sqrt{\eta_{(\nu)}}\mathbf{I}\end{pmatrix}^{\dagger}\begin{pmatrix}\underline{M}(\underline{z}_c^{(\nu-1)})\\ 0\end{pmatrix}, \tag{51}$$

assuming $\underline{z}_c^{(\nu-1)} = \underline{y}_c^{(\nu)} = \underline{y}_c^{(\nu-1)} + \Delta\underline{y}_c^{(\nu)}$. Thus, the convergence checking should be carried out over this last approximation step, yielding

$$\|\Delta\underline{z}_c^{(\nu)}\|_{\infty} \leqslant tol(\approx 10^{-3}), \tag{52}$$

where ν is the iteration counter. If (52) is satisfied, stop and print out the results. Otherwise, calculate the ratio of error deduction $err^{(\nu)} = Ared^{(\nu)}/Pred^{(\nu)}$, where

$$Ared^{(\nu)} = \|\underline{M}(\underline{x}_c^{(\nu-1)})\|^2 - \|\underline{M}(\underline{x}_c^{(\nu-1)} + \Delta\underline{x}_c^{(\nu)} + \Delta\underline{y}_c^{(\nu)} + \Delta\underline{z}_c^{(\nu)})\|^2, \tag{53}$$

$$\begin{aligned} Pred^{(\nu)} = {} & \|\underline{M}(\underline{x}_c^{(\nu-1)})\|^2 - \|\underline{M}(\underline{x}_c^{(\nu-1)}) + \mathbf{J}^{(\nu-1)}\Delta\underline{x}_c^{(\nu)}\|^2 + \\ & \|\underline{M}(\underline{y}_c^{(\nu-1)})\|^2 - \|\underline{M}(\underline{y}_c^{(\nu-1)}) + \mathbf{J}^{(\nu-1)}\Delta\underline{y}_c^{(\nu)}\|^2 + \\ & \|\underline{M}(\underline{z}_c^{(\nu-1)})\|^2 - \|\underline{M}(\underline{z}_c^{(\nu-1)}) + \mathbf{J}^{(\nu-1)}\Delta\underline{z}_c^{(\nu)}\|^2. \end{aligned} \tag{54}$$

The state vector is updated through

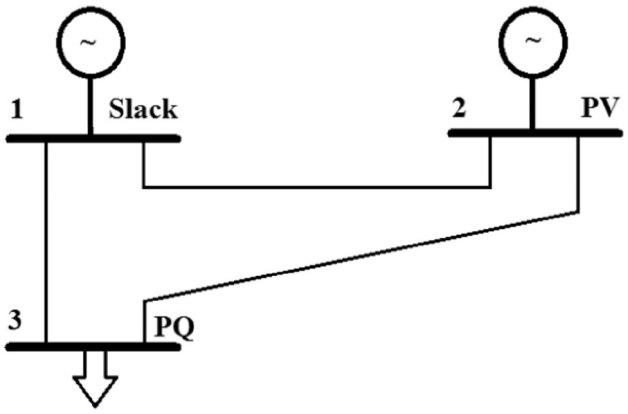

Fig. 2. One-line diagram for the 3-Bus test system.

Table 1
Bus data.

Bus	Specified Quantities in *pu*			
Type	P_g	V	P_{load}	Q_{load}
PV-2	1.0000	1.0000	0.2160	0.0918
PQ-3			2.700	1.620

Table 2
Branches data.

Branch	Serie		Shunt	
$k \rightarrow m$	R pu	X pu	Charging MVAr	Y/2 pu
1-2	0.0012	0.0021		
1-3	0.0150	0.0400		
2-3	0.3000	1.6000	39.2	0.196

Table 3
State Variables Vector.

$\underline{\mathbf{x}}_\mathbf{c}$	$\underline{\mathbf{x}}_\mathbf{c}^{(\nu=0)}$	$\underline{\mathbf{x}}_\mathbf{c}^{(\nu=1)}$	$\underline{\mathbf{x}}_\mathbf{c}^{(\nu=2)}$	$\underline{\mathbf{x}}_\mathbf{c}^{(\nu=3)}$
V_2	1.000 $e^{j0.0}$	1.000 $e^{+j0.132}$	1.000 $e^{+j0.115}$	1.000 $e^{+j0.115}$
V_3	1.000 $e^{j0.0}$	0.907 $e^{-j5.326}$	0.889 $e^{-j5.548}$	0.889 $e^{-j5.552}$
V_2^*	1.000 $\times e^{j0.0}$	1.000 $\times e^{-j0.132}$	1.000 $e^{-j0.115}$	1.000 $e^{-j0.115}$
V_3^*	1.000 $\times e^{j0.0}$	0.907 $\times e^{+j5.326}$	0.887 $e^{+j5.421}$	0.887 $e^{+j5.420}$

Table 4
CV-Power Flow Report.

CPI	*Coordinates*	
	Rectangular	*Polar*
S_1	$+ 2.0788 + j2.2844$	$3.0887 \times e^{+j47.697}$
S_2	$+ 0.7841 - j0.5449$	$0.9548 \times e^{-j34.802}$
S_3	$- 2.6999 - j1.6199$	$3.1487 \times e^{-j149.036}$
S_{12}	$- 0.7183 + j0.4114$	$0.8277 \times e^{+j150.199}$
S_{13}	$+ 2.7972 + j1.8730$	$3.3663 \times e^{+j33.806}$
S_{23}	$+ 0.0649 - j0.1350$	$0.1498 \times e^{-j64.323}$
S_{21}	$+ 0.7192 - j0.4099$	$0.8277 \times e^{-j29.686}$
S_{31}	$- 2.6368 - j1.4171$	$2.9935 \times e^{-j151.745}$
S_{32}	$- 0.0631 - j0.2028$	$0.2124 \times e^{-j107.289}$

Table 5
Features of the IEEE Test systems.

IEEE-Test Bus Systems/ SIN-	14	30	57	118	1916
No. of PV-bus (N_{PV})	4	5	6	53	163
No. of PQ-bus (N_{PQ})	9	24	50	64	1753
No. of transformers	3	4	15	9	835
No. of TL + shunt	21	43	83	200	3197
$\mathbb{R}V\text{-}^{(p)}$: $n = (N_{PV} + 2 \times N_{PQ})$	22	53	106	181	3669
$\mathbb{C}V\text{-}^{(r)}$: $n = 2 \times (N_{PV} + N_{PQ})$	26	58	112	234	3832

(TL) - Transmission Line.

$$\underline{x}_c^{(\nu)} = \begin{cases} \underline{x}_c^{(\nu-1)} + \Delta\underline{x}_c^{(\nu)} + \Delta\underline{y}_c^{(\nu)} + \Delta\underline{z}_c^{(\nu)}, & \text{if er } \mathrm{r}^{(\nu)} \geqslant p_0 \\ \underline{x}_c^{(\nu-1)}, & \text{otherwise.} \end{cases} \tag{55}$$

Finally the LM regularization parameter $\eta_{(\nu)}$ as defined in (49) is updated because $\mu_{(\nu)}$ is prone to changes as follows

$$\mu_{(\nu+1)} = \begin{cases} 4\ \mu_{(\nu)} & \text{if } \mathrm{err}^{(\nu)} < p_1 \\ \mu_{(\nu)} & \text{if } \mathrm{err}^{(\nu)} \in [p_1, p_2] \\ \max\left\{\dfrac{\mu_{(\nu)}}{4}, \bar{\lambda}\right\} & \text{if } \mathrm{err}^{(\nu)} > p_2 \end{cases} \tag{56}$$

where $0 < p_0 \leqslant p_1 \leqslant p_2 < 1$ and $\mu_{(\nu)} > \bar{\lambda} > 0$. Now, the iteration counter is updated, i.e., $\nu = \nu + 1$ and it is checked if the maximum iteration number is reached; if that is the case, terminate the algorithm and print out the results, otherwise restarts the whole process by going back to (48). Remark that the Jacobian matrix **J** is evaluated only once at the ν-th iteration, which is an appealing property for the biquadratic convergence rate of the proposed approach. The latter can be proved easily using the same theorems shown in [25]. Note that the calculation of the **J** matrix might be time consuming for large-scale systems. Thanks to the biquadratic convergence rate of the proposed approach, the number of iterations is reduced significantly. On the other hand, the linerization error of the nonlinear equation is compensated through the two additional approximate LM steps. This improves the numerical robustness of the CV-LM mainly when the power network is both under highly stressed operating conditions and presents branches with high R/X ratio. Finally, note that there are several parameters that have to be set before the iterative CV-LM has started. In this work the assumed values for these parameters are: $p_0 = 10^{-4}$, $p_1 = 0.25$, $p_2 = 0.75$ and $\lambda = 10^{-8}$ following the recommendation stated in [25,28]. This set of parameters values works well for the IEEE-test systems that we used.

4.2. The complex-valued power flow jacobian matrix

The complex-valued power flow Jacobian matrix exhibits the following pattern:

Table 6
Well-conditioned systems.

IEEE	Algorithm	# of iter	Time (s) / iter	Time (s)
-14	RV-NR$^{(p)}$	3	0.0014	0.0066
	RV-NR$^{(r)}$	3	0.0031	0.0123
	CV-NR$^{(r)}$	3	0.0028	0.0135
	RV-LM$^{(p)}$	1	0.0029	0.0039
	RV-LM$^{(r)}$	2	0.0050	0.0116
	CV-LM$^{(r)}$	2	0.0059	0.0148
	RV-OM$^{(r)}$	3	0.0073	0.0253
	CV-OM$^{(r)}$	3	0.0058	0.0214
-30	RV-NR$^{(p)}$	3	0.0023	0.0117
	RV-NR$^{(r)}$	4	0.0039	0.0192
	CV-NR$^{(r)}$	4	0.0055	0.0276
	RV-LM$^{(p)}$	2	0.0051	0.0108
	RV-LM$^{(r)}$	2	0.0052	0.0113
	CV-LM$^{(r)}$	2	0.0087	0.0199
	RV-OM$^{(r)}$	4	0.0118	0.0498
	CV-OM$^{(r)}$	5	0.0096	0.0516
-57	RV-NR$^{(p)}$	4	0.0032	0.0165
	RV-NR$^{(r)}$	4	0.0069	0.0316
	CV-NR$^{(r)}$	4	0.0082	0.0385
	RV-LM$^{(p)}$	2	0.0078	0.0156
	RV-LM$^{(r)}$	2	0.0111	0.0235
	CV-LM$^{(r)}$	2	0.0124	0.0277
	RV-OM$^{(r)}$	4	0.0183	0.0784
	CV-OM$^{(r)}$	4	0.0138	0.0613
-118	RV-NR$^{(p)}$	4	0.0061	0.0294
	RV-NR$^{(r)}$	4	0.0139	0.0585
	CV-NR$^{(r)}$	4	0.0153	0.0653
	RV-LM$^{(p)}$	2	0.0102	0.0224
	RV-LM$^{(r)}$	2	0.0212	0.0438
	CV-LM$^{(r)}$	2	0.0218	0.0460
	RV-OM$^{(r)}$	4	0.0371	0.1531
	CV-OM$^{(r)}$	4	0.0302	0.1261
SIN -1916	RV-NR$^{(p)}$	5	0.1363	0.6865
	RV-NR$^{(r)}$	6	0.2367	1.6258
	CV-NR$^{(r)}$	6	0.2161	1.3173
	RV-LM$^{(p)}$	3	0.3203	0.9724
	RV-LM$^{(r)}$	3	0.4142	1.2364
	CV-LM$^{(r)}$	3	0.4198	1.2709
	RV-OM$^{(r)}$	5	0.5761	2.918
	CV-OM$^{(r)}$	6	0.3116	1.897

(p) - polar coordinates; (r) - rectangular coordinates.

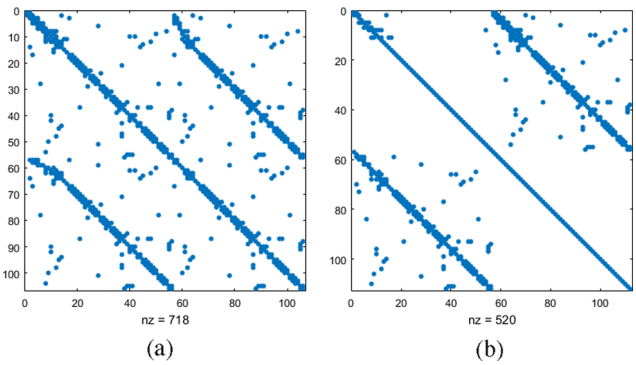

Fig. 3. Sparsity structure of (a) real-valued Jacobian matrix; (b) complex-valued Jacobian matrix of the IEEE 57-bus system.

Table 7
Ill-conditioned systems

Systems	Algorithm	Cond(**J**)	# of iter	Time(s)/iter
IEEE-11	RV-NR$^{(p)}$	-	*collapsed*	-
	RV-NR$^{(r)}$	-	*collapsed*	-
	CV-NR$^{(r)}$	-	*collapsed*	-
	RV-LM$^{(p)}$	3.21E+05	3	0.0035
	RV-LM$^{(r)}$	5.97E+07	6	0.0032
	CV-LM$^{(r)}$	1.13E+08	4	0.0048
	RV-OM$^{(r)}$	2.52E+06	6	0.0047
	CV-OM$^{(r)}$	-	*collapsed*	-
IEEE-43	RV-NR$^{(p)}$	-	*collapsed*	-
	RV-NR$^{(r)}$	-	*collapsed*	-
	CV-NR$^{(r)}$	1.34E+04	28	0.0043
	RV-LM$^{(p)}$	1.47E+08	3	0.0035
	RV-LM$^{(r)}$	1.23E+07	5	0.0061
	CV-LM$^{(r)}$	1.66E+08	4	0.0075
	RV-OM$^{(r)}$	7.08E+07	6	0.0113
	CV-OM$^{(r)}$	4.39E+04	36	0.0087
SIN-1916	RV-NR$^{(p)}$	-	*collapsed*	-
	RV-NR$^{(r)}$	-	*collapsed*	-
	CV-NR$^{(r)}$	-	*collapsed*	-
	RV-LM$^{(p)}$	6.28E+07	17	0.3039
	RV-LM$^{(r)}$	-	*collapsed*	-
	CV-LM$^{(r)}$	6.20E+08	18	0.4774
	RV-OM$^{(r)}$	9.31E+08	103	0.5013
	CV-OM$^{(r)}$	-	*collapsed*	-

(p) - polar coordinates; (r) - rectangular coordinates.

Table 8
$\|\underline{M}(\underline{x}_c)\|_\infty$ in *pu* - $S_{base} = 100MVA$.

Load Factor	RV-OM$^{(r)}$	RV-LM$^{(p)}$	RV-LM$^{(r)}$	CV-LM$^{(r)}$
1.00	5.94E−07	1.05E−08	6.27E−07	8.58E−06
1.10	2.77E−11	3.76E−06	*Collapsed*	1.37E-10
1.15	1.7163	0.0027	*Collapsed*	0.0076
1.20	*Collapsed*	0.0340	*Collapsed*	0.0188
1.25	*Collapsed*	0.0529	*Collapsed*	0.0300
1.50	*Collapsed*	0.1831	*Collapsed*	0.0804

(p) - polar coordinates; (r) - rectangular coordinates

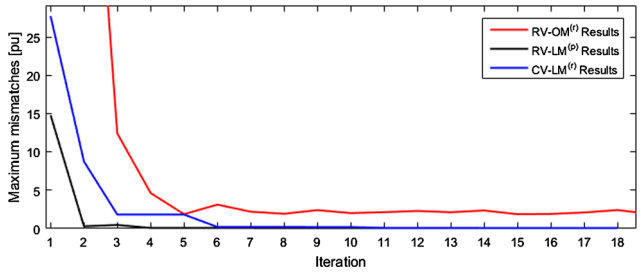

Fig. 4. Mismatches variations under a loading factor of 1.15.

$$\mathbf{J} = \begin{bmatrix} \frac{\partial M_{kg}}{\partial V_k} & \frac{\partial M_{kg}}{\partial V_m} & \frac{\partial M_{kg}}{\partial a_{km}} & \frac{\partial M_{kg}}{\partial V_k^*} & \frac{\partial M_{kg}}{\partial V_m^*} & \frac{\partial M_{kg}}{\partial a_{km}^*} \\ \frac{\partial M_k}{\partial V_k} & \frac{\partial M_k}{\partial V_m} & \frac{\partial M_k}{\partial a_{km}} & \frac{\partial M_k}{\partial V_k^*} & \frac{\partial M_k}{\partial V_m^*} & \frac{\partial M_k}{\partial a_{km}^*} \\ 0.0 & 0.0 & \frac{\partial M_m}{\partial a_{km}} & 0.0 & 0.0 & \frac{\partial M_m}{\partial a_{km}^*} \\ \frac{\partial E_{kg}}{\partial V_k} & 0.0 & 0.0 & \frac{\partial E_{kg}}{\partial V_k^*} & 0.0 & 0.0 \\ \frac{\partial M_k^*}{\partial V_k} & \frac{\partial M_k^*}{\partial V_m} & \frac{\partial M_k^*}{\partial a_{km}} & \frac{\partial M_k^*}{\partial V_k^*} & \frac{\partial M_k^*}{\partial V_m^*} & \frac{\partial M_k^*}{\partial a_{km}^*} \\ 0.0 & \frac{\partial E_m}{\partial V_m} & 0.0 & 0.0 & \frac{\partial E_m}{\partial V_m^*} & 0.0 \end{bmatrix}. \quad (57)$$

Table 9
Effect of R/X ratios on convergence.

R/X	RV-OM$^{(r)}$	CV-OM$^{(r)}$	RV-LM$^{(p)}$	RV-LM$^{(r)}$	CV-LM$^{(r)}$
$\Delta\theta$		IEEE-30 Bus System			
− 30°	4	6	2	2	2
− 40°	4	7	3	2	2
− 50°	4	*Collapsed*	12	12	11
− 60°	8	*Collapsed*	7	*Collapsed*	11
$\Delta\theta$		IEEE-118 Bus System			
− 30°	5	6	2	3	3
− 40°	9	*Collapsed*	7	4	12
− 50°	35	*Collapsed*	10	13	11
− 60°	*Collapsed*	*Collapsed*	8	13	12
$\Delta\theta$		SIN-1916 Bus System			
− 5°	6	6	4	4	4
− 10°	11	*Collapsed*	16	*Collapsed*	21
− 20°	*Collapsed*	*Collapsed*	21	*Collapsed*	20
− 30°	*Collapsed*	*Collapsed*	27	*Collapsed*	29
− 40°	*Collapsed*	*Collapsed*	32	*Collapsed*	31

(p) - polar coordinates; (r) - rectangular coordinates

In (57), the partial derivatives in the 1st and 4th rows correspond to PV-buses, those in the 2nd and 5th rows correspond to PQ-buses and those in the 3th and 6th rows correspond to PQV-buses. Note that here the partition matrix regarding the Levenberg-Marquardt parameter regularization is not shown once it is a diagonal matrix. Even though in order to factorize the complex-valued Jacobian matrix, two *QR*-algorithms are considered and were investigated [42,43]; the latter is formulated in polar coordinates. Both are the extension of the well-known real-valued algorithm described in [44], which was successfully applied to PSSE [45–47]. Recall that the *QR*-algorithm should be applied to an augmented matrix in order to avoid calculate and explicitly storing the *Q*-matrix. To this end, the *QR*-transformation is applied to $\mathbf{J_a}$ given by

$$\mathbf{J}_\mathbf{a}^{(\nu-1)} = \left[\begin{pmatrix} \mathbf{J}^{(\nu-1)} \\ \sqrt{\eta_{(\nu)}}\mathbf{I} \end{pmatrix} \begin{pmatrix} \underline{M}(\underline{x}_c^{(\nu-1)}) \\ 0 \end{pmatrix} \right]. \quad (58)$$

It turns out that if we store the sequence of rotations in compact form, the complex-valued Jacobian matrix can be kept constant, implying that only the right-hand-side vector is updated throughout the final iterations. Hence, the solution over the three steps of LM algorithm given by (48)–(51) can be performed as a simple back-substitution over the factorization of (58), yielding

$$\widetilde{\mathbf{J}}_\mathbf{a}^{(\nu-1)} = [\mathbf{T_c}\widetilde{\underline{M}}_c]. \quad (59)$$

where $\mathbf{T_c}$ is an upper triangular matrix of *dimension*-$4n \times 2n$, and $\widetilde{\underline{M}}_c$ comprises the corresponding rows in the updated *rhs* vector, *dimension*-$4n \times 1$, for $n = N - 1$, being N defined as the number of bus. Then, (48) can be expressed through

$$\Delta\underline{x}_c^{(\nu)} = \mathbf{T_c}\widetilde{\underline{M}}_c. \quad (60)$$

5. Numerical simulations

In this section, we provide a detailed description of the $CV - NR^{(r)}$ on a 3-bus power system. Then, we compare the performance of this algorithm with those of the CV-LM carried out on the well-conditioned IEEE-14, −30, −57 and −118 bus systems and on the ill-conditioned IEEE-11, −43 bus and 1916 bus systems. Note that these algorithms were encoded in Matlab by using sparsity technique and column approximate minimum degree (*colamd*) ordering scheme. The numerical tests were executed by using an Intel Core i5-4200 CPU @ 1.60 Hz 2.30 GHz; 6 GB of RAM and 64-bit operating system. A flat start condition is assigned to the state variables for the well-conditioned systems in all simulations. Whereas for the ill-conditioned systems, the starting values assigned to the voltage magnitude is 1.0 pu in all cases while for

the voltage phase angle the value is 0.0 rad, i.e., flat start; and fractions of the angles states. This latter are provided by the best solution under flat start condition. Notice that the Jacobian matrix is factorized at each iteration and the tolerance adopted for the convergence criterion in all simulations is 10^{-3}.

5.1. CV-power flow calculation analysis on a small example

The one-line diagram of the 3-bus system is depicted in Fig. 2 and the system bus data and branch parameters data in pu, calculated on the base values of $V_{base} = 230$ kV and $S_{base} = 100$ MVA, are provided in Tables 1 and 2, respectively.

5.1.1. CV-state variables throughout the iterations

As expected, the numerical values of the state variables calculated in the complex plane, which are displayed in Table 3, are exactly the same as those obtained in the real domain.

5.1.2. CV-Power Flow Analysis Report

Consequently, the values of the power injections and the power flows calculated in the real- and complex-domain are also the same which are displayed in Table 4.

5.2. IEEE test systems: well-conditioned systems

Table 5 provides the network features for the well-conditioned IEEE test systems. Highlight the large number of PV-bus type (≈45%) for the IEEE-118 bus system.

The results presented in Table 6 allows us to compare the number of iterations and time consuming to reach the solution of all algorithms carried out on the well-conditioned systems. The analyzes are summarized in the sequel.

- in blue rows the real- and complex-valued Newton-Raphson method performance is evaluated through its version in polar and rectangular coordinates, i.e., $RV - NR^{(p,r)}$ and $CV - NR^{(r)}$, respectively. Clearly, the version in rectangular coordinate is time consuming. However, surprisingly the version $CV - NR^{(r)}$ requires less computational overhead than $RV - NR^{(r)}$ for larger systems.
- in yellow rows the robust real- and complex-valued Levenberg-Marquardt algorithm performance is evaluated through its version in polar and rectangular coordinates, i.e., $RV - LM^{(p,r)}$ and $CV - LM^{(r)}$, respectively. Again, the version in rectangular coordinate is time consuming, but both version requires in average the half number of iterations to reach the solution due to its bi-quadratic convergence property. Nonetheless, the robust Levenberg-Marquardt methodology is addressed to deal with ill-conditioned systems.
- in brown rows the performance of the well-known optimized multiplier based load flow method is jointly presented with its version in complex plane. Highlight the $RV - OM^{(r)}$ is slower than $CV - OM^{(r)}$ in all test cases.

In all simulations analyzed in Table 6, the relative maximum bias between the corresponding state variables calculated in complex plane and in real domain is around 10^{-7}. The small differences are round-off errors due arithmetic operation of real and complex numbers.

In the sequel, highlight the sparsity structures of the Jacobian matrices in real and complex plane. For instance, Fig. 3 displays the pattern for the IEEE-57 bus system in $\mathbb{C}$-domain given by (57) as compared to that derived in $\mathbb{R}$-domain. Clearly, the diagonal blocks of the CV-Jacobian matrix are almost diagonal matrices, which speeds up its factorization.

5.3. IEEE test systems: ill-conditioned systems

The ill-conditioned systems are so inordinately sensitive to small perturbations that no numerical technique can be used with confidence. In other words, a system of linear equations is said to be ill-conditioned when some small perturbation in the system, regardless the side, can produce relatively large changes in the exact solution. Otherwise, the system is said to be well-conditioned [41]. For instance, consider:

$$\begin{aligned} 0.835x + 0.667y &= 0.168 \\ 0.333x + 0.266y &= 0.067, \end{aligned}$$

for which $\mathbf{A}$ is assumed as the coefficient matrix and $\underline{\mathbf{b}}$ as the right-hand-side (rhs) vector, thus $cond(\mathbf{A}) = 1.3238 \times 10^{+06}$ and the exact solution is $x_1 = 1$ and $x_2 = -1$; $\|\mathbf{A}\underline{\mathbf{x}} - \underline{\mathbf{b}}\|_\infty = 8.1524 \times 10^{-13}$. If $b_2 = 0.067$ is slightly perturbed to become $\hat{b}_2 = 0.066$, then the exact solution changes dramatically to become $\hat{x}_1 = -666$ and $\hat{x}_2 = 834$; $\|\mathbf{A}\hat{\underline{\mathbf{x}}} - \underline{\mathbf{b}}\|_\infty = 7.4937 \times 10^{-13}$. In this sense, the algorithms performance is compared taking into account the test systems or under heavily loaded condition or different R/X ratios aiming to reach only feasible solution. The test systems are the well-known ill-conditioned IEEE-11 and IEEE-43 bus systems [22]. Besides that, further simulations are included for the SIN-1916 buses operating under stressed condition or different R/X ratios.

Nonetheless, the numerical results for the mismatch vector have revealed that there is no feasible solution for the ill-conditioned IEEE 11-bus system. Specifically, the total load from bus 7 to 11 cannot be supplied which makes the constraints (45) violated in the majority of the nodes. Even though, the $RV - LM^{(p,r)}$ and $CV - LM^{(r)}$ provide the best possible solution. This behavior enables the $RV - LM^{(p)}$ and $CV - LM^{(r)}$ as an useful tool to support voltage instability and voltage collapse studies.

In the sequel, Table 7 gathers the results obtained through the simulations carried out on the ill-conditioned systems. All simulations carried out on the SIN-1916 bus system is under 1.15 of loading factor applied linearly to P and Q at all PQ-bus type. Similarly, the analyzes are summarized bellow.

- in blue rows, as expected, the real- and complex-valued Newton-Raphson method collapsed in all cases, regardless the coordinates system, i.e., $RV - NR^{(p,r)}$ and $CV - NR^{(r)}$. However, surprisingly for the 43-Bus system the exception is the $CV - NR^{(r)}$ which got success.
- in yellow rows, where the results obtained through the LM approaches are presented, the performance of $RV - LM^{(p)}$ and $CV - LM^{(r)}$ are the most robust in Table 7, whereas the version $RV - LM^{(r)}$ has collapsed (SIN-1916 bus system).
- in brown rows the performance of the optimized multiplier based load flow method is jointly shown with its version in complex plane. Highlight the $RV - OM^{(r)}$ performs much better than $CV - OM^{(r)}$ which agree with the conclusions stated in [34] regarding the algorithm $RV - OM$, i.e., in polar and rectangular coordinates.

Finally, note that the average value for the condition number of the CV-Jacobian matrix which is referred to the last iteration is higher than that presented before as an example of an ill-conditioned system.

5.4. Refining the performance analysis

The overall performance of the $CV - LM^{(r)}$ and $RV - LM^{(p)}$ algorithms aiming to solve ill-conditioned power flow problems allow us to claim that its robustness is effective and promising. Regardless the vector space and the size of the network, the developed algorithms exhibit very stable and reliable convergence properties since they reach a good solution under very stressed operating conditions. For ill-conditioned systems the use of the infinity norm of the mismatches vector at the end of the iterations is strongly recommended; indeed, the $\|\underline{M}(\underline{x}_c)\|_\infty$ allow us to test if the reached solution is associated with an

unsolvable system or not.

In this sense, Table 8 shows the results for the SIN 1916-bus system under additional heavy loading conditions. Notice that a loading factor of 1.0 is associated with a well-conditioned system as presented in Section 5.2. Remark that the $RV - OM^{(r)}$ collapses when a loading factor greater than 15 % is applied, whereas the $RV - LM^{(r)}$ does not support any tested overload. Finally, highlight the mismatch values determined by the $CV - LM^{(r)}$ is lower than those calculated through the $RV - LM^{(p)}$.

For instance, Fig. 4 depicts the mismatches variation throughout the iterations for the SIN 1916-bus system under a loading factor of 1.15. Clearly, the mismatches referred to the $RV - OM^{(r)}$ are not acceptable.

On the other hand, Table 9 presents the effect of different R/X ratios on convergence behavior of selected algorithms. Recall that higher R/X ratio can make a numerically well-conditioned system in an ill-conditioned one. The test cases presented in the sequence were generated under the following algorithm [31]:

1. $|Z|$ and θ are obtained from R and X of each branch impedance, i.e., $|Z| \times e^{j\theta} = |Z|(\cos\theta + j\sin\theta) = R + jX$.
2. Setting $\theta' = \theta + \Delta\theta$ to simulate high R/X ratios. For instance, $\Delta\theta = -20°; -40°$ and $-60°$.
3. R' and X' are obtained using $|Z|$ and θ' for each branch impedance, yielding $R' + jX' = |Z| \times e^{j\theta'} = |Z|(\cos\theta' + j\sin\theta')$.

The results presented in Table 9 clearly reveal that the algorithm $RV - LM^{(p)}$ and $CV - LM^{(r)}$ are the best to deal with ill-conditioned systems, regardless the size of the test system. Furthermore, the approaches $CV - OM^{(r)}$ and $RV - LM^{(r)}$ performs poorly compared to $RV - OM^{(r)}$ and $CV - LM^{(r)}$, respectively. Particularly, the comparative analysis confirm the same behavior presented and justified in [34].

6. Conclusions and future research

In this paper we have developed a complex-valued Newton-Raphson and a robust complex-valued Levenberg-Marquardt algorithm and referred versions aimed at solving well- and ill-conditioned power flow problems, respectively. It is shown that the implementation of the algorithms is straightforward and is much easier to encode them in the complex plane than in the real domain. All of the computations in the complex plane can be carried out in a very similar manner as those in the real domain, making many tools and methods developed for the latter readily available for the former domain. For ill-conditioned systems, the performance of the $CV - LM^{(r)}$ and the $RV - LM^{(p)}$ is both superior compared to the $RV - OM^{(r)}$-based power flow method, although they require a few changes in the parameters aiming to meet better performance.

As a future research, the following three objectives will be achieved.

- Firstly, the numerical algorithms to be used to factorize the complex-valued Jacobian matrix will be investigated because of in the ill-conditioned systems all the simulations are carried out on the border of the Jacobian matrix singularity. Thus, the orthogonal Givens-rotations-based methods are recommended [42,43] as their numerical robustness is superior. Nonetheless, further investigations are required in order to define what is the most effective ordering scheme that should be used jointly.
- Secondly, the complex-valued power flow analysis as stated in this paper is naturally formulated in rectangular coordinates. This feature allows us to exploit the power flow equations as a set of quadratic algebraic equations. This means that the exact non-linearity of the complex power flow equations is retained, i.e., the Taylor series expansion as outlined by Iwamoto & Tamura [32] is exact. Otherwise, it is approximated as in the Newton-Raphson method when applied to the power flow analysis and the Gauss-Newton method used to solve the power system static state estimation.
- Thirdly, the building of a power flow and a state estimation framework for hybrid AC-DC systems that include a variety of FACTS devices will be investigated [40,48–51].

Acknowledgment

Prof. Robson Pires would like to thank the CNPq - Brazilian *R & D*, for the financial support during his sabbatical year from Dec. 2014 to Nov. 2015 - Process No. [200703/2014-5] at the “Bradley Department of Electrical and Computer Engineering”, Northern Virginia Center - VTech, Falls Church, VA - USA.

References

[1] Nguyen T, Vu C. Complex-variable newton-raphson load-flow analysis with facts devices. Transmission and distribution conference and exhibition, 2005/2006 IEEE PES, May 2006. 2006. p. 183–90.
[2] Nguyen HL. Newton-raphson method in complex form [power system load flow analysis]. IEEE Trans Power Syst Aug 1997;12(3):1355–9.
[3] Nguyen HL. Newton-raphson method in complex form [power flow analysis]. Transmission and distribution conference, 1996. Proceedings., 1996 IEEE, Sep 1996. 1996. p. 591–5.
[4] Gonzalez-Vasquez FJ. The differentiation of functions of conjugate complex variables: application to power network analysis. IEEE Trans Educ November 1988;31(4):286–91.
[5] Wang Z, Cui B, Wang J. A necessary condition for power flow insolvability in power distribution systems with distributed generators. IEEE Trans Power Syst 2016;PP (99):1.
[6] S.S. Baghsorkhi and S.P. Suetin, ”Embedding AC power flow with voltage control in the complex plane: The case of analytic continuation via padé approximants,” CoRR, vol. abs/1504.03249, 2015. [Online]. Available: http://arxiv.org/abs/1504.03249.
[7] Trias A. The holomorphic embedding load flow method. 2012 IEEE power and energy society general meeting, July 2012. 2012. p. 1–8.
[8] Wirtinger W. Zur Formalen Theorie der Functionen Von Mehr Complexen Veranderlichen. Math Ann 1927;97:357–75.
[9] Pires R. Complex-valued steady-state models as applied to power flow analysis and power system state estimation [Ph.D. dissertation]. Institute of Electric Systems and Energy – ISEE, <https://repositorio.unifei.edu.br/xmlui/handle/123456789/55>, February 2018.
[10] Dzafic I, Jabr RA, Hrnjic T. Hybrid state estimation in complex variables. IEEE Trans Power Syst 2018:1–8.
[11] Adalý T, Schreier PJ. Optimization and estimation of complex-valued signals. IEEE Signal Process Mag 2014:112–28.
[12] Bonet PA. Theory and applications of bounded component analysis in complex valued signal processing [Ph.D. dissertation]. Spain: Department of Signal Theory and Communications, University of Seville; 2013.
[13] Trampitsch S. Complex-valued data estimation: Second-order statistics and widely linear estimators [Master’s thesis]. Klagenfurt, Austria: Institut für Vernetzte und Eingebettete Systeme; 2013.
[14] Sorber L, Barel MV, de Lathauwer L. Unconstrained optimization of real functions in complex variables. Soc Ind Appl Math – SIAM 2012;22(3):879–98.
[15] Adalý T, Haykin S. Tülay Adalý SH, editor. Adaptive signal processing: next-generation solutions. Hoboken, New Jersey: John Wiley and Sons Inc; 2010.
[16] Amin MF, Murase K. Complex-valued neural networks – advances and applications. In: Hirose A, Editor, Ser. IEEE Press Series on Computational Intelligence; 2013.
[17] Martínez JM. Solving nonlinear simultaneous equations with a generalization of brent’s method. BIT Numer Math 1980;20(4):501–10. https://doi.org/10.1007/BF01933643.
[18] Moré JJ, Cosnard MY. Numerical solution of nonlinear equations. ACM Trans Math Softw 1979;5(1):64–85. https://doi.org/10.1145/355815.355820.
[19] Martinez JM. Generalization of the Methods of Brent and Brown for Solving Nonlinear Simultaneous equations. SIAM J Numer Anal 1979;16(3):434–48. https://doi.org/10.1137/0716036.
[20] Tamura Y, Sakamoto K, Tayama Y. Voltage instability proximity index (vipi) based on multiple load flow solutions in ill-conditioned power systems. Proceedings of the 27th IEEE conference on decision and control, Dec 1988, Vol. 3. 1988. p. 2114–9.
[21] Tripathy SC, Prasad GD, Malik OP, Hope GS. Late discussion and closure to load-flow solutions for ill-conditioned power systems by a newton-like method. IEEE Trans Power App Syst 1984;PAS-103(8):2368.
[22] Tripathy SC, Prasad GD, Malik OP, Hope GS. Load-flow solutions for ill-conditioned power systems by a newton-like method. IEEE Power Eng Rev 1982;PER-2(10):25–6.
[23] Tripathy SC, Purge Prasad GSSSK. Load flow solution for ill-conditioned power systems by quadratically convergent newton-like method. IEE Proc C – Gen Transm Distrib 1980;127(5):273–80.
[24] Pourbagher R, Derakhshandeh SY. Application of high-order Levenberg -Marquardt method for solving the power flow problem in the ill-conditioned systems. IET Gen Transm Distrib 2016;10(12):3017–22.
[25] Yang X. A higher-order Levenberg-Marquardt method for nonlinear equations. Appl

Math Comput 2013;219(22):10682–94 Available: <http://www.sciencedirect.com/science/article/pii/S0096300313004487>.
[26] Amini K, Rostami F. Three-steps modified Levenberg-Marquardt method with a new line search for systems of nonlinear equations. J Comput Appl Math 2016;300(Supplement C):30–42 Available: <http://www.sciencedirect.com/science/article/pii/S0377042715006251>.
[27] Fan J. Accelerating the modified Levenberg-Marquardt method for nonlinear equations. Math Comput 2014;287(83):1173–87.
[28] Chen L. A high-order modified Levenberg-Marquardt method for systems of nonlinear equations with fourth-order convergence. Appl Math Comput 2016;285:79–93 Available: <http://www.sciencedirect.com/science/article/pii/S0096300316302314>.
[29] Zhao J, Mili L, Pires RC. Statistical and numerical robust state estimator for heavily loaded power systems. IEEE Trans Power Syst 2018:1–10.
[30] Iwamoto S, Tamura Y. A load flow calculation method for ill-conditioned power systems. IEEE Trans Power App Syst 1981;PAS-100(4):1736–43.
[31] Ochi T, Yamashita D, Koyanagi K, Yokoyama R. The development and the application of fast decoupled load flow method for distribution systems with high r/x ratios lines. 2013 IEEE PES Innovative Smart Grid Technologies Conference (ISGT), Feb 2013. 2013. p. 1–6.
[32] Iwamoto S, Tamura Y. A fast load flow method retaining nonlinearity. IEEE Trans Power App Syst 1978;PAS-97(5):1586–99.
[33] Shahriari A, Mokhlis H, Bakar A, well Critical reviews of load flow methods for. ill and unsolvable condition. J Electric Eng 2012;63(3):144–52 Available: <https://content.sciendo.com/view/journals/jee/63/3/article-p144.xml>.
[34] Tate JE, Overbye TJ. A comparison of the optimal multiplier in polar and rectangular coordinates. IEEE Trans Power Syst Nov 2005;20(4):1667–74.
[35] Braz LMC, Castro CA, Murati CAF. A critical evaluation of step size optimization based load flow methods. IEEE Trans Power Syst Feb 2000;15(1):202–7.
[36] Sachdev MS, Medicherla TKP. A second order load flow technique. IEEE Trans Power App Syst Jan 1977;96(1):189–97.
[37] Kreutz-Delgado K. The complex gradient operator and the CR-calculus, ArXIV e-print, arXIV:<0906.4835v1> [math.OC], pp. 1–74, June 25, 2009.
[38] Barboza L, Zürn H, Salgado R. Load tap change transformer: a modeling reminder. IEEE Power Eng Rev 2001:51–2.
[39] Verboomen J, Hertem DV, Schavemaker PH, Kling WL, Belmans R. Phase shifting transformers: principles and applications. 2005 international conference on future power systems, Nov 2005. 2005. p. 6.
[40] Pizano-Martinez A, Fuerte-Esquivel CR, Ambriz-Prez H, Acha E. Modeling of vsc-based hvdc systems for a newton-raphson opf algorithm. IEEE Trans Power Syst Nov 2007;22(4):1794–803.
[41] Meyer CD. Matrix analysis and linear algebra. Society for Industrial and Applied Mathematics – SIAM; 2000.
[42] Awasthi A, Guttal R, Al-Dhahir N, Balsara PT. Complex QR decomposition using fast plane rotations for MIMO applications. IEEE Commun Lett 2014;18(10):1743–6.
[43] Maltsev A, Pestretsov V, Maslennikov R, Khoryaev A. Triangular systolic array with reduced latency for QR-decomposition of complex matrices. IEEE International Symposium on Circuits and Systems – ISCAS. 2006. p. 385–8.
[44] Gentleman W. Least squares computations by givens transformations without square roots. J Math Appl 1974;12:329–36.
[45] Simões-Costa A, Quintana V. An orthogonal row processing algorithm for power sequential state estimation. IEEE-Trans Power App Syst 1981;100(8):3791–800.
[46] Wang JW, Quintana VH. A decoupled orthogonal row processing algorithm for power system state estimation. IEEE Trans Power App Syst 1984;PAS-103(8):2337–44.
[47] Vempati N, Slutsker IW, Tinney WF. Enhancement to givens rotations for power system state estimation. IEEE Trans Power Syst May 1991;6(2):842–9.
[48] Acha E, Rubbrecht T, Castro LM. Power flow solutions of ac/dc micro-grid structures. 2016 Power Systems Computation Conference (PSCC), June 2016. 2016. p. 1–6.
[49] Acha E, Castro LM. A generalized frame of reference for the incorporation of multi-terminal vsc-hvdc systems in power flow solutions. Electric Power Syst Res 2016;136(C):415–24 Available: <http://www.sciencedirect.com/science/article/pii/S0378779616300566>.
[50] Castro LM, Acha E. A unified modeling approach of multi-terminal vsc-hvdc links for dynamic simulations of large-scale power systems. IEEE Trans Power Syst 2016;31(6):5051–60.
[51] Acha E, Kazemtabrizi B. A new statcom model for power flows using the newton-raphson method. IEEE Trans Power Syst 2013;28(3):2455–65.

Electrical Power and Energy Systems 135 (2022) 107501

Contents lists available at ScienceDirect

International Journal of Electrical Power and Energy Systems

journal homepage: www.elsevier.com/locate/ijepes

Enhanced power flow solution in complex plane

Robson Pires [a,*], G. Chagas [a], Lamine Mili [b]

[a] Institute of Electric Systems and Energy, Federal University of Itajubá, Minas Gerais, MG 37500-903, Brazil
[b] Bradley Department of Electrical and Computer Engineering, Virginia Polytechnic Institute and State University, VA 22043, USA

ARTICLE INFO

Keywords:
Complex-valued enhanced power flow solution
Conjugate rectangular coordinates system
Quadratic mismatches functions
Ill-conditioned networks

ABSTRACT

In this paper an enhanced power flow algorithm in complex plane is proposed. The power flow models in complex plane is naturally developed in Cartesian coordinates, thus most of the constraints equations can be written as quadratic functions. Consequently, the Taylor series expansion stops in the third term and the exact nonlinearity of the quadratic complex power flow equations is retained while the remaining functions are dealt through the Newton-Raphson method. Minor changes in the codes are required to transform the Newton-Raphson method into the enhanced power flow approach in complex plane. The new algorithm exhibits either a superior behavior in well- or ill-conditioned networks. The features and advantages of the proposed algorithm are illustrated through a small example and case studies carried out either on the well- or ill-conditioned fashion of the IEEE-14, −30, −57 and −118 bus and the Brazilian Southern-equivalent of 1916-buses, termed as SIN-1916.

1. Introduction

The exact real-valued load flow formulation is not a new issue in the state-of-the-art literature. In order to achieve a more accurate model, Sachdev and Medicherla [1] proposed a second order method in polar coordinates formulation. Nonetheless, this approach still involves neglecting all the higher order terms in the Taylor's series expansion of the load flow equations. On the other hand, Iwamoto and Tamura [2] proposal is developed using rectangular coordinates and showed that no terms of the Taylor's series expansion need be neglected in their method. Moreover, in their proposal the Hessian matrix calculation is not required if all the constraints functions are quadratic. Further enhancements to the second order load flow were proposed by Roy and Rao [3] who showed that the use of a particular starting point and some suited approximations become his approach faster and requires less memory than the fast decoupled load flow (FDLF) which was taken as the benchmark in his work. In [4] some improvements in the exact load flow formulation are suggested aiming to overcome the FDLF slow convergence rate and failures when it is carried out on systems with large R/X ratios and capacitive series branches. It is conjectured that the poor FDLF performance under those conditions might be due to the approximations made while developing the FDLF model itself. In addition, a new technique is added for handling Q limit violations at PV buses. A comparative analysis of the convergence characteristics of second-order load flow methods is conducted in [5] but focused to FDLF. More recently, in [6] a new second order load flow method is proposed. It is based on the constant Jacobian matrix in polar coordinates and requires the Hessian matrix calculation. Anyway, the algorithms regarding all works mentioned earlier are aimed to solve the exact power flow problem formulated in the real domain. This procedure is followed because the power flow equations should be written in rectangular coordinates which allow to be splitted in real and imaginary parts. So, if the mismatches equations are quadratic functions their expansion in Taylor series till the third term is exact.

Nonetheless, none of the work on exact load flow model mentioned earlier shows how to deal with constraints that are not quadratic functions, e.g., on-load-tap-changer (*oltc*) and *phase-shifters* to cite a few, but recent work addresses these issues in complex plane [7]. To circumvent these weaknesses, in this work an enhanced power flow solution is proposed. As the quadratic power flow equations in complex plane are naturally formulated in rectangular coordinates, the complex-valued enhanced power flow formulation is straightforward derived and in our proposal the non-quadratic functions are dealt through the Newton-Raphson method. In order to present the effectiveness of the new method, three classes of algorithms are considered in this work and their performance are compared. The first one is the well known Newton-Raphson method in real domain and written in polar coordinates which is taken as a benchmark. The second one is the Iwamoto's approach as described in [2] otherwise developed in complex plane. The

* Corresponding author.
E-mail addresses: rpires@unifei.edu.br (R. Pires), lmili@vt.edu (L. Mili).

https://doi.org/10.1016/j.ijepes.2021.107501
Received 24 February 2021; Received in revised form 16 May 2021; Accepted 7 August 2021
Available online 9 September 2021

Nomenclature

$\underline{x}_c$	Vector of the state variables in the conjugate coordinate system
$\Delta\underline{x}_c$	Vector of the approximated state variables correction in the conjugate coordinate system
x, x^*	Complex and complex conjugate state variables
$\underline{x}_c^{(\star)}$	Solution vector for the state variables in the complex conjugate coordinates
$\Delta\underline{x}_c^{(\star)}$	Vector of the enhance state variables correction in the conjugate coordinate system
t, t^*	Complex and complex conjugate tap position
$\Re\{\cdot\}, \Im\{\cdot\}$	Real and imaginary part of a complex variable
$\mathbf{J}$	Complex-valued Jacobian matrix
$cond(\mathbf{J})$	Condition number of the Jacobian matrix
$\underline{M}$	Complex-valued mismatch vector
$(\cdot)_c$	Quantity in the complex conjugate coordinate system
$\|\cdot\|^2$	Squared Euclidean norm
ν	Iteration counter
$\|\cdot\|_\infty$	Infinity norm

third one is the proposed enhanced power flow algorithm that is also extended to the Levenberg-Marquardt approach [8] aimed to ill-conditioned networks. Notice that the contribution presented in this work is essentially based on Iwamoto's approach [2] in complex variables while allowing for multiple Jacobian matrix factorizations.

The aforementioned algorithms are identified as follows.

1. $RV-NRM_{fg}^{(p)}$ Real-valued Newton-Raphson method in polar coordinates;
2. $CV-EIA_{ag}^{(r)}$ Complex-valued enhanced power flow based on Iwamoto's approach in rectangular coordinates [2], i.e., approximate gain updating;
3. $RV-EPF_{fg}^{(r)}$ Real-valued enhanced power flow algorithm in rectangular coordinates;
4. $CV-EPF_{fg}^{(r)}$ Complex-valued enhanced power flow algorithm in rectangular coordinates;
5. $CV-ALM_{fg}^{(r)}$ Real-valued approximated Levenberg-Marquardt algorithm in rectangular coordinates;
6. $CV-ELM_{fg}^{(r)}$ Complex-valued enhanced Levenberg-Marquardt algorithm in rectangular coordinates.

The reminder of this paper is organized as follows. In Section 2 the power flow formulation in complex plane is summarized. In Section 3 is developed the enhanced power flow formulation in complex plane. Section 4 presents and discusses the set of simulations aimed to support the proposed contribution. In Section 5 are stated some conclusions and future works.

2. The complex-valued power flow formulation

2.1. General power flow equations

The general power flow equations that model any type of branch in an electrical network, i.e., transmission lines and phase- and phase-shifting-transformers can be written as follows:

$$S_{km} = V_k\left(\frac{y_{km}^*}{t_{km}t_{km}^*} - jb_{km}^{sh}\right)V_k^* - V_k\frac{y_{km}^*}{t_{km}}V_m^*, \tag{1}$$

$$S_{mk} = V_m\left(y_{km}^* - jb_{km}^{sh}\right)V_m^* - V_m\frac{y_{km}^*}{t_{km}^*}V_k^*. \tag{2}$$

and their complex conjugate counterpart are

$$S_{km}^* = V_k^*\left(\frac{y_{km}}{t_{km}^*t_{km}} + jb_{km}^{sh}\right)V_k - V_k^*\frac{y_{km}}{t_{km}^*}V_m, \tag{3}$$

$$S_{mk}^* = V_m^*\left(y_{km} + jb_{km}^{sh}\right)V_m - V_m^*\frac{y_{km}}{t_{km}}V_k. \tag{4}$$

In (1)–(4), b_{km}^{sh} is the half susceptance shunt of a transmission line π-model whereas $t_{km} = a_{km}e^{-j\varphi_{km}}$ is the general off-nominal tap transformer model. This latter is assumed an ideal transformer with complex turns ratio $t_{km} : 1$ in series with its admittance or impedance. Thus, if the corresponding branch is referred to

(i) off-nominal tap transformer: $b_{km}^{sh} = 0$ and $\varphi_{km} = 0$
(ii) pure-shifter: $b_{km}^{sh} = 0$ and $a_{km} = 1$
(iii) phase-shifter: $b_{km}^{sh} = 0$
(iv) π-transmission line: $a_{km} = 1$ and $\varphi_{km} = 0$

Thereby, regardless the branch type, all terms in (1)–(4) are quadratic functions of bus voltage. This main feature allow us to formulate the power flow problem as a set of quadratic algebraic equations. Hence, thanks to Wirtinger calculus, all terms of the Taylor series expansion can be taken into account in the solution of the emerged nonlinear system of equations in complex plane. Consequently, the exact nonlinearity of the quadratic complex power flow equations is naturally retained in the complex-valued power flow formulation as described in the sequel.

2.2. Complex-valued constraints functions

Assuming the injected complex power at each bus is given by

$$S_k = \sum_{m\in\Omega_k} S_{km}, \tag{5}$$

where Ω_k is the set of neighboring buses connected to the $k^{th}-bus$, the constraints functions are modeled as shown in the sequence.

2.2.1. PQ-bus type

Similarly to the former model, with the active- and reactive-power demand specified for a PQ node, the complex mismatches functions are expressed as

$$\begin{aligned} M_k &= S_k - (P_{ks} + jQ_{ks}), \\ M_k^* &= S_k^* - (P_{ks} - jQ_{ks}), \end{aligned} \tag{6}$$

where P_{ks} and Q_{ks} are the specified active- and reactive-power injection at node k, respectively.

2.2.2. PV-bus type

As the active-power generation and the terminal voltage magnitude at a $PV-bus$ are both specified, i.e., P_{ks} and V_{ks}, respectively, the sum of M_k and M_k^* in (6) gives the complex residual function, M_{kg}, which is related to the active-power constraint, yielding

$$\begin{aligned} M_{kg} &= M_k + M_k^*, \\ &= S_k + S_k^* - 2\times P_{ks}. \end{aligned} \tag{7}$$

The second complex residual function E_{kg} for a generator node k is formed, using the voltage magnitude constraint given by

$$\begin{aligned} E_{kg} &= V_k V_k^* - |V_{ks}|^2, \\ &= \underbrace{e_k^2 + f_k^2}_{=|V_k|^2} - |V_{ks}|^2, \end{aligned} \tag{8}$$

where e_k and f_k, respectively, are the real and imaginary part of V_k. So, it should be noted that the derivation of the current formulation in complex plane is as the rectangular formulation in real domain, i.e., it requires an extra equation at each PV-bus in the system, due to the need to maintain the specified voltage magnitude (8). Consequently, the rectangular formulation has a larger equation and variable count relative to the polar formulation because of the number of PV-bus in the system.

2.2.3. PQV-bus type

This type of bus is referred to on-load-tap-changer (*oltc*) transformer bus, which can be connected to a phase-transformer for local and nearby bus voltage regulation or to a phase-shifting-transformer for controlling the active power flow transmitted over a line. When specifying the active- and reactive-power demand, the complex mismatch functions as stated in (6) are employed. It is worth to recall that the *oltc* tap position allows us to regulate the voltage magnitude at either *k*- or *m*-bus. Let us assume that the *m*-bus voltage is regulated. Hence the following mismatches functions are adopted.

$$M_m = j\frac{\left(t_{km}^* - t_{km}\right)}{2} - \Im\left\{t_{km_s}\right\}, \tag{9}$$

$$E_m = V_m V_m^* - |V_{m_s}|^2, \tag{10}$$

where $\Im\{t_{km_s}\}$ is the specified imaginary part of the complex tap value, e.g., for a phase-transformer the $\Im\{t_{km_s}\} = 0$. Otherwise, it is a phase-shifter-transformer and instead of (9), (7) is used. In (10), V_{m_s} is the specified voltage at node *m*, i.e., the regulated nodal voltage which may be local or remote. Remark that in (9) the constraint is not a quadratic function. This apparent difficulty is easily circumvented as shown in the sequel.

3. Power flow algorithms in complex plane

The complex-valued enhanced power flow in Cartesian coordinates, i.e., $CV-EPF^{(r)}$ for short, can be formulated as follows [8]. Firstly, as the slack bus is excluded from the iterative loop, the vector of state variables in complex plane becomes

$$\underline{x}_c = \left[x_1, x_2, \ldots, x_{N-1}, x_1^*, x_2^*, \ldots, x_{N-1}^*\right]^T, \tag{11}$$

where *N* is the total number of buses. Thus, the mismatches vector reduces to

$$\underline{M}\left(\underline{x}_c\right) = \left[M_1, M_2, \ldots, M_{N-1}, M_1^*, M_2^*, \ldots, M_{N-1}^*\right]^T. \tag{12}$$

Recalling that the goal is to calculate $\underline{x}_c$ that satisfies

$$\underline{M}\left(\underline{x}_c\right) = 0. \tag{13}$$

At this point, the reader should be aware toward the nature of the constraints functions taken into account in the mismatch vector. The most noteworthy feature aiming the iterative process formulation is that no terms beyond the second order derivative exist because the original Eqs. (1)–(4) are quadratic functions in x and x^*. Indeed, this feature is used to develop the proposed algorithm, i.e., $CV-EPF$, once it allows to retain the nonlinearity without introducing any approximation or assumption into the model. Thus, without any loss of exactness, this work employs the very nice property presented by Iwamoto's approach in [2], i.e., the Hessian matrix calculation can be avoided. Consequently, the mismatch vector (13) in expanded Taylor's series becomes

$$\underline{M}\left(\underline{x}_c^{(\nu)}\right) = \underline{Y}_e\left(\underline{x}_c^{(\nu)}\right) + \underline{Y}\left(\Delta\underline{x}_c^{(\nu)}\right) - \underline{Y}_s, \tag{14}$$

where $\underline{Y}_s$ is a vector of constant terms referred as specified quantities. Whereas at each iteration, $\underline{Y}_e\left(\underline{x}_c^{(\nu)}\right) = J_c^{(\nu)}\Delta\underline{x}_c^{(\nu)}$ and $\underline{Y}\left(\Delta\underline{x}_c^{(\nu)}\right)$ are the vector of calculated quantities and the 3^{th} term of the Taylor serie expansion, respectively. Thereby, this latter is equivalent to the Hessian matrix which is complicated and of high dimensionality [2,9]. Consequently, its calculation is advantageously avoided as described in the Appendix.

Notice that in (14) the only difference between $\underline{Y}\left(\Delta\underline{x}_c^{(\nu)}\right)$ and $\underline{Y}_e\left(\underline{x}_c^{(\nu)}\right)$ is their argument. Hence, if $\underline{Y}\left(\Delta\underline{x}_c^{(\nu)}\right)$ is neglected in (14) the $CV-EPF^{(r)}$ algorithm becomes the former Newton-Raphson method in complex plane, i.e., $CV-NRM^{(r)}$ [8,10,11] in Cartesian coordinates. Hence, writing (14) in terms of $\Delta\underline{x}_c$, leads to

$$\Delta\underline{x}_c^{(\nu+1)} = -\left(\mathbf{J}^{(\nu)}\right)^{-1}\underline{M}\left(\underline{x}_c^{(\nu)}\right). \tag{15}$$

Thereby, since (15) is not approximate but intended to be exact, (9) or any other non-quadratic constraint should not be in use. Otherwise a null value is assigned to the corresponding non-quadratic function and (15) becomes an enhanced correction, i.e., it is not exact. At this stage three algorithms are formulated in complex plane and presented hereinafter.

3.1. The Iwamoto's approach in complex plane

In this algorithm the starting values assigned to the state variables stay constant throughout the iterations. Thus, also $\underline{Y}_e\left(\underline{x}_c^{(\nu=0)}\right)$ and $\mathbf{J}^{(\nu=0)}$ which are functions of $\underline{x}_c^{(\nu=0)}$ remain constant during the iterative process if they are once computed, i.e., the gain is approximate instead of full, as depicted in Fig. 1a. Thereby, this approach is termed as $CV-EPF_{ag}$ because is aimed to lighten the computational burden. Consequently, only $\Delta\underline{x}_c^{(\nu+1)}$ and $\underline{Y}\left(\Delta\underline{x}_c^{(\nu)}\right)$ change their values in the iteration process. Notice that null values are assigned to $\Delta\underline{x}_c^{(\nu=0)}$ in the fist iteration of the exact power flow loop [2]. Consequently, it is the former Newton-Raphson method. Hence, the recommended convergence criterion to be satisfied is

$$\left\|\Delta\mathbf{x}_c^{(\nu+1)} - \Delta\mathbf{x}_c^{(\nu)}\right\|_\infty \leqslant tol\left(e.g., 10^{-3}\right), \tag{16}$$

where $\Delta\mathbf{x}_c$ physically means the total voltage correction vector. Now, it is worth to highlight the fact that the following two matrices operation are done just once, i.e., the Jacobian matrix factorization and the state variables updating in (15). This latter occurs after the convergence has been reached, yielding

$$\underline{x}_c^{(\star)} = \underline{x}_c^{(0)} + \Delta\underline{x}_c^{(\nu+1)}, \tag{17}$$

where $\underline{x}_c^{(\star)}$ is the solution vector for the power flow problem. Nonetheless, as any iterative process the outcome to reach the solution is prone to the starting values assigned to the state variables. If needed, the starting point can be enhanced making at least one iteration, e.g., through the Newton-Raphson method, as shown in Fig. 1b. Thus, (17) has to be re-written, leading to

$$\underline{x}_c^{(\star)} = \underline{x}_c^{(1)} + \Delta\underline{x}_c^{(\nu+1)}. \tag{18}$$

Fig. 1 depicts both possibilities, i.e., (17) and (18), where the state

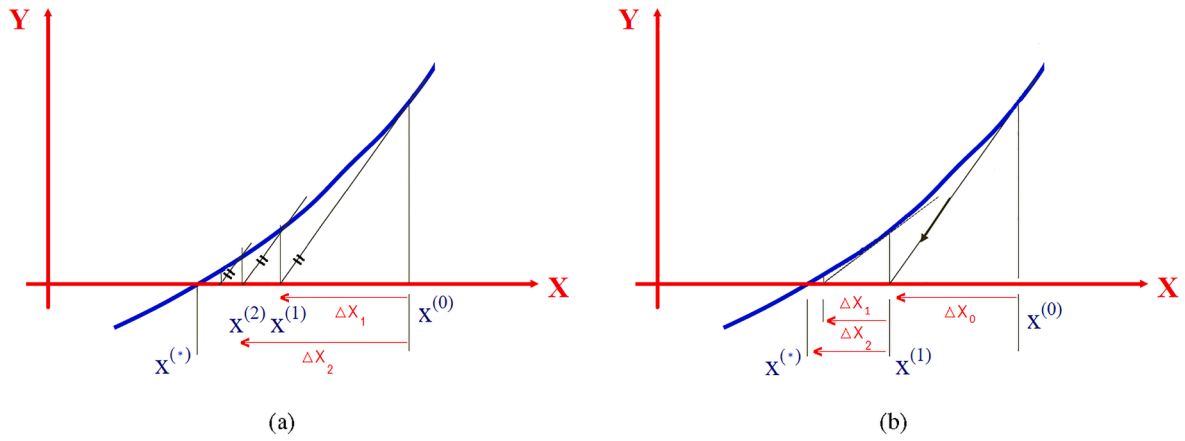

Fig. 1. Exact power flow solutions through Iwamoto's approach. (a) Starting point; (b) Enhanced starting point.

variables are updated only once, i.e., after the iterative process is over.

3.2. The Enhanced Power Flow Algorithm (CV-EPF)

Contrary to the procedure shown in Fig. 1, the proposed algorithm requires at each iteration either a full gain updating, $CV-EPF_{fg}^{(r)}$, or an approximate gain updating, $CV-EPF_{ag}^{(r)}$, for short. In the full gain mode the Jacobian matrix is updated and factorized at each iteration while in the approximate gain mode the Jacobian matrix may be kept constant. e. g., after the 2nd iteration likely the former Newton-Raphson method via approximate gain updating. Regarless the updating mode, the advantage over the Iwamoto's algorithm is the lower number of iterations required to achieve the convergence and less proneness to divergence stemmed by starting values assigned to the state variables. These issues are highlighted in the next section.

Hence, the convergence checking is carried out over the Infinity norm of two vectors. Simultaneously, it occurs over the corrections to be applied to the state variables and over the mismatches vector. This latter is included aiming to be aware against ill-conditioned systems [8], leading to

$$\left\|\Delta\underline{x}_c^{(\nu)}\right\|_\infty \; and \left\|M\left(\underline{x}_c\right)^{(\nu)}\right\|_\infty \leqslant tol\left(e.g., 10^{-3}\right). \tag{19}$$

If (19) is satisfied, stop and print out the results. Otherwise, the state variables are updated as in (20).

$$\underline{x}_c^{(\nu)} = \underline{x}_c^{(\nu-1)} + \Delta\underline{x}_c^{(\nu)}, \tag{20}$$

and the iteration counter is increased followed by the updating of the mismatch vector and the Jacobian matrix. Notice the Jacobian matrix updating and its factorization are done at each iteration if full gain mode is assumed. Thus, the fast plane rotation can be applied efficiently once this algorithm is a square root- and division-free Givens rotations [12].

3.3. The Enhanced Levenberg-Marquardt Algorithm (CV-ELM)

To assign robustness to the enhanced power flow solution in ill-conditioned networks, the enhanced Levenberg-Marquardt approach ($6.CV-ELM$) is now proposed. It is straightforward derived from the approximate Levenberg-Marquardt algorithm ($5.CV-ALM$) as presented in [8]. In fact, the Levenberg-Marquardt algorithm remain unchanged while only the corrections to be applied to the state variables are either enhanced due to the inclusion of the third term of the Taylor's series expansion or due the three corrections provided by the Levenberg-Marquardt algorithm, i.e., $\Delta\underline{x}_c^{(\nu)}$, $\Delta\underline{y}_c^{(\nu)}$ and $\Delta\underline{z}_c^{(\nu)}$ [13] yielding

$$\underline{x}_c^{(\nu)} = \begin{cases} \underline{x}_c^{(\nu-1)} + \Delta\underline{x}_c^{(\nu)} + \Delta\underline{y}_c^{(\nu)} + \Delta\underline{z}_c^{(\nu)}, \text{iferr}^{(\nu)} \geqslant p_0 \\ \underline{x}_c^{(\nu-1)} + \Delta\underline{x}_c^{(\star)}, \qquad \text{otherwise.} \end{cases} \tag{21}$$

where ν is the iteration counter; $p_0 = 10^{-4}$; $\Delta\underline{x}_c^{(\star)}$ is the enhanced correction which adds the exact effect of the third term of Taylor series expansion (see, Fig. 1). The ratio of error deduction of the Levenberg-Marquardt algorithm is given by

$$err^{(\nu)} = \frac{Ared^{(\nu)}}{Pred^{(\nu)}}, \tag{22}$$

$$Ared^{(\nu)} = \left\|\underline{M}\left(\underline{x}_c^{(\nu-1)}\right)\right\|^2 - \left\|\underline{M}\left(\underline{x}_c^{(\nu-1)} + \Delta\underline{x}_c^{(\nu)} + \Delta\underline{y}_c^{(\nu)} + \Delta\underline{z}_c^{(\nu)}\right)\right\|^2, \tag{23}$$

and

$$Pred^{(\nu)} = \left\|\underline{M}\left(\underline{x}_c^{(\nu-1)}\right)\right\|^2 - \left\|\underline{M}\left(\underline{x}_c^{(\nu-1)}\right) + \mathbf{J}^{(\nu-1)}\Delta\underline{x}_c^{(\nu)}\right\|^2 + \left\|\underline{M}\left(\underline{y}_c^{(\nu-1)}\right)\right\|^2 - \left\|\underline{M}\left(\underline{y}_c^{(\nu-1)}\right) + \mathbf{J}^{(\nu-1)}\Delta\underline{y}_c^{(\nu)}\right\|^2 + \left\|\underline{M}\left(\underline{z}_c^{(\nu-1)}\right)\right\|^2 - \left\|\underline{M}\left(\underline{z}_c^{(\nu-1)}\right) + \mathbf{J}^{(\nu-1)}\Delta\underline{z}_c^{(\nu)}\right\|^2. \tag{24}$$

For additional details, kindly report to [8].

4. Numerical simulations

In this section, the performance of the enhanced power flow algorithms described earlier is evaluated. The Iwamoto's approach which is developed with an approximate gain updating is termed as $CV-EIA_{ag}$. Instead, the proposed algorithm in this work requires full gain updating, so it is termed as $CV-EPF_{fg}$. All simulations are carried out on the standard IEEE-14, −30, −57 and −118 bus systems and on the 1916 bus systems.

All algorithms described earlier were encoded in Matlab by using

sparsity technique and column approximate minimum degree (*colamd*) ordering scheme. The numerical tests were executed by using an Intel® Core™ i5-4200 CPU @ 1.60 Hz 2.30 GHz; 6 GB of RAM and 64-bit operating system. A flat start condition is assigned to the state variables in all simulations. The tolerance adopted for the convergence criterion in all simulations is 10^{-12}. Otherwise, it is indicated in the corresponding table of results.

4.1. Small example: comparative performance in real domain

Without any loss of generality, a numerical example developed in the real domain is shown in the sequel considering the nonlinear system of equations, i.e., (25) which is taken from the Appendix. That is composed of quadratic functions as it was employed in [2] and the performance of the Newton-Raphson method and the algorithm proposed in this work, both with full gain updating can be previewed in Table 1, including the Iwamoto's approach. Notice that in this table the starting values assigned to the unknowns and the reached solution are highlighted in bold. The Newton-Raphson method needs 4 iterations to attain the convergence while the enhanced method here proposed requires 3 iterations to reach the solution. On the other hand, the Iwamoto's approach demands 9 iterations. Clearly, the proposed algorithm presents the best performance once the corrections applied to the state variables at each iteration are exact in this case while in the remaining ones the corrections are approximated. Remark that in [2] although the corrections applied to the state variables are exact the gain updating is approximate because the Jacobian matrix is kept constant throughout the iterations. Whereas in the Newton-Raphson method, nevertheless the full gain updating is employed aiming the incremental correction calculation, only the first two terms in the Taylor series expansion are taken into account. Anyway, usually for larger systems in the real domain the exact method is about 3 to 5 times faster than the Newton-Raphson method [5].

Table 2
Features of the IEEE/ SIN Test systems.

IEEE-Test Bus Systems/ SIN-	14	30	57	118	1916
No. of PV-bus (N_{PV})	4	5	6	53	163
No. of PQ-bus (N_{PQ})	9	24	50	64	1753
No. of transformers	3	4	15	9	835
No. of TL + shunt	21	43	83	200	3197
$\mathbb{R}$V-$^{(p)}$:$n = (N_{PV} + 2 \times N_{PQ})$	22	53	106	181	3669
$\mathbb{C}$V-$^{(r)}$:$n = 2 \times (N_{PV} + N_{PQ})$	26	58	112	234	3832

TL - Transmission Line.

4.2. IEEE/SIN test systems as well-conditioned systems

Table 2 provides the network features of the well-conditioned IEEE/ SIN test systems. Whereas, Table 3 allows us to make a comparative analysis of the performance referred to all algorithms carried out on the well-conditioned systems regarding the number of iterations and time consuming to reach the solution. The well known Newton-Raphson method in polar coordinates is taken as the benchmark.

Regardless whether the real or complex vector space and how large is the network, the Iwamoto's approach demands much more iterations than any other algorithm to attain the solution. For instance, see the its behavior ($2.CV - EIA_{ag}^{(r)}$) in Table 3. Moreover, aiming the solution for the SIN-1916 bus system the Iwamoto's algorithm needs an enhanced starting point to start the iterative process, as shown earlier in Fig. 1b. In

Table 1
Solution of (25) presented in the Appendix, tol.: 5×10^{-4}.

Iteration	Newton-Raphson method - full gain updating			
	$\underline{x}_e$		$\Delta\underline{x}$	
	x_{e1}	x_{e2}	Δx_1	Δx_2
0	**1.0**	**1.0**	–	–
1	0.840000000000000	1.280000000000000	−0.160000000000000	+ 0.280000000000000
2	0.800983823043909	1.202561901617696	−0.039016176956091	−0.077438098382304
3	0.800000712925059	1.200002946154031	−0.000983110118850	−0.002558955463665
4	**0.800000000000644**	**1.200000000004269**	−0.000000712924415	−0.000002946149762
Iteration	Exact Iwamoto's approach - approximate gain updating			
	$\underline{x}_e$		$\Delta\underline{x}$	
	x_{e1}	x_{e2}	Δx_1	Δx_2
0	**1.0**	**1.0**	–	–
1			−0.160000000000000	+ 0.280000000000000
2			−0.197000000000000	+ 0.168200000000000
3			−0.196075880000000	+ 0.215840240000000
4			−0.200432236598369	+ 0.193078411679926
5			−0.199442869522463	+ 0.203291377105927
6			−0.200163088277594	+ 0.198513230469437
7			−0.199900481845622	+ 0.200692695990663
8			−0.200039463087178	+ 0.199683135589635
9	**0.800019837117279**	**1.200146514220692**	−0.199980162882721	+ 0.200146514220692
Iteration	Enhanced method - full gain updating			
	$\underline{x}_e$		$\Delta\underline{x}$	
	x_{e1}	x_{e2}	Δx_1	Δx_2
0	**1.0**	**1.0**	–	–
1	0.803000000000000	1.168200000000000	−0.197000000000000	0.168200000000000
2	0.799996996729410	1.199973828390555	−0.003003003270590	0.031773828390555
3	**0.799999999999999**	**1.199999999999990**	+ 0.000003003270589	+ 0.000026171609435

Table 3
Performance in the well-conditioned systems.

(tol. $= 1.0 \times 10^{-12}$)

	Algorithms	Number of Iters.	Time/ iteration (× faster)	Total time (× faster)
IEEE-14	$1.RV-NRM_{fg}^{(p)}$	5	1	1
	$2.CV-EIA_{ag}^{(r)}$	14	31.18	1.81
	$3.RV-EPF_{fg}^{(r)}$	**5**	**2.92**	**1.86**
	$4.CV-EPF_{fg}^{(r)}$	**4**	**1.87**	**2.14**
IEEE-30	$1.RV-NRM_{fg}^{(p)}$	5	1	1
	$2.CV-EIA_{ag}^{(r)}$	21	51.5	1.92
	$3.RV-EPF_{fg}^{(r)}$	**6**	**2.28**	**2.05**
	$4.CV-EPF_{fg}^{(r)}$	**4**	**2.26**	**2.77**
IEEE-57	$1.RV-NRM_{fg}^{(p)}$	6	1	1
	$2.CV-EIA_{ag}^{(r)}$	22	11	1.46
	$3.RV-EPF_{fg}^{(r)}$	**6**	**0.92**	**1.26**
	$4.CV-EPF_{fg}^{(r)}$	**4**	**1.2**	**2.04**
IEEE-118	$1.RV-NRM_{fg}^{(p)}$	5	1	1
	$2.CV-EIA_{ag}^{(r)}$	26	11.57	1
	$3.RV-EPF_{fg}^{(r)}$	**6**	**1.13**	**1.07**
	$4.CV-EPF_{fg}^{(r)}$	**5**	**1.33**	**1.49**
SIN-1916	$1.RV-NRM_{fg}^{(p)}$	7	1	1
	$2.CV-EIA_{ag}^{(r)}$	41*	15.57	0.95
	$3.RV-EPF_{fg}^{(r)}$	**8**	**1.32**	**0.71**
	$4.CV-EPF_{fg}^{(r)}$	**5**	**0.60**	**0.76**

(p) - polar coordinates; (r) - rectangular coordinates (*) - with enhanced starting point.

this case, one iteration through Newton-Raphson method is required. Even though, further 40 iterations are needed.

Whereas, the evaluation of the proposed algorithm, i.e., $3.RV-EPF_{fg}^{(r)}$ and $4.CV-EPF_{fg}^{(r)}$ which are both highlighted in bold in Table 3 allows us to infer that the approach $4.CV-EPF_{fg}^{(r)}$ demands less iterations than $3.RV-EPF_{fg}^{(r)}$ and usually requires lower number of iterations to reach the solution in all simulations.

Besides that, it performs better than any other algorithm for the standard IEEE-test systems with respect to the total time to attain the convergence. For instance, taking as reference the well known Newton-Raphson method in polar coordinates, i.e., $1.RV-NRM_{fg}^{(p)}$, carried out on the IEEE-14, −30, −57 and −118, the approach $4.CV-EPF_{fg}^{(r)}$ is 2.14×, 2.77×, 2.04× and 1.49× faster, respectively. The exception occurs for larger systems when the time consuming becomes higher because of the arithmetic of complex numbers, e.g., SIN-916 bus system. In this case the approach $4.CV-EPF_{fg}^{(r)}$ is about 23.7% slower than $1.RV-NRM_{fg}^{(p)}$.

Table 4
Efect of $\neq$ loading factor on $\left\|\underline{M}\left(\underline{x}_c\right)\right\|_{\infty}$ (pu) and number of iterations.

Load Factor	$5.CV-ALM_{fg}^{(r)}$	$6.CV-ELM_{fg}^{(r)}$
1.10	3.61e-6 (5)	3.61e-6 (5)
1.15	0.00945 (57)	0.00941 (25)
1.20	0.0195 (100)	0.0392 (55)
1.25	0.0302 (96)	0.0306 (47)
1.50	0.1517 (47)	0.6109 (37)

(p) - polar coordinates; (r) - rectangular coordinates $S_{base} = 100$ MVA.

4.3. IEEE/SIN test systems as ill-conditioned systems

At this stage only selected algorithms are evaluated based on the studies conducted in [8]. Specifically, two scenarios are taken into account by using the SIN-1916 as the test bed.

In the first scenario the SIN-1916 is under stressed operating condition. The values assigned to the state variables before starting the iterative process are in all cases the flat start condition, i.e., 1.0 *pu* for the voltage magnitude and 0.0 *rad* for the phase angles. Also, the convergence criterion is relaxed in order to decrease the number of iterations required to attain the convergence, e.g., tol. $= 1.0 \times 10^{-03}$. In the sequel Table 4 shows the performance of the approaches $5.CV-ALM_{fg}^{(r)}$ and $6.CV-ELM_{fg}^{(r)}$. The features and advantages of the proposed algorithm are illustrated through simulations conducted under different loading factor applied linearly to the real and imaginary part, i.e., P and Q of all PQ-bus type. Notice that a loading factor of 1.0 is associated with a well-conditioned systems as presented in Section 4.2. The results reveal that the enhanced Levenberg-Marquardt approach ($6.CV-ELM_{fg}^{(r)}$) has outstanding performance compared to the previous version of the algorithm ($5.CV-ALM_{fg}^{(r)}$) as presented in [8]. Although the robustness of both algorithms is the same, in average, the number of iterations of enhanced Levenberg-Marquadt algorithm is reduced to the half.

In the second scenario, aiming to refine the performance analysis presented above, let us compare the behavior of both algorithms under the impact of different R/X ratios on the number of iterations. Recall that higher R/X ratio can make a numerically well-conditioned system in an ill-conditioned one. Aiming this purpose, the test cases presented in the sequence are generated by the algorithm proposed in [14] and is summarized as follows.

1. $|z_{km}|$ and θ_{km} are obtained from r_{km} and x_{km} of each branch impedance, i.e., $|z_{km}| \times e^{j\theta_{km}} = |z_{km}|(cos\theta_{km} + jsin\theta_{km}) = r_{km} + jx_{km}$.
2. Setting $\theta_{km}{}' = \theta_{km} + \Delta\theta_{km}$ to simulate high r_{km}/x_{km} ratios. For instance, $\Delta\theta_{km} = -20°$; $-40°$ and $-60°$.

Table 5
Effect of $\neq R/X$ ratios on $\left\|\underline{M}\left(\underline{x}_c\right)\right\|_{\infty}$ (pu) and number of iterations.

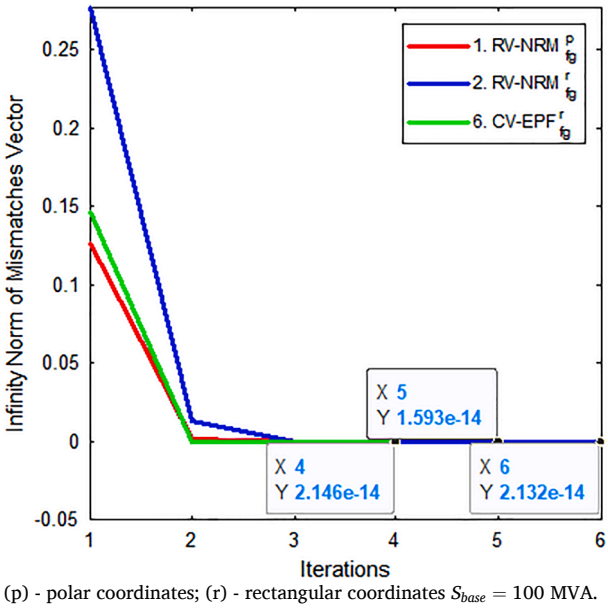

(p) - polar coordinates; (r) - rectangular coordinates $S_{base} = 100$ MVA.

3. $r_{km}{}'$ and $x_{km}{}'$ are obtained using $|z_{km}|$ and $\theta_{km}{}'$ for each branch impedance, yielding $r_{km}{}' + jx_{km}{}' = |z_{km}| \times e^{j\theta_{km}{}'} = |z_{km}|(cos\theta_{km}{}' + jsin\theta_{km}{}')$.

The overall performance is revealed in Table 5. Their contents are the maximum value (*pu*) of the Infinity norm of the mismatch vector and number of iterations. The results allow us to reach the same conclusions emerged from the Table 4, i.e., the approach 6.$CV-ELM_{fg}^{(r)}$ performs better than 5.$CV-ALM_{fg}^{(r)}$ regarding the number of iterations. On the other hand, aiming power flow analysis of ill-conditioned networks, two criterias should be satisfied. The first one is the convergence accuracy whereas the second one is the maximum value (*pu*) of the Infinity norm of the mismatches vector. Remark that in the Tables 4 and 5 the infeasible solutions are highlighted in yellow.

5. Conclusions and future research

In this paper is developed a complex-valued enhanced power flow solution aiming either well- or ill-conditioned networks. The proposed algorithm is compared to the well known Newton-Raphson method in polar coordinates, besides the Iwamoto's approach proposed in [2]. It is shown that the proposed algorithm is faster and more reliable regardless the network is either well- or ill-conditioned. The proposed technique can be conveniently incorporated in the existing *RV*- and $CV-NRM$ power flows by adding a subroutine for computing the exact effect of the second order term of the Taylor's series expansion and calculating the modified residual vector. As a future research, the following two immediate objectives will be achieved. Firstly, the numerical algorithms to be used to factorize the complex-valued Jacobian matrix will be investigated [15] because in ill-conditioned systems very often the simulations are carried out on the border of the Jacobian matrix singularity. Secondly, the complex-valued enhanced power system state estimation will be studied and developed.

Declaration of Competing Interest

The authors declare that they have no known competing financial interests or personal relationships that could have appeared to influence the work reported in this paper.

Appendix A. Numerical equivalence $f\left(\Delta\underline{\mathbf{x}}_e\right) \equiv \frac{1}{2}H\left(\underline{\mathbf{x}}_e\right)\Delta\underline{\mathbf{x}}_e^2$

Let us consider the following simple system of quadratic equations and the starting values assigned to the unknowns as being $\underline{\mathbf{x}}_e^{(\nu=0)} = [1.0; 1.0]$:

$$\begin{aligned} f_1(x) &= +2x_1^2 - 2x_1x_2 + 2x_2^2 - 2.24 \\ f_2(x) &= -2x_1^2 - 1x_1x_2 + 2x_2^2 - 0.64, \end{aligned} \tag{25}$$

which in matrix form becomes

$$\begin{aligned} [y_s] &= \begin{bmatrix} 2 & -1 & -1 & 2 \\ -2 & -0.5 & -0.5 & 2 \end{bmatrix} \cdot \begin{bmatrix} x_1x_1 \\ x_1x_2 \\ x_2x_1 \\ x_2x_2 \end{bmatrix} \\ &= \begin{bmatrix} 2 & -2 & 2 \\ -2 & -1 & 2 \end{bmatrix} \cdot \begin{bmatrix} x_1x_1 \\ x_1x_2 \\ x_2x_2 \end{bmatrix} \end{aligned} \tag{26}$$

where $y_s = [2.24; 0.64]^T$. Hence, the Taylor series expansion of (26) leads to

$$[y_s] = [y(x_e)] + \begin{bmatrix} \frac{\partial y_1}{\partial x_1} & \frac{\partial y_1}{\partial x_2} \\ \frac{\partial y_2}{\partial x_1} & \frac{\partial y_2}{\partial x_2} \end{bmatrix} \cdot \begin{bmatrix} \Delta x_1 \\ \Delta x_2 \end{bmatrix} + + \frac{1}{2} \begin{bmatrix} \frac{\partial^2 y_1}{\partial x_1^2} & 2\frac{\partial^2 y_1}{\partial x_1 \partial x_2} & \frac{\partial^2 y_1}{\partial x_2^2} \\ \frac{\partial^2 y_2}{\partial x_1^2} & 2\frac{\partial^2 y_2}{\partial x_1 \partial x_2} & \frac{\partial^2 y_2}{\partial x_2^2} \end{bmatrix} \cdot \begin{bmatrix} \Delta x_1^2 \\ \Delta x_1 \Delta x_2 \\ \Delta x_2^2 \end{bmatrix}, \tag{27}$$

or

$$\begin{bmatrix} 2.24 \\ 0.64 \end{bmatrix} = \begin{bmatrix} f_1\left(x_e^{(\nu)}\right) \\ f_2\left(x_e^{(\nu)}\right) \end{bmatrix} + \begin{bmatrix} 4x_{e_1}^{(\nu)} - 2x_{e_2}^{(\nu)} & -2x_{e_1}^{(\nu)} + 4x_{e_2}^{(\nu)} \\ -4x_{e_1}^{(\nu)} - x_{e_2}^{(\nu)} & -x_{e_1}^{(\nu)} + 4x_{e_2}^{(\nu)} \end{bmatrix} \begin{bmatrix} \Delta x_1^{(\nu)} \\ \Delta x_2^{(\nu)} \end{bmatrix} + \frac{1}{2} \begin{bmatrix} 4 & 2(-2) & 4 \\ -4 & 2(-1) & 4 \end{bmatrix} \begin{bmatrix} \Delta x_1^{2(\nu)} \\ \Delta x_1^{(\nu)} \Delta x_2^{(\nu)} \\ \Delta x_2^{2(\nu)} \end{bmatrix}, \tag{28}$$

and alternatively,

$$\begin{bmatrix} 2.24 \\ 0.64 \end{bmatrix} = \begin{bmatrix} f_1\left(x_e^{(\nu)}\right) \\ f_2\left(x_e^{(\nu)}\right) \end{bmatrix} + \begin{bmatrix} 4x_{e_1}^{(\nu)} - 2x_{e_2}^{(\nu)} & -2x_{e_1}^{(\nu)} + 4x_{e_2}^{(\nu)} \\ -4x_{e_1}^{(\nu)} - x_{e_2}^{(\nu)} & -x_{e_1}^{(\nu)} + 4x_{e_2}^{(\nu)} \end{bmatrix} \begin{bmatrix} \Delta x_1^{(\nu)} \\ \Delta x_2^{(\nu)} \end{bmatrix} + \begin{bmatrix} f_1\left(\Delta x_1^{(\nu)}\right) \\ f_2\left(\Delta x_2^{(\nu)}\right) \end{bmatrix}, \tag{29}$$

where the 2nd order term in (28) is replaced by the 1st order term in (29) except that now its arguments are the corrections imposed to the unknowns. Thus, (29) in the first iteration becomes

$$\begin{bmatrix} 2.24 \\ 0.64 \end{bmatrix} = \begin{bmatrix} 2 \\ -1 \end{bmatrix} + \begin{bmatrix} 2 & 2 \\ -5 & 3 \end{bmatrix} \cdot \begin{bmatrix} \Delta x_1 \\ \Delta x_2 \end{bmatrix}, \tag{30}$$

which can be re-written and solved, yielding

$$\begin{bmatrix} \Delta x_1 \\ \Delta x_2 \end{bmatrix} = -\begin{bmatrix} 2 & 2 \\ -5 & 3 \end{bmatrix}^{-1} \cdot \begin{bmatrix} -0.24 \\ -1.64 \end{bmatrix} = \begin{bmatrix} -0.16 \\ 0.28 \end{bmatrix}. \tag{31}$$

Now, it allow us to infer about the equivalence between the 2nd order term in (28) and the third term in (29), yielding

$$\frac{1}{2}\begin{bmatrix} 4 & -4 & 4 \\ -4 & -2 & 4 \end{bmatrix} \cdot \begin{bmatrix} (-0.16)^2 \\ (-0.16)(0.28) \\ (0.28)^2 \end{bmatrix} = \begin{bmatrix} 0.2976 \\ 0.1504 \end{bmatrix} \quad \equiv \quad \begin{bmatrix} f_1(-0.16) \\ f_2(0.28) \end{bmatrix} = \begin{bmatrix} 0.2976 \\ 0.1504 \end{bmatrix}. \tag{32}$$

This nice property holds at each iteration. Therefore, taking in mind larger systems, the use of Eq. (29) instead (28) is computationally much more advantageous.

References

[1] Sachdev MS, Medicherla TKP. A second order load flow technique. IEEE Trans Power Apparatus Syst 1977;96(1):189–97.
[2] Iwamoto S, Tamura Y. A fast load flow method retaining nonlinearity. IEEE Trans Power Apparatus Syst 1978;PAS-97(5):1586–99.
[3] Roy L. Exact Second Order Load Flow. In: Proceedings of 6-th power system computation conference (PSCC) - Cambridge - UK; 1978. p. 711–3.
[4] Nagendra Rao PS, Prakasa Rao KS, Nanda J. An exact fast load flow method including second order terms in rectangular coordinates. IEEE Trans Power Apparatus Syst 1982;PAS-101(9):3261–8.
[5] Cory B, Ekwue A, Johnson R. Comparative analysis of the convergence characteristics of second-order loadflow methods. Int J Electr Power Energy Syst 1990;12(4):251–6.
[6] Mokhlis H, Shahriari A, Laghari J. Fast and accurate second order load flow method based on fixed jacobian matrix. Appl Math Comput 2015;269:584–93 [Online]. Available: http://www.sciencedirect.com/science/article/pii/S0096300315009947.
[7] Džafic I, Jabr RA, Hrnjic T. High performance distribution network power flow using wirtinger calculus. IEEE Trans Smart Grid 2019;10(3):3311–9.
[8] Pires R, Mili L, Chagas G. Robust complex-valued Levenberg-Marquardt algorithm as applied to power flow analysis. Int J Electr Power Energy Syst 2019;113:383–92.
[9] Iwamoto S, Tamura Y. A load flow calculation method for ill-conditioned power systems. IEEE Trans Power Apparatus Syst 1981;PAS-00(4):1736–43.
[10] Wang Z, Cui B, Wang J. A necessary condition for power flow insolvability in power distribution systems with distributed generators. IEEE Trans Power Syst 2016;PP(99). pp. 1–1.
[11] Nguyen T, Vu C. Complex-variable newton-raphson load-flow analysis with facts devices. In: Transmission and Distribution Conference and Exhibition, 2005/2006 IEEE PES, May 2006. p. 183–90.
[12] Awasthi A, Guttal R, Al-Dhahir N, Balsara PT. Complex QR decomposition using fast plane rotations for MIMO applications. IEEE Commun Lett 2014;18(10):1743–6.
[13] Yang X. A higher-order Levenberg Marquardt method for nonlinear equations. Appl Math Comput 2013;219(22):10682–94 [Online]. Available: http://www.sciencedirect.com/science/article/pii/S0096300313004487.
[14] Ochi T, Yamashita D, Koyanagi K, Yokoyama R. The development and the application of fast decoupled load flow method for distribution systems with high r/x ratios lines. In: 2013 IEEE PES Innovative Smart Grid Technologies Conference (ISGT); Feb 2013. p. 1–6.
[15] Pires R. Solution Methods of Large Complex-Valued Nonlinear System of Equations. In: Bulnes F, editor. Book title: Advances in Complex Analysis and Aplications. IntechOpen; 2020. [Online]. Available: https://www.intechopen.com/books/advances-in-complex-analysis-and-applications/solution-methods-of-large-complex-valued-nonlinear-system-of-equations [chapter 4].

Robson Pires (S'98-A'99-M'02-SM'17) received his B.Sc'83, M.Sc'89. and D.Sc'98. degrees in Electrical Engineering from Fluminense Federal University (UFF) - RJ; Federal University of Itajubá (UNIFEI) - MG, and Federal University of Santa Catarina (UFSC) - SC, respectively, all in Brazil. In 1996 (Jan-Jul), he did part of his graduate program at "The Bradley Department of Electrical and Computer Engineering" - VTech, Blacksburg-VA, USA. Since 1987 he is with the Institute of Electric Systems and Energy at UNIFEI, where he is currently a Professor. His research interests include power system analysis and real-time control of wide area monitoring (WAM) and complex-valued network applications.

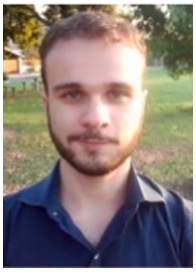

Guilherme Chagas received his B.Sc. degree in Control and Automation Engineering in 2015, M.Sc. degree in Electrical Engineering in 2018 from Federal University of Itajubá (UNIFEI) - MG, Brazil. Since 2018 he is working for pursuing the D. Sc. degree at Institute of Electric Systems and Energy (ISEE) at UNIFEI. His research interests are concerned with computer methods as applied to power systems analysis, operation and control.

Lamine Mili (Fellow'16) received the electrical engineering diploma from EPFL, Lausanne, Switzerland, in 1976, and the Ph.D. degree from the University of Liege, Liege, Belgium in 1987. He is a Professor of electrical and computer engineering at Virginia Tech. His research interests include robust statistics, power system dynamics and control and risk management of critical infrastructures. Dr. Mili has five years of industrial experience with the electric power utility, STEG, where he worked as an engineer in the planning department and the Test and Metering Laboratory from 1976 till 1981. He is co-founder and co-editor of the International Journal of Critical Infrastructures, http://www.inderscience.com/jhome.php?jcode=ijcis.

The VSC-MTDC Hybrid AC/DC Transmission Grids Solved by the Newton-Raphson Power Flow in Complex Plane

Guilherme Chagas[a], Robson Pires[a], Lamine Mili[b]

[a]*Institute of Electric Systems and Energy, Federal University of Itajubá, UNIFEI, Itajubá, Brazil*
[b]*Department of Electrical and Computer Engineering, Virginia Tech National Capital Region, Falls Church, VA 22043, USA*

Abstract

This paper presents new methodologies and modeling aimed at studying interwoven AC and DC subsystems of a power system in the complex plane. It is well known that the development of any former power flow application in real domain addressed to embedding FACTS devices is preceded by an arduous algebra task. To overcome this difficulty, a novel power flow solution method is proposed in this work. Thanks to the Wirtinger calculus, a Newton-Raphson method based on Taylor series expansions of nonlinear functions of complex variables and their complex conjugates is developed. Thus, the voltage-source-converter multi-terminal direct current is formulated in complex plane without any loss of accurateness and is termed as VSC-MTDC. Its performance is assessed through a small example and on the IEEE-test systems interconnected across a DC network prone to several scenarios, e.g., topology, loading magnitude and interchanging of active power.

Keywords: Complex-valued Newton-Raphson method, VSC-MTDC hybrid transmission grids formulated in complex plane, Wirtinger Calculus.

Nomenclature

$\underline{x}_c$	Vector of the state variables in the conjugate coordinate system
$\Delta\underline{x}_c$	Vector of the approximated state variables correction in the conjugate coordinate system
x, x^*	Complex and complex conjugate state variables
t, t^*	Complex and complex conjugate tap position
$\Re\{\cdot\}$, $\Im\{\cdot\}$	Real and imaginary part of a complex variable
$\mathbf{J}$	Complex-valued Jacobian matrix
$\underline{M}$	Complex-valued mismatch vector
$(\cdot)_c$	Quantity in the conjugate coordinate system
$\|\cdot\|_\infty$	Infinity norm
ν	Iteration counter

1. Introduction

The power flow equations are primordially complex-valued (CV) formulations. Due to their state variables, the most natural, compact and direct way to formulate it is in the Complex Domain. However, such equations are non-analytic in their phasors variables, i.e. they do not have a Taylor series expansion in therms of these complex variables alone, which is a condition for solving the Power Flow problem with numerical methods, such as Newton-Raphson. For this issue we have the Wirtinger calculus, where the equations can be expanded in terms of the complex variables and their conjugates. Another problem with this implementation is that for many decades the computers had limited processing. Thus, it was more advantageous to solve it in the real domain, replacing their complex variables by their real-valued (RV) rectangular or polar coordinates. But now the modern processors employ single instruction multiple data (SIMD), resulting in a CV formulation that is faster than the classical RV one [1], yet it has the distinct advantage of a simple software implementation.

This new scene has rescued the interest to research how the complex implementation of the power flow equations can improve the algorithms for power flow analysis and state estimation, making those algorithms

more adaptable for recent constraints such as the insertion of distributed and renewable energy generation and FACTS to the grid. [2] presents the general methods and analyses for load flow formulations using Wirtinger's calculus. [3] specializes the complex variable Newton Raphson to distribution networks. [4] proposes a CV formulation for unbalanced radial networks. [5] presents the Newton Raphson Power Flow with FACTS devices. In [6] was presented a robust Levemberg-Marquardt for solving ill-conditioned systems and in [7] an enhanced power flow solution is proposed. Likewise, in this paper a generalized VSC-MTDC power flow solution is formulated in the complex plane.

Nowadays, power transmission employing VSC-MTDC is an enhanced HVDC tecnhology of attractive application in the industry because of their well-known advantages [8]. The two most basic VSC-HVDC configurations are the back-to-back and point-to-point in either monopolar or bipolar fashions. The two monopolar VSC-HVDC links are shown schematically in Fig. 1 where each converter comprises a voltage-source-converter (VSC) and an interfacing load-tap-changer (LTC) transformer [9]. Remark that the two VSCs are series-connected on their DC sides, both sharing a capacitor in the case of the back-to-back configuration or a DC cable in the case of the point-to-point configuration. Whereas on the converters AC side, the transformer's respective primary and secondary windings are connected to the high-voltage power grid which makes each VSC to be shunt-connected with the AC system, just as if they were two STATCOM [10].

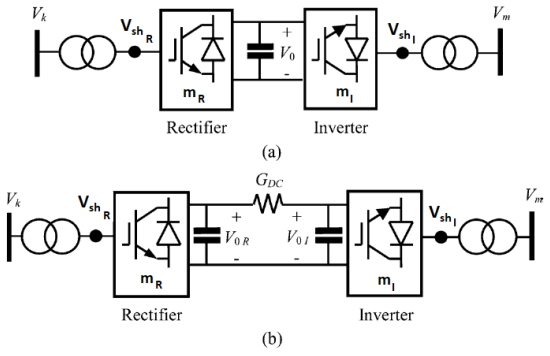

Figure 1: VSC-HVDC schematic representation. (a) Back-to-back. (b) Point-to-point.

On the other hand, Fig. 2 shows a VSC-MTDC hybrid *AC&DC* transmission grid's one line diagram. From the picture showed in the sequel one can infer that the IEEE-test systems are operated as an isolated AC subsystems, but all are interconnected through a DC grid. This latter being operated either in monopolar or bipolar configuration. Thus, it allows us to simulate a large number of scenarios taking AC isolated networks importing or exporting active power to each other. Furthermore, in spite of other FACTS devices are not shown in Fig. 2, e.g., a battery energy storage system (BESS), a PMSG-based wind farm and a photovoltaic generation system (PV), to cite a few, they can be equally DC grid connected.

Basically, in the state-of-the-art two approaches for the the hybrid AC/DC power flow can be found. In the first, the solution method is sequential [11, 12, 13] while in the second the solution is formulated in an unified fashion [14, 15, 16]. In sequential methods the AC and DC equations are solved sequentially whereas in the unified methods the hybrid systems are solved together. Both methods were first implemented considering the DC slack bus voltage control, where one VSC terminal may be selected to compensate the power imbalance of the overall DC grid. Those works were extended in [17, 18] to include the voltage droop control strategy where multiple converters can simultaneously contribute to the DC voltage stability as presented in [19, 20].

In this work both sequential and unified formulations were developed and applied to the general VSC-MTDC hybrid AC/DC transmission grid stated in complex plane. Comparing their implementation effort, Belmans *et. al.* [11] claim that the sequential approach is more advantageous because it allows to embed a MTDC system to an existing AC based power flow software. The authors share the same viewpoint and extended it towards the power flow software developed in complex plane, but the sequential solution requires an additional iterative process to solve the DC grid power flow because its inner losses are not known a priori. Regarding the VSC-MTDC voltage control strategies, once their formulations rely only on real variables they remain the

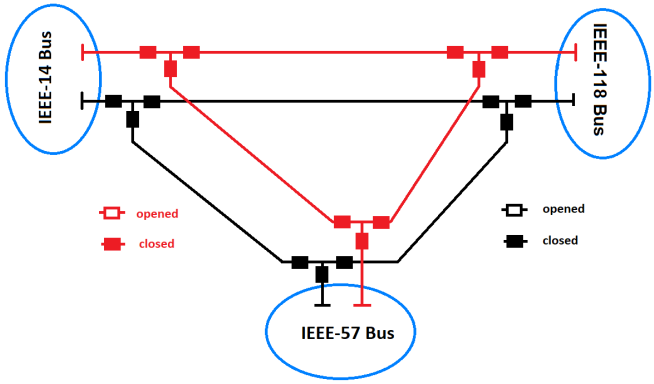

Figure 2: Hybrid AC&DC one-line diagram.

same in the complex plane. Considering this, the voltage droop control can be straightforwardly implemented from, e.g., [17] for the sequential or [18] for the unified method with no need of adaptions to CV formulation. To keep it simple this paper adopts the classic dc slack bus control strategy as it is in [11, 16].

The major contribution presented in this work is the development of a generalized VSC-MTDC power flow solution in complex plane that lands itself to an easy software implementation, and whose performance is better than the classical VSC-MTDC power flow in real variables; these features make the complex variable power flow more suited to modern processors. The formulation is solved, in the same way as [2], by Newton's method using Wirtinger's calculus, preserving the powerful convergence property of Newton's method [5]. The full complex power flow equations with no restrictions on the topology or configuration of the AC and DC networks is assumed. Moreover, without any loss of generality, the former VSC-HVDC model showed in Fig. 3 is adopted in this work [16]. The main reason is the power flow equations are functions only of the network's state variables, including the AC side of the converter. Consequently, regardless the Newton-Raphson iterative power flow algorithms, i.e., sequential or unified approach, usually it requires fewer number of iterations to reach the solution than other equivalent algorithms which model the state variables inner the converter explicitly [14].

The remainder of this paper is organized as follows. In Section II the Newton-Raphson method in complex plane is summarized. Section III presents the generalized complex-valued VSC-MTDC power flow formulation proposed in this work, including their control strategies aimed to meet the AC/DC hybrid networks operation scenarios. Section IV is addressed to show the numerical performance of the current proposals. Ending the paper, Section V presents the main conclusions and future developments.

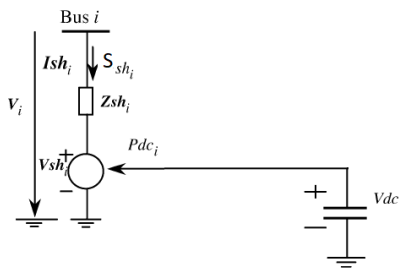

Figure 3: VSC-HVDC model.

2. Complex-Valued Newton-Raphson Method

2.1. Power flow algorithm in complex plane

For any AC network the set of complex state variables, excluding one that is referred to the slack bus, is regularly taken into account in the complex-valued iterative algorithm [2] as follows:

$$\underline{x}_c = [V_1, V_2, \ldots, V_{N-1}, V_1^*, V_2^*, \ldots, V_{N-1}^*]^T, \quad (1)$$

and the mismatches vector leads to

$$\underline{M}\left(\underline{x}_c\right) = [M_1, M_2, \ldots, M_{N-1}, M_1^*, M_2^*, \ldots, M_{N-1}^*]^T. \quad (2)$$

Nonetheless, here the goal is to calculate $\underline{x}_c$ that satisfies

$$\underline{M}\left(\underline{x}_c\right) = \underline{Y}_e(\underline{x}_c) - \underline{Y}_s = 0, \quad (3)$$

where in (3), $\underline{Y}_s$ is a vector of specified quantities, i.e., constant term; $\underline{Y}_e(\underline{x}_c) = J_c\ \Delta\underline{x}_c$ is a vector of calculated quantities at each iteration. Consequently, the linearization of (3) from one step to the sequel leads to

$$\underline{M}\left(\underline{x}_c^{(\nu-1)}\right) + \mathbf{J}^{(\nu-1)}\ \Delta\underline{x}_c^{(\nu)} = 0, \quad (4)$$

$$\text{or } \Delta\underline{x}_c^{(\nu)} = -\left(\mathbf{J}^{(\nu-1)}\right)^{-1}\ \underline{M}\left(\underline{x}_c^{(\nu-1)}\right), \quad (5)$$

where $\mathbf{J}$ is the complex-valued Jacobian matrix. As a further advantage provided by the Wirtinger calculus [21, 22], the Jacobian matrix emerged in Cartesian coordinates needs lesser algebra task as well as minor implementation effort (encoding) than the former procedure in real domain [6].

In this work the convergence checking is carried out over the Infinity norm of two vectors. Firstly, it occurs over the corrections to be applied to the state variables and simultaneously over the mismatches vector. This latter is included aiming to be aware against ill-conditioned systems [6], yielding

$$\left\|\Delta\underline{x}_c^{(\nu)}\right\|_\infty \ \textit{and}\ \left\|M(\underline{x}_c)^{(\nu)}\right\|_\infty \leq tol\ (e.g.,\ 10^{-3}). \quad (6)$$

If the constraint in (6) is satisfied, stop and print out the results. Otherwise, the state vector is updated as in (7).

$$\underline{x}_c^{(\nu)} = \underline{x}_c^{(\nu-1)} + \Delta\underline{x}_c^{(\nu)}, \quad (7)$$

and the iteration counter is increased followed by the updating of the mismatch vector and the Jacobian matrix factorization. This latter task can be mandatory or not once the Jacobian matrix may be kept constant throughout the iterative process (approximate, instead of full gain) which is a decision very often adopted after the second iteration aiming to lighten the computational burden. In the sequel is summarized the AC power flow formulation in complex plane. Further details can be found in [6].

2.2. Complex-valued power flow equations

The general complex-valued power flow equations that model any type of branch in an electrical network, i.e., *AC&DC* transmission lines and phase- and phase-shifting-transformers can be written as follows:

$$S_{km} = V_k \left(\frac{y^*_{km}}{t_{km} t^*_{km}} - j\, b^{sh}_{km} \right) V^*_k - V_k \frac{y^*_{km}}{t_{km}} V^*_m, \quad (8)$$

$$S_{mk} = V_m \left(y^*_{km} - j\, b^{sh}_{km} \right) V^*_m - V_m \frac{y^*_{km}}{t^*_{km}} V^*_k. \quad (9)$$

and their complex conjugate counterpart are

$$S^*_{km} = V^*_k \left(\frac{y_{km}}{t^*_{km} t_{km}} + j\, b^{sh}_{km} \right) V_k - V^*_k \frac{y_{km}}{t^*_{km}} V_m, \quad (10)$$

$$S^*_{mk} = V^*_m \left(y_{km} + j\, b^{sh}_{km} \right) V_m - V^*_m \frac{y_{km}}{t_{km}} V_k. \quad (11)$$

In (8-11), where $t_{km} = a_{km}\, e^{-j\varphi_{km}}$ is the general off-nominal tap transformer model which is composed by an ideal transformer with complex turns ratio $t_{km} : 1$ in series with its admittance or impedance. Hence, if the corresponding branch is referred to

1. an off-nominal tap transformer: $b^{sh}_{km} = 0$ and $\varphi_{km} = 0$
2. a pure-shifter: $b^{sh}_{km} = 0$ and $a_{km} = 1$
3. a phase-shifter: $b^{sh}_{km} = 0$
4. a $\pi-$transmission line: $a_{km} = 1$ and $\varphi_{km} = 0$
5. a DC link: $a_{km} = 1$; $\varphi_{km} = 0$; $b^{sh}_{km} = 0$ and $\Im\{\, y_{km}\} = 0$. Consequently, V_k; $V^*_k \rightarrow Vdc_k$; V_m; $V^*_m \rightarrow Vdc_m$; $S_{km} \rightarrow P_{km}$.

2.3. Complex-valued constraints functions

Assuming the injected complex power at each bus is given by

$$S_k = \sum_{m \in \Omega_k} S_{km}, \quad (12)$$

where Ω_k is the set of neighboring buses connected to the $k^{th} - bus$, the constraints functions are modeled as follows.

2.3.1. PQ-bus type

Similarly to the former model, with the active- and reactive-power demand specified for a PQ node type, the complex mismatches functions are expressed as

$$\begin{aligned} M_k &= S_k - (P_{ks} + j\, Q_{ks}), \\ M^*_k &= S^*_k - (P_{ks} - j\, Q_{ks}), \end{aligned} \quad (13)$$

where P_{ks} and Q_{ks} are the specified active- and reactive-power injection at node k, respectively.

2.3.2. PV-bus type

As the active-power generation and the terminal voltage magnitude at a $PV - bus$ type are both specified, i.e., P_{ks} and V_{ks}, respectively, the sum of M_k and M^*_k in (13) gives the complex residual function, M_{kg}, which is related to the active-power constraint, yielding

$$\begin{aligned} M_{kg} &= M_k + M^*_k, \\ &= S_k + S^*_k - 2 \times P_{ks}. \end{aligned} \quad (14)$$

The second complex residual function E_{kg} for a generator node k is formed, using the voltage magnitude constraint given by

$$\begin{aligned} E_{kg} &= V_k\, V^*_k - |V_{ks}|^2, \\ &= \underbrace{e^2_k + f^2_k}_{=|V_k|^2} - |V_{ks}|^2, \end{aligned} \quad (15)$$

where e_k and f_k, respectively, are the real and imaginary part of V_k. So, it should be noted that the derivation of the current formulation in complex plane is as the rectangular formulation in real domain, i.e., it requires an extra equation at each PV-bus in the system due to the need to maintain the specified voltage magnitude (15). Consequently, the rectangular formulation has a larger equation and variable count relative to the polar formulation because of the number of PV-bus in the system.

2.3.3. PQV-bus type

This type of bus is referred to on-load-tap-changer (OLTC) transformer bus, which can be connected to a phase-transformer for local and nearby bus voltage regulation or to a phase-shifting-transformer for controlling the active power flow transmitted over a line [23]. When specifying the active- and reactive-power demand, the complex mismatch functions as stated in (13) are employed. It is worth to recall that the OLTC tap position allows us to regulate the voltage magnitude at either $k-$ or $m-$bus. Let us assume that the $m-$bus voltage is regulated. Thus, the following mismatches functions are adopted.

$$M_m = j\, \frac{(t^*_{km} - t_{km})}{2} - \Im\{t_{km_s}\}, \quad (16)$$

$$E_m = V_m\, V^*_m - \left| V_{m_s} \right|^2, \quad (17)$$

Here, $\Im\{t_{km_s}\}$ is the specified imaginary part of the complex tap value. For instance, for a phase-transformer the $\Im\{t_{km_s}\} = 0.0$; otherwise, it is a phase-shifter-transformer and instead of (16), (14) is used. In (17), V_{m_s} is the specified voltage at node m, i.e., the regulated nodal voltage which may be local or remote.

3. Complex-Valued VSC-MTDC Formulation

3.1. The generalized complex-valued VSC-HVDC formulation

The equivalent circuit of the VSC-HVDC at the *i-th* bus is presented in Fig. 3 under the following assumptions: *i)* the system as well the VSC are three-phase balanced; *ii)* the harmonics generated by the converters are neglected. Thus, each former VSC based power flow model can be represented at the fundamental (power grid) frequency by the complex bus voltage V_{sh_i} and generalized to any number m of DC terminals, for $i = 1, 2, \cdots, m$. Based on these assumptions the general complex power flow equation at the AC side of the converter is

$$S\,sh_i = V_i\,Ish_i^* = V_i\,Ysh_i^*\,(V_i^* - Vsh_i^*), \qquad (18)$$

where $Ysh_i = 1/Zsh_i$ and $Zsh_i = (Rsh_i + j\,Xsh_i)$ is the impedance of the converter coupling transformer. Furthermore, the losses in the converter model can be represented as a function of the reactor current magnitude Ic as discussed in [24], where the coefficients a, b and c are shown in Table 1:

$$P_{loss} = a + b\,Ic + c\,Ic^2, \qquad (19)$$

$$\text{with}\;\; Ic_i = \frac{1}{\sqrt{3}}\,\sqrt{\frac{S\,sh_i\,S\,sh_i^*}{V_i\,V_i^*}}. \qquad (20)$$

Table 1: Per unit converter loss coefficients.

	a	b	c	
rectifier	11.033	3.464	4.400	x 10^{-3}
inversor			6.667	

3.2. The generalized complex-valued VSC-MTDC formulation

Firstly, it is worth suggest to the reader to take a glance on the detailed steady state VSC-MTDC models which are all developed in real domain, e.g., [14, 11, 16]. Instead, for the sake of simplicity, the VSC-HVDC shown in Fig. 3 is extended to the generalized VSC-MTDC power flow model depicted in Fig. 4. In spite of the VSC-HVDC model can be extended to any number of terminal, here it follows the same three terminal VSC-MTDC topology taken into account in [16]. Notice that if the three converters are all co-located in the same substation, i.e. they are directly connected with a common DC link, $Y_{ij} = Y_{jk} = Y_{ik} = 0$. Otherwise, i.e., $Y_{ij} \neq Y_{jk} \neq Y_{ik} \neq 0$, a DC network is explicitly represented, comprising of three DC buses and three HVDC transmission lines. Hence, the DC bus voltages Vdc_i, Vdc_j and Vdc_k are the complex-valued state variables of the DC network, i.e., $Vdc_m = (Vdc_m + j\;0.0)$ for $m = i, j, k$.

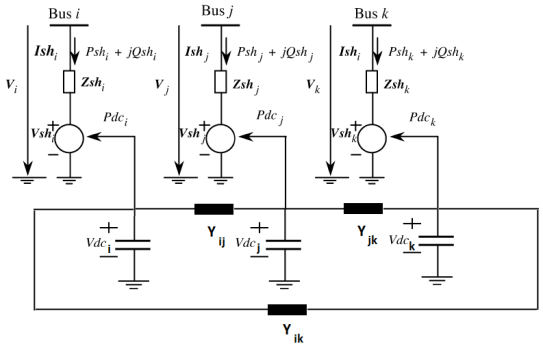

Figure 4: VSC-MTDC model.

3.3. The VSC-MTDC slack bus control strategy

Very often the converters at buses j and k are referred as *primary converters* [15, 16]. They can provide either the independent active and reactive power flow control or active power flow and voltage control. Remark that both control mode are operated in the AC side of the converters as follows.

3.3.1. PQ control mode

The converters are under the following complex power constraints

$$\begin{aligned} S\,sh_j - S\,sh_j^{spec} &= 0 \\ S\,sh_k - S\,sh_k^{spec} &= 0, \end{aligned} \qquad (21)$$

$$\begin{aligned} \text{where}\;\; S\,sh_j^{spec} &= (Psh_j^{spec} + j\,Qsh_j^{spec}) \\ S\,sh_k^{spec} &= (Psh_k^{spec} + j\,Qsh_k^{spec}), \end{aligned} \qquad (22)$$

are the complex power specified at buses j and k, respectively.

3.3.2. PV control mode

The VSC_m are under the active power flow and voltage control. Hence, the converters at buses j and k may control voltage rather than reactive power. Thus, the complex power control established in (21) have to be replaced by

$$\begin{aligned} S\,sh_j + S\,sh_j^* - 2 \times Psh_j^{spec} &= 0 \\ S\,sh_k + S\,sh_k^* - 2 \times Psh_k^{spec} &= 0, \end{aligned} \qquad (23)$$

$$\begin{aligned} \text{and} \quad V_j\, V_j^* - (V_j^{spec})^2 \quad &= 0 \\ V_k\, V_k^* - (V_k^{spec})^2 \quad &= 0, \end{aligned} \tag{24}$$

respectively.

On the other hand, the converter at bus i which in turn is referred as a *secondary converter* provides the voltage control at its DC terminal bus, yielding

$$Vdc_i\, Vdc_i^* - (Vdc_i^{spec})^2 \quad = 0, \tag{25}$$

which is equivalent to

$$Vdc_i - Vdc_i^{spec} \quad = 0, \tag{26}$$

where: $Vdc_i = (Vdc_i + j\,0.0)$. This feature allows us to infer that the DC network constraints functions are analytic or holomorphic functions, i.e., they are not function of their complex conjugate state variables. Thereby, the Cauchy-Riemann equations hold (please, see Section II of [6]), and only the complex DC state variables, i.e., $Vdc_m = (Vdc_m + j\,0.0)$ for $m = i, j, k$ are needed to solve the problem posed in (3). The remaining constraint, i.e., the active power exchange balance among the converters coupled through the DC network, including their losses, leads to

$$Pdc_{\sum} = \; Pdc_i + Pdc_j + Pdc_k + P_{loss} \quad = 0. \tag{27}$$

Notice the converter at bus i plays the role of a DC *slack* bus. Further details are provided hereafter.

3.4. The generalized DC network power flow formulation

As depicted in Fig. 4 the voltage and current relationships of a DC grid may be represented by

$$\mathbf{Y}_{dc}\, \underline{V}_{dc} = \underline{I}_{dc}, \tag{28}$$

where $\mathbf{Y}_{dc}$ is the DC network nodal admittance matrix; $\underline{V}_{dc}$ is the DC bus voltage vector which in expanded form is $\underline{V}_{dc} = [Vdc_i; Vdc_j; Vdc_k]^T$ and $\underline{I}_{dc}$ is the DC network bus current injection vector, represented by $\underline{I}_{dc} = [Idc_i; Idc_j; Idc_k]^T$, being

$$Idc_m = \; -\frac{Pdc_m}{Vdc_m}, \tag{29}$$

for $m = i, j, k$. Instead, assuming a bipolar DC grid [11] the above equation becomes

$$Idc_m = \; -\frac{Pdc_m}{2 \times Vdc_m}. \tag{30}$$

Therefore, similarly to the AC power flow formulation, a DC slack bus should be selected and the corresponding DC voltage is kept constant in the DC network nodal equation (28). Thus, equally to its AC counterpart, the DC slack bus is required to providing voltage control and balancing the active power exchange among the converters through (26) and (27), respectively. As described earlier, the converter at bus i plays the role of a DC slack bus. Hence, equations (26-30) are the basic operating constraints of the DC network, being this latter mathematically coupled with the AC side of the VSC-MTDC through the DC power exchange Pdc_i, Pdc_j, Pdc_k.

3.5. Embedding the DC network into the unified formulation

Aiming the embeddedness of the DC network into the generalized VSC-MTDC model, the power flow problem stated in (3) should be organized as follows:

$\Delta\underline{x}_c$ incremental vector of complex and complex conjugate state variables, being $\Delta\underline{x}_c = [\Delta\underline{x}_1; \Delta\underline{x}_2; \Delta\underline{x}_3; \Delta\underline{x}_1^*; \Delta\underline{x}_2^*]^T$, where

$\Delta\underline{x}_1$ incremental vector of complex AC network state variables, which in expanded form is $\Delta\underline{x}_1 = [\Delta V_i; \Delta V_j; \Delta V_k]^T$;

$\Delta\underline{x}_2$ incremental vector of complex VSC-MTDC converter state variables, which in expanded form is $\Delta\underline{x}_2 = [\Delta Vsh_i; \Delta Vsh_j; \Delta Vsh_k]^T$;

$\Delta\underline{x}_3$ incremental vector of complex DC network state variables, which in expanded form is $\Delta\underline{x}_3 = [\Delta Vdc_i; \Delta Vdc_j; \Delta Vdc_k]^T$.

$\underline{M}\left(\underline{x}_c\right)$ bus power mismatch and VSC-MTDC control mismatch vector and their complex conjugate, and $\underline{M}\left(\underline{x}_c\right) = [\underline{M}_1\left(\underline{x}_c\right); \underline{M}_2\left(\underline{x}_c\right); \underline{M}_3\left(\underline{x}_c\right); \underline{M}_1\left(\underline{x}_c\right)^*; \underline{M}_2\left(\underline{x}_c\right)^*]^T$, where

$\underline{M}_1\left(\underline{x}_c\right)$ AC network bus complex power mismatches, which in expanded form is $[S_i; S_j; S_k]^T$;

$\underline{M}_2\left(\underline{x}_c\right)$ control complex mismatches of the VSC-MTDC converters, which in expanded form is $[Pdc_{\sum}; S\,sh_j - S\,sh_j^{spec}; S\,sh_k - S\,sh_k^{spec}]^T$, whereas its complex conjugate counterpart is $\underline{M}_2\left(\underline{x}_c\right)^* = [Vdc_i - Vdc_i^{spec}; (S\,sh_j - S\,sh_j^{spec})^*; (S\,sh_k - S\,sh_k^{spec})^*]$;

$\underline{M}_3\left(\underline{x}\right)$ DC network bus complex current injections, which in compact form is $= [\mathbf{Y}_{dc}\, \underline{V}_{dc} - \underline{I}_{dc}]$.

J unified complex-valued Jacobian matrix, which in expanded form may be represented through four partitions matrix, yielding

$$\mathbf{J} = \begin{bmatrix} \frac{\partial \underline{M}_1}{\partial \underline{x}_1} & \frac{\partial \underline{M}_1}{\partial \underline{x}_2} & \frac{\partial \underline{M}_1}{\partial \underline{x}_3} & \vdots & \frac{\partial \underline{M}_1}{\partial \underline{x}_1^*} & \frac{\partial \underline{M}_1}{\partial \underline{x}_2^*} \\ \frac{\partial \underline{M}_2}{\partial \underline{x}_1} & \frac{\partial \underline{M}_2}{\partial \underline{x}_2} & \frac{\partial \underline{M}_2}{\partial \underline{x}_3} & \vdots & \frac{\partial \underline{M}_2}{\partial \underline{x}_1^*} & \frac{\partial \underline{M}_2}{\partial \underline{x}_2^*} \\ \frac{\partial \underline{M}_3}{\partial \underline{x}_1} & \frac{\partial \underline{M}_3}{\partial \underline{x}_2} & \frac{\partial \underline{M}_3}{\partial \underline{x}_3} & \vdots & \frac{\partial \underline{M}_3}{\partial \underline{x}_1^*} & \frac{\partial \underline{M}_3}{\partial \underline{x}_2^*} \\ & \cdots & & \vdots & & \cdots \\ \frac{\partial \underline{M}_1^*}{\partial \underline{x}_1} & \frac{\partial \underline{M}_1^*}{\partial \underline{x}_2} & \frac{\partial \underline{M}_1^*}{\partial \underline{x}_3} & \vdots & \frac{\partial \underline{M}_1^*}{\partial \underline{x}_1^*} & \frac{\partial \underline{M}_1^*}{\partial \underline{x}_2^*} \\ \frac{\partial \underline{M}_2^*}{\partial \underline{x}_1} & \frac{\partial \underline{M}_2^*}{\partial \underline{x}_2} & \frac{\partial \underline{M}_2^*}{\partial \underline{x}_3} & \vdots & \frac{\partial \underline{M}_2^*}{\partial \underline{x}_1^*} & \frac{\partial \underline{M}_2^*}{\partial \underline{x}_2^*} \end{bmatrix}. \quad (31)$$

3.6. Embedding the DC network into the sequential formulation

In the sequential approach, the DC grid variables are used as inputs to solve the AC equations and vice versa, which allows an easy embeddedness of DC grids into existing AC power flow programs. Thus, each network, i.e., the DC as well as the AC network have to be solved iteratively. Due to the converters loss inclusion, an extra inner loop is required to calculate the DC slack bus active power injection as a result of the nonlinear DC power flow solution. After that, the former iteration is needed to ensure the overall solution converges while the overall power flow solution changes due to the updates of the DC slack bus power injection. Further formulation details of the sequential hybrid power flow can be tracked in [11, 13].

3.7. Number of unknowns required to solve VSC-MTDC

At this stage, it is worthwhile to take stock of the unknowns and the specified quantities. The set of state variables corresponding to each converter is comprised of DC side voltages, i.e., $Vdc_m = (Vdc_m + j\ 0.0)$ for $m = j, k, \cdots$ once Vdc_i is specified and on the AC side output, for *PV control mode* the unknowns quantities are the voltage phase angles, θsh_m, whereas for *PQ control mode* the unknowns are the voltage phasor, Vsh_m, for $m = i, j, k, \cdots$. Finally, the number of complex state variables in the AC network of N buses where each converter is coupled is $n = N - 1$. In this work the sequential and unified approaches were developed in complex plane and their performance are compared under several scenarios of topology, load magnitude and interchanging of active power as described in the sequel.

4. Numerical Simulations

The unified and the sequential formulation of a CV Newton-Raphson Power Flow were programmed and executed in Matlab, using an Intel® Core™ i7 CPU 870 @ 2.93GHz; 8GB of RAM and 64-bit operating system. Two hybrid AC/DC test systems were simulated: a 5-bus example system, duplicated here from [11] in order to validate the results, and a proposed test system as presented in Fig. 2, were a MTDC grid is interconnecting different standard IEEE-test systems, e.g., IEEE-14, -57 and -118 bus systems, operating under different scenarios. A flat start condition is assigned to the state variables in all simulations. Notice that the Jacobian matrix is factorized at each iteration and the tolerance adopted for the convergence criterion in all simulations is 10^{-3}.

4.1. IEEE 5-Bus test system with a coupled MTDC Network

In order to validate the effectiveness of the developed algorithms in complex plane, i.e., the unified and sequential power flow formulations, both are carried out on the 5-bus test system with the coupled MTDC network of 3-nodes as presented in Fig. 5. The DC branch parameters used hereafter were obtained based on the results tabulated in [11].

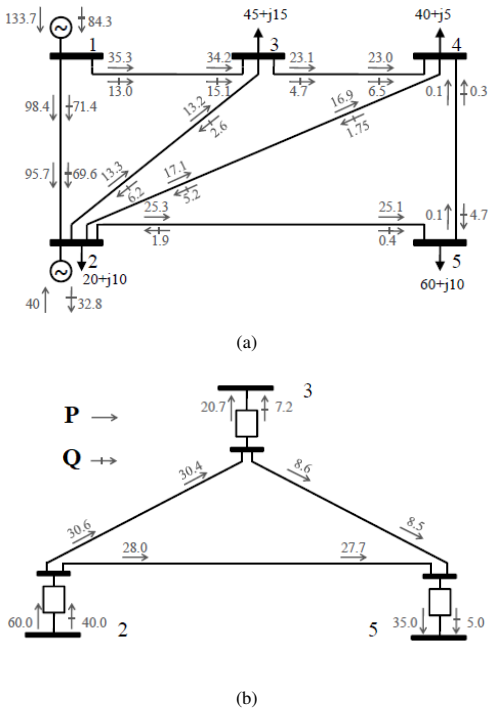

Figure 5: Hybrid *AC&DC* power flow solution.
(a) The AC 5-bus one-line diagram; (b) The DC 3-bus one-line diagram.

The AC/DC hybrid power flow solution is showed in Table 2. The same results presented in [11] which are reproduced in Fig. 5 were achieved by both algorithms developed in the complex plane, i.e., the unified and sequential approaches, which demanded 3 and 2 iterations respectively to reach the solution. Tables 3 and 4 summarize the remaining results.

4.2. IEEE-Standard systems interconnect through MTDC grid

In the sequence are provided the results obtained via simulations carried out on the AC/DC hybrid transmission system that was shown earlier in Fig. 2, considering a MTDC grid with the same specifications as presented in the previous test system. In order to demonstrate the generality of the algorithms developed in complex plane, different scenarios of operation are considered hereafter. Table 5 gathers the network features of the IEEE test systems. Basically, in all simulations a common assumption is considered, i.e., the IEEE-118 bus system is taken as an export market because of its larger number of power sources. The simulations are conducted as follows:

Case 1: IEEE-118 bus system is exporting energy to the remainder subsystems considering the same MTDC configuration as shown earlier in Fig. 2.

Case 2: The converters coupled to IEEE-14 and -57 bus systems are co-located in the same substation. The power exchanges among all subsystems are the same as considered in Case 1.

Case 3: Likely to Case 1, except that the *DC* link between the IEEE-14 and IEEE-57 subsystems is out of service. Consequently, the DC grid topology becomes radial.

Tables 6 and 7 show the results obtained through the simulations described above. Notice that both DC grid operation mode are equally simulated and included in all cases, i.e., monopolar and bipolar. In all cases, 4 and 2 iterations are required to reach the final solution for the unified and sequential methods, respectively. Moreover, the VSC voltages regarding the subsystems IEEE-14 and -57 bus suffer small changes as can be seen in Table 6 in all cases as well.

On the other hand, Table 7 presents the power flow values at each branch in the *DC* grid. Remark that the losses variation are approximately linear concerning the operation mode of the converters. The total losses under bipolar operation mode is approximately the half of those resulted under monopolar operation mode. Highlight as expected there are no losses in the link which connects the subsystems IEEE-14 and -57 bus in Case 2 once the converters referred to those subsystems are co-located in the same substation. Finally, in Case 3 the total losses have decreased because the link which connects the subsystems IEEE-14 and -57 bus is out of service.

5. Conclusions and future investigations

In this paper is developed a Newton-Raphson method in complex plane aiming to evaluate the performance of VSC-MTDC hybrid AC/DC transmission grids. It is shown that the implementation in complex plane is flexible and straightforward to model the power flow equations and FACTS devices. All of the computations in the complex plane can be carried out in a very similar manner, making many tools and methods already developed readily available to be used in the industry. As an immediate goal to be investigated is the building of an enhanced power flow and a state estimation framework aiming VSC-MTDC hybrid AC/DC transmission grids that include a variety of FACTS devices and renewable energy sources. For instance, the unified power flow controller (UPFC) which controls the real and imaginary parts of the total complex power over a transmission line, i.e., active and reactive power, simultaneously; a battery energy storage system (BESS); a PMSG-based wind farm and a photovoltaic generation system (PV), to cite a few.

Acknowledgment

Mr. Chagas is thankfull to the FAPEMIG - Brazilian *R&D*, for the financial support for his Ph.D. program since September 2018 at the Institute of Electric Systems and Energy, Federal University of Itajubá (UNIFEI), MG - Brazil.

Dr. Pires would like to thank the CNPQ - Brazilian *R&D*, for the financial support during his sabbatical year from Dec. 2014 to Nov. 2015 - Process No. [200703/2014-5] at the "Bradley Department of Electrical and Computer Engineering", Northern Virginia Center - VTech, Falls Church, VA - USA.

Table 2: Voltages and power injections report.

Converter at		*AC* Side					*DC* Side	
		VSC		Power Injection		Converter loss	Voltage	Power
bus	Control mode	V_{sh} (pu)	θ_{sh} (deg)	P_{sh} (MW)	Q_{sh} $(MVAr)$	P_{loss} (MW)	V_{dc} (pu)	P_{dc} (MW)
2	P - Q	0.984	-3.755	-60.00	-40.00	1.36	1.008	-58.60
3	Slack - V	1.003	-3.429	20.71	7.84	1.15	1.000	21.86
5	P - Q	0.993	-3.343	35.00	5.00	1.19	0.998	36.20

Table 3: Power flow report: *AC* side.

bus	type	Voltage V (pu)	Voltage θ (deg)	Power Injection P (MW)	Power Injection Q $(MVAr)$
1	Slack	1.060	0.000	133.68	84.31
2	PV	1.000	-2.384	-40.00	-82.84
3	PQ	1.000	-3.898	-24.28	-7.85
4	PQ	0.996	-4.264	-40.00	-5
5	PQ	0.991	-4.151	-25.00	-5

Branch	Direct Way P (MW)	Direct Way Q (MVA)	Reverse Way P (MW)	Reverse Way Q (MVA)	Power Loss P (MW)	Power Loss Q (MVA)
1 - 2	98.401	71.358	-95.683	-69.576	2.718	1.782
1 - 3	35.276	12.954	-34.213	-15.074	1.063	-2.120
2 - 3	13.264	-6.228	-13.148	2.576	0.116	-3.651
2 - 4	17.085	-5.185	-16.903	1.744	0.181	-3.440
2 - 5	25.334	-1.852	-25.077	-0.350	0.257	-2.202
3 - 4	23.080	4.649	-23.023	-6.472	0.056	-1.823
4 - 5	-0.073	-0.273	0.077	-4.650	0.004	-4.922
Total Power Loss					4.395	-16.377

Table 4: Power flow report: *DC* side.

Branch	Direct Way P_{dc} (MW)	Reverse Way P_{dc} (MW)	Power Loss P_{dc} (MW)
2 - 3	30.624	-30.381	0.244
2 - 5	27.979	-27.701	0.278
3 - 5	8.510	-8.493	0.017
Total Power Loss			0.539

Table 5: Features of the IEEE Test systems

IEEE-Test Bus Systems	14	57	118
No. of PV-bus (N_{PV})	4	6	53
No. of PQ-bus (N_{PQ})	9	50	64
No. of transformers	3	15	9
No. of TL + shunt	21	83	200
$\mathbb{R}$V-$^{(p)}$: $n = (N_{PV} + 2 \times N_{PQ})$	22	106	181
$\mathbb{C}$V-$^{(r)}$: $n = 2 \times (N_{PV} + N_{PQ})$	26	112	234

TL - Transmission Line

References

[1] C. J. Hughes, Single-Instruction Multiple-Data Execution, 2015.

[2] R. Pires, Complex-valued steady-state models as applied to power flow analysis and power system state estimation, Ph.D. thesis, Institute of Electric Systems and Energy - ISEE, https://repositorio.unifei.edu.br/xmlui/handle/123456789/55 (February 2018).

[3] I. Džafic, R. Jabr, T. Hrnjic, High performance distribution network power flow using wirtinger calculus, IEEE Transactions on Smart Grid (2018).

[4] J. Sarmiento, C. Alvez, B. de Nadai, A. Zambroni, E. Carreno, P. Ribeiro, A complex-valued three-phase load flow for radial networks: High-performance and low-voltage solution capability, IEEE Transactions on Power Systems (2019).

[5] T. Nguyen, C. Vu, Complex-variable newton-raphson load-flow analysis with facts devices, IEEE PES Transmission and Distribution Conference and Exhibition (2006).

[6] R. Pires, L. Mili, G. Chagas, Robust complex-valued Levenberg-Marquardt algorithm as applied to power flow analysis, International Journal of Electrical Power & Energy Systems 113 (2019) 383 – 392.

[7] R. Pires, L. Mili, G. Chagas, Enhanced power flow solution in complex plane, International Journal of Electrical Power & Energy Systems 135 (2022).

[8] D. Jovcic, High Voltage Direct Current Transmission: Converters, Systems and DC Grids, 2019.

[9] E. Acha, B. Kazemtabrizi, L. M. Castro, A new VSC-HVDC model for power flows using the Newton-Raphson method, IEEE Transactions on Power Systems 28 (3) (2013) 2602–2612.

[10] E. Acha, B. Kazemtabrizi, A new STATCOM model for power flows using the Newton–Raphson method, IEEE Transactions on Power Systems 28 (3) (2013) 2455–2465.

[11] J. Beerten, S. Cole, R. Belmans, A sequential AC/DC power flow algorithm for networks containing multi-terminal vsc hvdc systems, in: IEEE PES General Meeting, 2010, pp. 1–7.

[12] U. Arifoglu, The power flow algorithm for balanced and unbalanced bipolar multiterminal AC-DC systems, Electric Power Systems Research 64 (3) (2003) 239 – 246.

[13] M. El-Hawary, S. Ibrahim, A new approach to AC-DC load flow analysis, Electric Power Systems Research 33 (3) (1995) 193 – 200.

[14] E. Acha, L. M. Castro, A generalized frame of reference for the incorporation of multi-terminal VSC-HVDC systems in power flow solutions, Electric Power Systems Research 136 (2016) 415 – 424.

[15] S. Khan, S. Bhowmick, A novel power-flow model of multi-terminal VSC-HVDC systems, Electric Power Systems Research 133 (2016) 219 – 227.

[16] Xiao-Ping Zhang, Multiterminal voltage-sourced converter-based HVDC models for power flow analysis, IEEE Transactions on Power Systems 19 (4) (2004) 1877–1884.

Table 6: Voltages and power injections report.

Cases	Converter at				*AC* Side				*DC* Side	
					VSC		Power Injection		Voltage	Power
	Operation Mode	System	bus (type)	Control mode	V_{sh} (pu)	θ_{sh} (deg)	P_{sh} (MW)	Q_{sh} $(MVAr)$	V_{dc} (pu)	P_{dc} (MW)
Case 1	Monopolar	118-bus	59 (PV)	P - Q	0.969	-12.318	-60.00	-40.00	1.008	-58.59
		57-bus	18 (PQ)	Slack - V	1.006	-11.239	20.70	11.41	1.000	21.86
		14-bus	5 (PQ)	P - Q	1.021	-3.632	35.00	5.00	0.998	36.19
	Bipolar	118-bus	59 (PV)	P - Q	0.969	-12.318	-60.00	-40.00	1.004	-58.59
		57-bus	18 (PQ)	Slack - V	1.006	-11.188	20.97	11.44	1.000	22.13
		14-bus	5 (PQ)	P - Q	1.021	-3.632	35.00	5.00	0.999	36.19
Case 2	Monopolar	118-bus	59 (PV)	P - Q	0.969	-12.318	-60.00	-40.00	1.009	-58.59
		57-bus	18 (PQ)	Slack - V	1.006	-11.235	20.72	11.41	1.000	21.86
		14-bus	5 (PQ)	P - Q	1.021	-3.632	35.00	5.00	1.000	36.19
	Bipolar	118-bus	59 (PV)	P - Q	0.969	-12.318	-60.00	-40.00	1.004	-58.59
		57-bus	18 (PQ)	Slack - V	1.006	-11.186	20.98	11.45	1.000	22.14
		14-bus	5 (PQ)	P - Q	1.021	-3.632	35.00	5.00	1.000	36.19
Case 3	Monopolar	118-bus	59 (PV)	P - Q	0.969	-12.318	-60.00	-40.00	1.006	-58.59
		57-bus	18 (PQ)	Slack - V	1.006	-11.252	20.63	11.40	1.000	21.79
		14-bus	5 (PQ)	P - Q	1.021	-3.632	35.00	5.00	0.993	36.19
	Bipolar	118-bus	59 (PV)	P - Q	0.969	-12.318	-60.00	-40.00	1.003	-58.59
		57-bus	18 (PQ)	Slack - V	1.006	-11.194	20.93	11.44	1.000	22.10
		14-bus	5 (PQ)	P - Q	1.021	-3.632	35.00	5.00	0.996	36.19

Table 7: Power flow report: *DC* side.

Cases	Operation Mode	Branch	Direct Flow P_{dc} (MW)	Reverse Flow P_{dc} (MW)	Power Loss P_{dc} (MW)
Case 1	Monopolar	59 - 18	30.62	-30.38	0.24
		59 - 5	27.98	-27.70	0.28
		18 - 5	8.51	-8.49	0.02
		Total Power Loss			0.54
	Bipolar	59 - 18	30.67	-30.55	0.12
		59 - 5	27.93	-27.79	0.14
		18 - 5	8.41	-8.40	0.01
		Total Power Loss			0.27
Case 2	Monopolar	59 - 18	33.84	-33.55	0.29
		59 - 5	24.75	-24.53	0.22
		18 - 5	11.66	-11.66	0.00
		Total Power Loss			0.51
	Bipolar	59 - 18	33.84	-33.69	0.15
		59 - 5	24.75	-24.64	0.11
		18 - 5	11.55	-11.55	0.00
		Total Power Loss			0.26
Case 3	Monopolar	59 - 18	21.92	-21.79	0.13
		59 - 5	36.67	-36.19	0.48
		Total Power Loss			0.61
	Bipolar	59 - 18	22.16	-22.10	0.06
		59 - 5	36.43	-36.19	0.24
		Total Power Loss			0.30

[17] W. Wang, M. Barnes, Power flow algorithms for multi-terminal vsc-hvdc with droop control, IEEE Transactions on Power Systems (2014).

[18] F. Akhter, D. Macpherson, G. Harrison, W. Bukhsh, Dc voltage droop control implementation in the ac/dc power flow algorithm: Combinational approach, 11th IET International Conference on AC and DC Power Transmission (2015).

[19] R. Hendriks, G. Paap, W. Kling, Control of a multi-terminal vsc transmission scheme f or connecting offshore wind farms, European Wind Energy Conference and Exhibition (May 2007).

[20] T. Haileselassie, K. Uhlen, Precise control of power flow in multiterminal vsc-hvdcs using dc voltage droop control, IEEE Power and Energy Society General Meeting (2012).

[21] L. Sorber, M. V. Barel, L. de Lathauwer, Unconstrained optimization of real functions in complex variables, Society for Industrial and Applied Mathematics - SIAM 22, No. 3 (2012) 879–898.

[22] K. Kreutz-Delgado, The complex gradient operator and the CR-calculus, ArXIV e-print, arXIV:0906.4835v1 [math.OC] (2009) 1–74.

[23] J. Verboomen, D. V. Hertem, P. H. Schavemaker, W. L. Kling, R. Belmans, Phase shifting transformers: principles and applications, in: 2005 International Conference on Future Power Systems, 2005, pp. 6 pp.–6.

[24] G. Daelemans, K. Srivastava, S. Cole, R. Belmans, Minimization of steady-state losses in meshed networks using vsc hvdc, IEEE Power Energy Society General Meeting (2009).

Bibliography

1 STEINMETZ, C. P. Complex quantities and their use in electrical engineering. *Proceedings of the International Electrical Congress*, p. 33–74, 1893. Mentioned on page 17.

2 WIRTINGER, W. Zur Formalen Theorie der Functionen Von Mehr Complexen Ver¨anderlichen. *Math. Ann.*, v. 97, p. 357–375, 1927. Mentioned on pages 17, 37, and 83.

3 REMMERT, R. *Theory of Complex Functions*. [S.l.]: Springer-Verlag, New York, 1991. Mentioned on page 17.

4 HUGHES, C. J. *Single-Instruction Multiple-Data Execution*. [S.l.]: Morgan & Claypool, 2015. ISSN 1935-3235. Mentioned on pages 17 and 50.

5 PIRES, R. *Complex-Valued Steady-State Models as Applied to Power Flow Analysis and Power System State Estimation*. 76 p. Tese (Doutorado) — Institute of Electric Systems and Energy - ISEE, https://repositorio.unifei.edu.br/xmlui/handle/123456789/55, February 2018. Mentioned on pages 17, 37, 52, and 82.

6 DžAFIC, I.; JABR, R.; HRNJIC, T. High performance distribution network power flow using wirtinger calculus. *IEEE Transactions on Smart Grid*, April 2018. ISSN 1949-3061. Mentioned on page 17.

7 SARMIENTO, J. et al. A complex-valued three-phase load flow for radial networks: High-performance and low-voltage solution capability. *IEEE Transactions on Power Systems*, Jan 2019. ISSN 0885-8950. Mentioned on page 17.

8 NGUYEN, T.; VU, C. Complex-variable newton-raphson load-flow analysis with facts devices. *IEEE PES Transmission and Distribution Conference and Exhibition*, Aug 2006. ISSN 2160-8555. Mentioned on pages 17, 37, and 52.

9 TRIAS, A. The holomorphic embedding load flow method. In: IEEE. *2012 IEEE Power and Energy Society General Meeting*. [S.l.], 2012. p. 1–8. Mentioned on page 18.

10 TRIAS, A. Fundamentals of the holomorphic embedding load-flow method. *arXiv preprint arXiv:1509.02421*, 2015. Mentioned on page 18.

11 PIRES, R.; MILI, L.; CHAGAS, G. Robust complex-valued Levenberg-Marquardt algorithm as applied to power flow analysis. *International Journal of Electrical Power & Energy Systems*, v. 113, p. 383 – 392, 2019. ISSN 0142-0615. Mentioned on pages 18 and 57.

12 KIM, C.-K. et al. *HVDC Transmission: Power Conversion Applications in Power Systems*. [S.l.]: Wiley & Sons, 2009. Mentioned on pages 19, 20, and 25.

13 JOVCIC, D. *High Voltage Direct Current Transmission: Converters, Systems and DC Grids*. 2. ed. United Kingdom: John Wiley Sons Ltd., 2019. ISBN 9781119566540. Mentioned on pages 20, 26, 52, and 55.

14 KUNDUR, P. *Power System Stability and Control*. [S.l.]: McGraw-Hill Inc, 1993. Mentioned on pages 20, 21, 22, 25, and 33.

15 ARRILLAGA, J.; LIU, Y.; WATSON, N. *Flexible Power Transmission – The HVDC options*. [S.l.]: Wiley & Sons, 2007. Mentioned on pages 25, 26, and 28.

16 OTTOSSON, N.; KJELLIN, L. Modular back-to-back hvdc, with capacitor commutated converters (ccc). *IEEE AC-DC Power Transmission*, p. 55–59, Dez. 2001. Mentioned on page 25.

17 GRAHAM, J. et al. The rio madeira hvdc system – design aspects of bipole 1 and the connector to acre-rondônia. *CIGRÉ 2012*, Aug. 2012. Mentioned on page 25.

18 JIANG-HAFNER, Y. et al. Hvdc with voltage source converters - a powerful standby black start facility. *Transmission and Distribution Conference and Exposition IEEE/PES*, Apr. 2008. Mentioned on page 26.

19 DU, C. *VSC-HVDC for industrial power systems*. Tese (Doutorado) — Chalmers University of Technology, Göteborg, Sweden, 2007. Mentioned on page 26.

20 IT'S time to connect - technical description of HVDC Light technology. [S.l.], 2008. Mentioned on page 27.

21 DODDS, S. et al. Hvdc vsc (hvdc light) transmission – operating experiences. *CIGRÉ 2010*, Aug. 2010. Mentioned on page 28.

22 SELLICK, R.; ÅKERBERG, M. Comparison of hvdc light (vsc) and hvdc classic (lcc) site aspects, for a 500mw 400kv hvdc transmission scheme. *IET ACDC 2012*, Dec. 2012. Mentioned on page 28.

23 LESNICAR, A.; MARQUARDT, R. An innovative modular multilevel converter topology suitable for a wide power range. *IEEE Bologna Power Tech Conference Proceedings*, Jun. 2003. Mentioned on page 28.

24 GLINKA, M.; MARQUARDT, R. A new ac/ac multilevel converter family. *IEEE Transactions on Industrial Electronics*, v. 53, n. 3, p. 662 – 669, Jun. 2005. Mentioned on page 28.

25 ALLEBROD, S.; HAMERSKI, R.; MARQUARDT, R. New transformerless, scalable modular multilevel converters for hvdc-transmission. *IEEE Power Electronics Specialists Conference*, Jun. 2008. Mentioned on page 28.

26 DORN, J.; HUANG, H.; RETZMANN, D. "a new multilevel voltage-sourced converter topology for hvdc applications. *IEEE Power Electronics Specialists Conference*, 2008. Mentioned on page 28.

27 BARNES, M.; BEDDARD, A. Voltage source converter hvdc links – the state of the art and issues going forward. *Energy Procedia*, v. 24, p. 108 – 122, Aug. 2012. Mentioned on page 31.

28 HERTEM, D. V.; GHANDHARI, M. Multi-terminal vsc hvdc for the european supergrid: Obstacles. *Renewable and Sustainable Energy Reviews*, v. 14, n. 9, p. 3156–3163, Dec. 2010. Mentioned on page 33.

29 NAKAJIMA, T.; IROKAWA, S. A control system for hvdc transmission by voltage sourced converters. *IEEE PES Summer Meeting*, Jul. 1999. Mentioned on page 34.

30 HENDRIKS, R. et al. Control of a multi-terminal vsc transmission scheme for connecting offshore wind farms. *European Conference on Power Electronics and Applications*, May. 2007. Mentioned on page 35.

31 DIERCKXSENS, C. et al. A distributed dc voltage control method for vsc mtdc systems. *Electric Power Systems Research*, v. 82, n. 1, p. 54–58, 2012. ISSN 0378-7796. Disponível em: <https://www.sciencedirect.com/science/article/pii/S0378779611001933>. Mentioned on pages 35 and 57.

32 HAILESELASSIE, T. et al. Control of multiterminal hvdc transmission for offshore wind energy. *Nordic Wind Power Conference Presentation*, Sep. 2009. Mentioned on page 35.

33 BARBOZA, L.; ZÜRN, H.; SALGADO, R. Load tap change transformer: A modeling reminder. *IEEE Power Engineering Review*, p. 51–52, 2001. Mentioned on pages 37 and 38.

34 PIRES, R. Unbalanced phase-to-phase voltage compensators applied to radial distribution feeders. *Power Delivery, IEEE Transactions on*, v. 19, n. 2, p. 806–812, April 2004. ISSN 0885-8977. Mentioned on page 37.

35 VERBOOMEN, J. et al. Phase shifting transformers: principles and applications. In: *2005 International Conference on Future Power Systems*. [S.l.: s.n.], 2005. p. 6 pp.–6. Mentioned on page 42.

36 BHOWMICK, S. *Flexible Transmission Systems (FACTS) - Newton Power Flow Modeling of Voltage-Sourced Converter Based Controllers*. [S.l.: s.n.], 2016. (International Standard Book Number-13: 978-1-4987-5620-4 (eBook - PDF)). Mentioned on page 43.

37 ZHANG, X.-P. Multiterminal voltage-sourced converter-based **HVDC** models for power flow analysis. *IEEE Transactions on Power Systems*, v. 19, n. 4, p. 1877–1884, Nov 2004. ISSN 0885-8950. Mentioned on pages 43 and 57.

38 AWASTHI, A. et al. Complex QR decomposition using fast plane rotations for MIMO applications. *IEEE Communications Letters*, v. 18, No. 10, p. 1743–1746, 2014. Mentioned on page 45.

39 MALTSEV, A. et al. Triangular systolic array with reduced latency for QR-decomposition of complex matrices. *IEEE International Symposium on Circuits and Systems - ISCAS*, p. 385–388, 2006. Mentioned on page 45.

40 GENTLEMAN, W. Least Squares Computations by Givens Transformations Without Square Roots. *Journal of Mathematics Applications*, v. 12, p. 329–336, 1974. Mentioned on page 45.

41 SIMÕES-COSTA, A.; QUINTANA, V. An Orthogonal Row Processing Algorithm for Power Sequential State Estimation. *IEEE-Transaction on Power Apparatus and Systems*, v. 100, n. 8, p. 3791–3800, August 1981. Mentioned on page 45.

42 WANG, J. W.; QUINTANA, V. H. A decoupled orthogonal row processing algorithm for power system state estimation. *IEEE Transactions on Power Apparatus and Systems*, PAS-103, n. 8, p. 2337–2344, Aug 1984. ISSN 0018-9510. Mentioned on page 45.

43 VEMPATI, N.; SLUTSKER, I. W.; TINNEY, W. F. Enhancement to givens rotations for power system state estimation. *IEEE Transactions on Power Systems*, v. 6, n. 2, p. 842–849, May 1991. ISSN 0885-8950. Mentioned on page 45.

44 SACHDEV, M. S.; MEDICHERLA, T. K. P. A second order load flow technique. *IEEE Transactions on Power Apparatus and Systems*, v. 96, n. 1, p. 189–197, Jan 1977. ISSN 0018-9510. Mentioned on page 46.

45 IWAMOTO, S.; TAMURA, Y. A fast load flow method retaining nonlinearity. *IEEE Transactions on Power Apparatus and Systems*, PAS-97, n. 5, p. 1586–1599, Sept 1978. ISSN 0018-9510. Mentioned on pages 46 and 47.

46 ROY, L. Exact Second Order Load Flow. *Proceedings of 6-th power system computation conference (PSCC) - Cambridge - UK*, p. 711–713, Aug. 1978. Mentioned on page 46.

47 RAO, P. S. N.; RAO, K. S. P.; NANDA, J. An exact fast load flow method including second order terms in rectangular coordinates. *IEEE Transactions on Power Apparatus and Systems*, PAS-101, n. 9, p. 3261–3268, 1982. Mentioned on page 46.

48 CORY, B.; EKWUE, A.; JOHNSON, R. Comparative analysis of the convergence characteristics of second-order loadflow methods. *International Journal of Electrical Power and Energy Systems*, v. 12, n. 4, p. 251 – 256, 1990. ISSN 0142-0615. Mentioned on page 46.

49 MOKHLIS, H.; SHAHRIARI, A.; LAGHARI, J. Fast and accurate second order load flow method based on fixed jacobian matrix. *Applied Mathematics and Computation*, v. 269, p. 584 – 593, 2015. ISSN 0096-3003. Disponível em: <http://www.sciencedirect.com/science/article/pii/S0096300315009947>. Mentioned on page 46.

50 IWAMOTO, S.; TAMURA, Y. A load flow calculation method for ill-conditioned power systems. *IEEE Transactions on Power Apparatus and Systems*, PAS-100, n. 4, p. 1736–1743, April 1981. ISSN 0018-9510. Mentioned on page 47.

51 BEERTEN, J.; COLE, S.; BELMANS, R. A sequential AC/DC power flow algorithm for networks containing multi-terminal vsc hvdc systems. In: *IEEE PES General Meeting*. [S.l.: s.n.], 2010. p. 1–7. ISSN 1944-9925. Mentioned on pages 52, 59, and 64.

52 BEERTEN, J. et al. Generalized steady-state vsc mtdc model for sequential ac/dc power flow algorithms. *IEEE Transactions on Power Systems*, v. 27, n. 2, p. 821–829, May. 2012. Mentioned on pages 52, 59, 70, 71, and 72.

53 ARIFOGLU, U. The power flow algorithm for balanced and unbalanced bipolar multiterminal AC-DC systems. *Electric Power Systems Research*, v. 64, n. 3, p. 239 – 246, 2003. ISSN 0378-7796. Disponível em: <http://www.sciencedirect.com/science/article/pii/S0378779602001931>. Mentioned on page 52.

54 EL-HAWARY, M.; IBRAHIM, S. A new approach to AC-DC load flow analysis. *Electric Power Systems Research*, v. 33, n. 3, p. 193 – 200, 1995. ISSN 0378-7796. Disponível em: <http://www.sciencedirect.com/science/article/pii/037877969500945E>. Mentioned on pages 52 and 59.

55 WANG, W.; BARNES, M. Power flow algorithms for multi-terminal vsc-hvdc with droop control. *IEEE Transactions on Power Systems*, v. 29, n. 4, p. 1721–1730, 2014. Mentioned on pages 52 and 57.

56 ACHA, E.; CASTRO, L. M. A generalized frame of reference for the incorporation of multi-terminal VSC-HVDC systems in power flow solutions. *Electric Power Systems Research*, v. 136, p. 415 – 424, 2016. ISSN 0378-7796. Disponível em: <http://www.sciencedirect.com/science/article/pii/S0378779616300566>. Mentioned on pages 52 and 53.

57 KHAN, S.; BHOWMICK, S. A novel power-flow model of multi-terminal VSC-HVDC systems. *Electric Power Systems Research*, v. 133, p. 219 – 227, 2016. ISSN 0378-7796. Disponível em: <http://www.sciencedirect.com/science/article/pii/S0378779615004083>. Mentioned on pages 52 and 57.

58 ZHANG, X.-P. Multiterminal voltage-sourced converter-based HVDC models for power flow analysis. *IEEE Transactions on Power Systems*, v. 19, n. 4, p. 1877–1884, Nov 2004. ISSN 0885-8950. Mentioned on page 52.

59 BARADAR, M.; GHANDHARI, M.; HERTEM, D. V. The modeling multi-terminal vsc-hvdc in power flow calculation using unified methodology. In: *2011 2nd IEEE PES International Conference and Exhibition on Innovative Smart Grid Technologies*. [S.l.: s.n.], 2011. p. 1–6. Mentioned on pages 52 and 67.

60 NARAYANAN, K. N.; MITRA, P. A comparative study of a sequential and simultaneous ac-dc power flow algorithms for a multi-terminal vsc-hvdc system. In: *2013 IEEE Innovative Smart Grid Technologies-Asia (ISGT Asia)*. [S.l.: s.n.], 2013. p. 1–6. Mentioned on pages 52, 64, and 67.

61 ACHA, E.; KAZEMTABRIZI, B.; CASTRO, L. M. A new VSC-HVDC model for power flows using the Newton-Raphson method. *IEEE Transactions on Power Systems*, v. 28, n. 3, p. 2602–2612, Aug 2013. ISSN 0885-8950. Mentioned on page 53.

62 ACHA, E.; KAZEMTABRIZI, B. A new STATCOM model for power flows using the Newton–-Raphson method. *IEEE Transactions on Power Systems*, v. 28, n. 3, p. 2455–2465, Aug 2013. ISSN 0885-8950. Mentioned on page 53.

63 DAELEMANS, G. et al. Minimization of steady-state losses in meshed networks using vsc hvdc. *IEEE Power Energy Society General Meeting*, July 2009. ISSN 1932-5517. Mentioned on page 55.

64 HAILESELASSIE, T. M.; UHLEN, K. Impact of dc line voltage drops on power flow of mtdc using droop control. *IEEE Transactions on Power Systems*, v. 27, n. 3, p. 1441–1449, 2012. Mentioned on page 57.

65 GOMIS-BELLMUNT, O. et al. Voltage–current characteristics of multiterminal hvdc-vsc for offshore wind farms. *Electric Power Systems Research*, v. 81, n. 2, p. 440–450,

2011. ISSN 0378-7796. Disponível em: <https://www.sciencedirect.com/science/article/pii/S0378779610002403>. Mentioned on page 57.

66 ASPLUND, G. et al. Cigre tb 533-working group b4. 52-hvdc grid feasibility study. CIGRÉ, 2013. Mentioned on page 57.

67 GRIGG, C. et al. The ieee reliability test system-1996. a report prepared by the reliability test system task force of the application of probability methods subcommittee. *IEEE Transactions on Power Systems*, v. 14, n. 3, p. 1010–1020, 1999. Mentioned on page 70.

68 KREUTZ-DELGADO, K. The complex gradient operator and the CR-calculus. *ArXIV e-print, arXIV:0906.4835v1 [math.OC]*, p. 1–74, June 25, 2009. Mentioned on page 82.